Dynamical changes in neuronal network function underlying epileptogenesis in the temporal lobe

Nicole Marley

Doctor of Philosophy

Aston University

April 2023

Aston University

Dynamical changes in neuronal network function underlying epileptogenesis in the temporal lobe

Nicole Marley

Doctor of Philosophy, 2023

Epilepsy is a common neurological disorder characterized by recurrent seizures. Even before the presentation of the first seizure, it is believed there is a chronic pathogenic process underlying the network, cellular and synaptic changes which result in the development of symptomatic epilepsy – termed epileptogenesis. Epileptogenesis involves several crucial, progressive steps which develop over a period of weeks, months or sometimes years: the initial precipitating assault/injury, the latent period, and spontaneous recurrent seizures (SRS). Understanding the development and progression of epileptogenesis within the temporal lobe offers a new avenue for controlling or even preventing the development of symptomatic epilepsy.

Animal models of epilepsy allow researchers to investigate the pathogenic process' of epilepsy and explore possible therapeutics, including anti-epileptic drugs. A low mortality, high morbidity model for epilepsy termed the reduced intensity status epilepticus (RISE) model was developed to study temporal lobe epilepsy. Investigation of the early stages of epileptogenesis involved *ex vivo* local field potential (LFP) and whole-cell patch clamp recordings of extracted brain slices from RISE animals during the latent period (weeks 2, 3, 4, 5, and 6 post-induction) and during the SRS stage of epileptogenesis (>3 months post-induction). Using several measures of brain excitability, it was found there is a marked reduction in brain excitability for RISE animals during the later stages of epileptogenesis (weeks 4 – 6 post-induction) compared to aged-matched control (AMC) in hippocampal subregions CA1 and CA3. However, there appears to be recovery to AMC or even above as animals enter SRS despite now displaying electrographic and behavioural seizures.

Previous work studying the RISE model of epilepsy has uncovered a dramatic loss of the glutamatergic ionotropic AMPA receptors (AMPARs) and their associated accessory proteins in the hippocampus during the latent period which continues into SRS. Tianeptine is an atypical anti-depressant which is already known to modulate AMPAR function by increasing channel conductance and by increasing AMPAR trafficking and anchoring into the postsynaptic membrane. Control experiments confirmed this by revealing a marked increase in hippocampal gamma oscillatory power when conducting LFP experiments across all ages studied.

Given the proposed mechanism of action of tianeptine, tianeptine (10μM) was then studied as a potential anti-epileptogenic drug to modify the progression of epileptogenesis within the RISE model. *Ex vivo* LFP and patch clamp recordings were taken and found tianeptine was able to recover the hippocampal oscillation during the early stages of epileptogenesis but had subregional differences as the epileptogenesis progressed. Under both spontaneous and kainic acid (KA) conditions, tianeptine had minimal effects on the gamma oscillations in both hippocampal subregions CA1 and CA3 during the latent period (6 weeks post-induction) compared to AMC. However, once RISE animals enter SRS, tianeptine was only capable of modulating gamma oscillations in CA1 (and not CA3) in KA conditions. Therefore, showing subregional differences in the progression of epileptogenesis.

Finally, to explore seizure susceptibility, the 0 Mg^{2+} *in vitro* model of epilepsy was employed in the hippocampus. Using several measures, it was found RISE animals were more susceptible to generate seizures and seizure-like activity. Seizure susceptibility decreased as RISE animals entered later into the latent period (weeks 5 – 6 post-induction) and again increased as they entered SRS. This combines with the above findings of reduced brain excitability during the latent period which likely drives the progression of epileptogenesis into SRS. Overall, this thesis shows there are dynamical changes in neuronal network function which underlie epileptogenesis in the temporal lobe.

Acknowledgements

First and foremost, my biggest thank you and gratitude goes to my supervisor Professor Gavin Woodhall. Not only has Gavin been incredible with all the support, encouragement, and inspiration throughout my whole PhD, but has also been understanding during difficult times. Not only has this made the PhD an amazing experience overall but has helped me grow into the person I am today. A big thank you also goes to my co-supervisor Dr Stuart Greenhill for all the advice and support over the years.

I would also like to thank all the amazing lab mates that have shared the journey with me, particularly to Max, Ellen, Divya, Manoj, Hannah, and Beth. No better group of people to have shared the highs and lows of research with (in the pub usually)!

Another massive thank you goes to the Biomed team, especially Wayne, Matt, and Kat. They would continuously go above and beyond to help in every way, and without them the PhD would have been a much more difficult process.

Finally, I would like to thank my friends and family for all their support. Choosing to study a PhD in neuroscience was heavily influenced by my dad, Paul. As such, I would like to dedicate this thesis to my dad, and I hope it is something he is proud of.

Table of contents

Acknowledgements 3
Table of contents 4
List of Figures 8
List of Tables 10
Abbreviations 11
Chapter 1 Introduction 12
1.1. The temporal lobe 13
1.1.1. The hippocampus 14
1.1.2. The entorhinal cortex 15
1.1.2.1. The medial entorhinal cortex 15
1.2. Epilepsy 16
1.2.1. Seizures 17
1.2.2. Temporal lobe epilepsy 17
1.2.3. Epileptogenesis 18
1.2.4. Animal models of epilepsy 19
1.2.4.1. Reduced Intensity Status Epilepticus model of epilepsy 19
1.3. Tianeptine 21
1.4. Neurotransmitters and receptors 22
1.4.1. Glutamate 22
1.4.1.1. NMDA receptors 22
1.4.1.2. AMPA receptors 24
1.4.2. GABA 26
1.4.2.1. $GABA_A$ receptors 26
1.4.2.2. Inhibitory interneurons 27
1.5. Neuronal network oscillations 28
1.5.1. Gamma oscillations 30
1.5.1.1. ING model of gamma oscillations 31
1.5.1.2. PING model of gamma oscillations 31
1.5.1.3. The role of glutamate receptors in gamma oscillations 32
1.6. Aims and objectives 34
Chapter 2 Methods 35
2.1. Animals and ethical approval 36

2.2. Reduced Intensity Status Epilepticus model of epilepsy and epileptogenesis 36
2.3. Behavioural experiments 37
2.3.1. Post-seizure behavioural battery test 37
2.4. Brain slice preparation 38
2.5. *In vitro* electrophysiology experiments 39
2.5.1. Extracellular recordings 39
2.5.2. Intracellular recordings 42
2.6. Data collection and analysis 43
2.6.1. LFP data analysis 43
2.6.1.1. FFT algorithms 43
2.6.1.2. Peak gamma power 43
2.6.1.3. Seizure-like activity *in vitro* 44
2.6.2. Patch clamp data analysis 45
2.7. Drugs 45
Chapter 3 Modelling the progression of epileptogenesis *in vitro* 47
3.1. Introduction 48
3.1.1. Current understanding of epileptogenesis using the RISE model of epilepsy 48
3.2. Results 49
3.2.1. Network excitability – spontaneous local field potential oscillations in epileptogenesis 49
3.2.2. Network excitability – kainic acid-induced local field potential oscillations in epileptogenesis 52
3.2.3. Exploring the latent period of epileptogenesis - week 5 post-induction 55
3.2.4. Network excitability and the transition from the latent period to SRS 59
3.2.5. Changes in synaptic excitability during epileptogenesis 60
3.3. Discussion 66
Chapter 4 Local field and synaptic effects of tianeptine *in vitro* 69
4.1. Introduction 70
4.2. Results 71
4.2.1. Effect of acute tianeptine on spontaneous local field hippocampal gamma oscillations 71
4.2.2. Effect of acute tianeptine on KA-induced local field hippocampal gamma oscillations 75
4.2.3. Effect of acute tianeptine on synaptic neurotransmission in CA1 78
4.3. Discussion 80

4.3.1. Pitfall in the whole-cell voltage clamp experiments 80
4.3.2. Mechanisms by which tianeptine potentiates oscillations 80
Chapter 5 The effect of tianeptine during epileptogenesis *in vitro* 82
5.1. Introduction 83
5.2. Results 83
5.2.1. The effect of tianeptine on spontaneous network activity for AMC and RISE 83
5.2.2. The effect of tianeptine on spontaneous network activity for AMC and RISE – 6 weeks post-induction 86
5.2.3. The effect of tianeptine on KA-induced network activity for AMC and RISE 90
5.2.4. The effect of tianeptine on KA-induced network activity for AMC and RISE – SRS stage of epileptogenesis 93
5.2.5. Network excitability and the transition from the latent period to SRS 98
5.2.5. The effect of tianeptine on synaptic activity during epileptogenesis 99
5.3. Discussion 101
5.3.1. Network excitability and the response to tianeptine during the latent period 101
5.3.2. Network excitability and the response to tianeptine during the SRS stage of epileptogenesis 103
5.3.3. This excitatory-inhibitory imbalance and the consequence for the transition to SRS 104
Chapter 6 Seizure-like activity *in vitro* 106
6.1. Introduction 107
6.1.1. 0 Mg^{2+} model of acute seizures 107
6.2. Results 108
6.2.1. Typical seizure generation in the hippocampus 108
6.2.2. AMC vs RISE – seizure susceptibility using the *in vitro* 0 Mg^{2+} model of epilepsy 109
6.2.3. Seizure initiation zone 113
6.2.4. Comparing seizure susceptibility between the latent period and SRS stage of epileptogenesis 114
6.3. Discussion 116
6.3.1. Increased seizure susceptibility following RISE induction 116
6.3.2. Seizure initiation zones 117
Chapter 7 A potential *in vitro* model of epileptogenesis 119
7.1. Introduction 120

7.2. Results 120
7.3. Discussion 126
Chapter 8 General discussion and future work 128
8.1. Introduction 129
8.2. Changes in brain excitability throughout epileptogenesis 129
8.3. Can tianeptine modulate the progression of epileptogenesis? 131
8.4. Increased seizure susceptibility using the RISE model of epilepsy 133
8.6. Conclusion 133
References 134

List of Figures

Figure 1.1. Diagram of the anatomy of the rat hippocampal-entorhinal pathways 16
Figure 1.2. Schematic representation of the organisation/structure of an NMDA receptor 23
Figure 1.3. Schematic representation of the AMPAR structure and the confirmational changes which occur during desensitisation 25
Figure 1.4. Schematic illustration of the major isoform of $GABA_A$ receptor 27
Figure 1.5. Illustration of current flow and the sink-source interaction 30
Figure 1.6. Schematic representation of the ING and PING models of gamma oscillations .. 32
Figure 2.1. Timeline for *in vitro* extraction and experimentation for studying epileptogenesis in AMC and RISE animals. 37
Figure 2.2. The local field potential interface recording chamber. 41
Figure 2.3. An example FFT showing analysis parameters for studying gamma oscillations. 44
Figure 2.4. An example of a section of trace showing seizures in CA1 *in vitro*. 45
Figure 3.1. Comparison of spontaneous network excitability in the hippocampus throughout epileptogenesis for AMC and RISE. 51
Figure 3.2. Comparison of kainic acid-induced network excitability in the hippocampus throughout epileptogenesis for AMC and RISE. 53
Figure 3.3. Normalised percentage change response to kainic acid in the hippocampus throughout epileptogenesis for AMC and RISE. 55
Figure 3.4. Exploring CA1 - week 5 post-induction of epileptogenesis. 57
Figure 3.5. Exploring CA3 - week 5 post-induction of epileptogenesis. 58
Figure 3.6. Comparison of network excitability during the latent period and SRS in spontaneous and KA conditions in RISE animals. 60
Figure 3.7. Changes in synaptic excitability during epileptogenesis. 62
Figure 3.8. sEPSC changes during week 6 post-induction and the SRS stage of epileptogenesis. 64
Figure 3.9. Comparison of sEPSCs between the latent period (6 weeks post-induction) and the SRS stage of epileptogenesis in RISE animals 65
Figure 3.10. Cumulative frequency graphs of sEPSC amplitude during week 6 post-induction and the SRS stage of epileptogenesis. 66
Figure 4.1. Effect of tianeptine on spontaneous gamma oscillations in CA1. 73
Figure 4.2. Effect of tianeptine on spontaneous gamma oscillations in CA3. 74
Figure 4.3. Effect of tianeptine on KA-induced gamma oscillations in CA1. 76
Figure 4.4. Effect of tianeptine on KA-induced gamma oscillations in CA3. 77
Figure 4.5. Combined percentage increase following tianeptine application in spontaneous and KA conditions. 78
Figure 4.6. Changes in synaptic excitability by tianeptine. 79

Figure 5.1. Comparison of tianeptine response on spontaneous network excitability in the hippocampus throughout epileptogenesis for AMC and RISE. 85
Figure 5.2. Exploring the effect of tianeptine in CA1 - week 6 post-induction of epileptogenesis. 88
Figure 5.3. Exploring the effect of tianeptine in CA3 - week 6 post-induction of epileptogenesis. 89
Figure 5.4. Comparison of tianeptine response on KA-induced network excitability in the hippocampus throughout epileptogenesis for AMC and RISE. 93
Figure 5.5. Exploring the effect of tianeptine in CA1 – SRS stage of epileptogenesis. 96
Figure 5.6. Exploring the effect of tianeptine in CA3 – SRS stage of epileptogenesis. 97
Figure 5.7. Comparison of network excitability during the latent period and SRS following tianeptine application in spontaneous and KA conditions. 99
Figure 5.8. Changes in synaptic excitability by tianeptine in AMC and RISE. 100
Figure 6.1. An example of a single seizure in CA1 *in vitro*. 109
Figure 6.2. Percentages of slices to seize for AMC and RISE 110
Figure 6.3. Time to first seizure for AMC and RISE. 111
Figure 6.4. Total seizure count and seizure duration for AMC and RISE. 112
Figure 6.5. Inter-seizure interval for AMC and RISE. 113
Figure 6.6. Seizure initiation percentages in CA1. 114
Figure 6.7. Comparing seizure susceptibility between 6 weeks post-induction and SRS in slices from RISE animals. 115
Figure 7.1. Example receptor shuttling (AMPAR internalisation) experiments in CA1 and CA3. 121
Figure 7.2. Percentage changes throughout the receptor shuttling experiment 122
Figure 7.3. Receptor shuttling (AMPAR internalisation) in CA1. 124
Figure 7.4. Receptor shuttling (AMPAR internalisation) in CA3. 125

List of Tables

Table 1.1. Common frequency bands within the brain and their functions. 28
Table 2.1. The Racine scale of seizures (Racine, 1972). 36
Table 2.2. The PSBB test..... 38
Table 2.3. All drugs and the final concentrations used *in vitro*. 46

Abbreviations

(m)EC – (medial) entorhinal cortex

(s)EPSC/P – (spontaneous) excitatory postsynaptic current/potential

(s)IPSC/P – (spontaneous) inhibitory postsynaptic current/potential

3Rs – replacement, reduction and refinement

aCSF – artificial cerebrospinal fluid

AED – anti-epileptic drug

AMC – aged-matched control

AMPA(R) – α-amino-3-hydroxy-5-methyl-4-isoxazolepropionic acid (receptor)

AUC – area under curve

CA(1/3) – cornu ammonis (1/3)

Ca^{2+} - calcium ion

CaMKII – calcium-calmodulin kinase II

CNQX – 6-cyano-7-nitroquinoxaline-2,3-dione

DG – dentate gyrus

EEG – electroencephalogram

GABA(R) – gamma-aminobutyric acid (receptor)

Hz – hertz

IBMX - 3-isobutyl-1-methylxanthine

IEI – inter-event interval

ING – interneuron network gamma

ISI – inter-seizure interval

KA(R) – kainic acid (receptor)

LFP – local field potential

LTD – long term depression

LTP – long term potentiation

Mg^{2+} - magnesium ion

mM – millimolar

MOR – mu opioid receptor

MPEP - 2-methyl-6-(phenylethyl)pyridine

Na^{+} - sodium ion

NBQX – 2,3-dioxo-6-nitro-7-sulfamoyl-benzo[f]quinoxaline

nM – nanomolar

NMDA(R) – N-methyl-D-aspartate (receptor)

PID – post-ictal depression

PING – pyramidal network interneuron gamma

PIS – post-ictal spiking

PKA – protein kinase A

PSBB – post-seizure behavioural battery test

PSD – postsynaptic density

RISE – reduced intensity status epilepticus

SE – status epilepticus

SEM – standard error of the mean

SLA – seizure-like activity

SLE – seizure-like events

SRS – spontaneous recurrent seizures

TARP – transmembrane AMPA receptor regulatory proteins

TLE – temporal lobe epilepsy

µM – micromolar

Chapter 1 Introduction

The mammalian brain is a highly organised and sophisticated organ comprised of the cerebrum, cerebellum, and brainstem. The cerebrum can be further divided into the frontal, parietal, temporal, and occipital lobes. The most superficial area of the cerebrum, the cerebral cortex, is responsible for highly evolved functions such as cognition, mental imagery, and the ability to produce and understand language. Sitting just below are subcortical structures (e.g., hippocampus, amygdala, thalamus and basal ganglia) essential for more primitive functions, including movement, consciousness, perception, emotion and maintaining bodily homeostasis (Ackerman, 1992).

For this thesis, exploration of the development and progression of epilepsy in the temporal lobe using a variety of *in vitro* and *ex vivo* methods is used to investigate the neuronal network dynamics which underlie epileptogenesis.

1.1. The temporal lobe

The temporal lobe is one of four major lobes of the brain. Located near the temples of the skull, it is anterior to the occipital lobe and posterior to the frontal lobe. The temporal lobe is further subdivided into the superior temporal lobe, middle temporal lobe, and the inferior temporal lobe. Functionally, the temporal lobe plays vital roles in the processing of auditory, olfactory, vestibular, visual, and linguistic information. A significant part of the temporal lobe is the hippocampal formation, comprised of: parahippocampal gyrus, subiculum, hippocampus, and dentate gyrus (Kiernan, 2012). Pathological development/changes to the hippocampal formation have been associated with numerous neurological disorders, including epilepsy, Alzheimer's disease, schizophrenia and depression (Small et al., 2011).

The role of the medial temporal lobe in the formation of new memories is relatively established (Baxter, 2009). Under the 'standard' model, the binding of a memory trace between the neocortex (where the memory is initially registered) and the hippocampus and related structures (where the memory temporally held for storage and recovery) allows for unity of this new memory. Damage to the medial temporal lobe with resulting retrograde amnesia results in particular deficits in episodic (event) and semantic (factual) memory equally, but only within a given time period (Nadel and Moscovitch, 1997). A study with bilateral lesions of the EC in monkeys showed disruption of the relational organisation of declarative memory, with specific dysfunctions in episodic memory (Buckmaster et al., 2004). Therefore, highlighting a central role of the medial temporal lobe in memory formation and sustainment.

A famous case study demonstrating the fundamental role medial temporal lobe structures play in memory is that of Henry Molaison (formally known as H.M.). Following a traumatic brain injury sustained aged 7, H.M. began developing seizures a few years later. By age 27, these were severe and not well managed with high doses of anti-convulsants. H.M. was offered a bilateral medial temporal lobe resection (including hippocampus, parahippocampal cortices,

entorhinal cortices, and amygdala) which managed the epilepsy, however this produced severe memory impairment with absence of general intellectual loss of perceptual disorder. Despite the significant impairment caused to H.M. following the surgery, this case motivated the development of an animal model of human memory impairment and subsequent delineation of the medial temporal lobe memory system, therefore leading to a deeper understanding of how memory is organised in the brain (Squire, 2009).

1.1.1. The hippocampus

The hippocampus was first identified by Greek surgeon Julius Caesar Arantius in 1587 and termed 'hippokampos' due to its resemblance to a seahorse (Bir et al., 2015). The hippocampus is a part of the limbic system and is central to the consolidation process of integrating short-term memories into long-term, permanent memory formation, particularly of spatial information (Terranova et al., 2019). Located in the allocortex (archicortex), the hippocampus is a conserved brain structure identified in an array of species, ranging from fish to birds to mammals, indicating its significance in memory formation and consolidation (Bingman et al., 2009).

The hippocampus is made up of the hippocampal proper (also called Ammon's horn/cornu Ammonis, CA) including subfields CA1, CA2 and CA3, and the dentate gyrus (DG). The hippocampal circuit which allows the flow of information is termed the 'trisynaptic loop' and is made up of the DG, CA3 and CA1. The DG projects directly to CA3 via the mossy fibre pathway, and CA3 projects directly to CA1 via the Schaffer Collateral pathway. CA3 also projects back onto other CA3 neurons and the DG, forming a recurrent collateral pathway. These recurrent collaterals have been shown to play a role in 'holding memory' (e.g., novel information can be temporarily held despite a distraction present, such as a phone ringing) (Anand and Dhikav, 2012). Historically, CA2 has been ignored and only considered a transitional region of the hippocampus. However, research has begun elucidating the differing response to neurodegeneration and disease CA2 demonstrates in comparison to other hippocampal subregions, suggesting CA2 has its own distinct functions (Knierim, 2015, Pang et al., 2019).

The entorhinal cortex (EC) provides the major inputs to the hippocampus via two main pathways: (1) the perforant pathway projects directly onto the DG and CA3 from layer II of the medial EC (mEC) (Witter et al., 2000), and (2) the temporoammonic pathway projects directly to CA1 and the subiculum from layer III of the mEC (Steward and Scoville, 1976). Feedback projections are received in the deep layer V of the EC, which are further projected to the lateral septum via the fornix. CA1 also has output projections to the nucleus accumbens (ventral striatum), amygdala and prefrontal cortex (Pang et al., 2019) (figure 1.1.).

Anatomically, hippocampal identification can be done with relative ease due to its unique layer of cell bodies. Anterior to this dark cell body layer is the *Stratum oriens* which contains primarily

a few inhibitory basket-cell interneurons. The *stratum pyramidalis* forms the principal cellular component of the hippocampus, with 10 – 30 layers of excitatory pyramidal cells. Apical dendrites of the pyramidal cells receive afferents from the EC and DG mossy fibres and can form the recurrent collateral pathways mentioned above. Posterior to the *stratum pyramidalis* is this *stratum radiatum* which comprises of apical dendrites of the pyramidal cells and some stellate cells. Finally, the *stratum lacunosum moleculare* contains primarily axons and inhibitory interneurons. The majority of neurons (up to 90%) in the hippocampus are excitatory pyramidal cells, with the rest being inhibitory interneurons (e.g. stellate cells), demonstrating a strong disposition towards excitatory neurotransmission in the hippocampus (Chauhan et al., 2021).

1.1.2. The entorhinal cortex

The entorhinal cortex (EC) is a brain region part of the parahippocampal region (along with the perirhinal and postrhinal cortices) located within the medial temporal lobe. Subdivided into the lateral (lEC) and medial (mEC), the EC acts as a major input/output structure for the hippocampus.

1.1.2.1. The medial entorhinal cortex

The medial entorhinal cortex (mEC) is made up of six layers (I – VI). Layers I (plexiform layer) and IV (laminar dissecans) are relatively free of cells (Canto et al., 2008). Incoming information converges onto mEC superficial layers II and III, originating from the postrhinal/parahippocampal cortex, neocortex (visual, posterior parietal and the pre- and para-subiculum), and subcortex (dorsal thalamus and thalamic nuclei) (Kerr et al., 2007, Witter et al., 2017). Processing of this information occurs in the hippocampal formation via two main pathways: (1) the perforant pathway projects directly onto the dentate gyrus and CA3 from layer II (Witter et al., 2000), and (2) the temporoammonic pathway projects directly to CA1 and the subiculum from layer III (Steward and Scoville, 1976). Before re-entering the mEC in the deeper layer V (specifically layer Vb). Layer Vb neurons can innervate neurons in layers Va, II and II creasing a feedback loop, and feedforward to other (sub)cortical areas (Ohara et al., 2018, Wouterlood et al., 2004).

Despite having different input pathways to the hippocampus, superficial layers II and III share the same anti-phase to the extracellular field activity, meaning principal cells in both layers share the same temporal pattern of inhibitory drive. There is however a distinct phase reversal between layer II and III, with the authors explaining this is due to the source-sink interaction generated (Cunningham et al., 2003).

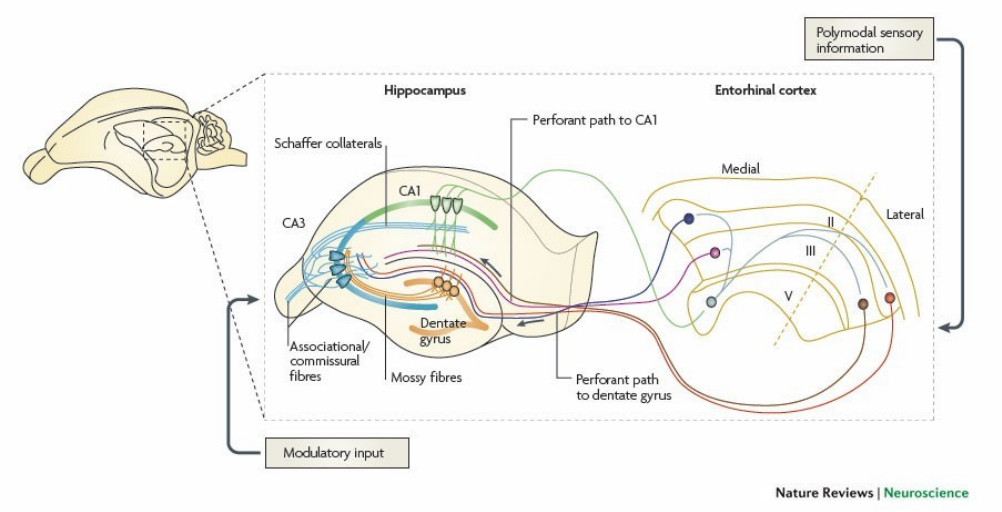

Figure 1.1. Diagram of the anatomy of the rat hippocampal-entorhinal pathways (Neves et al., 2008).

Diagram shows the major input connections to the DG/CA3 via mEC layer II (perforant pathway). Mossy fibre projections and associational/commissural projections converse at CA3, which projects to CA2/1 via Schaffer collaterals. Temporoammonic pathway projects from mEC layer III directly to CA1. Hippocampal output via CA1 projects to mEC layer V via the subiculum.

1.2. Epilepsy

Epilepsy is one of the most common neurological conditions affecting 1% of the population, with an incidence of approximately 50 new cases per 100,00 population p/a. Approximately 75% of cases begin during childhood, reflecting the vulnerability of the brain during development. The International League Against Epilepsy (ILAE) defines epilepsy as the occurrence of at least one epileptic seizure (with its associated neurobiological, cognitive, psychological and social disturbances) which results in the increased likelihood of generating epileptic seizures in the future (Fisher et al., 2005).

The aetiology of epilepsy can be divided into idiopathic (genetic abnormalities, e.g., *SCN1A* gene), cryptogenic (aetiology obscure or unknown) and symptomatic groups (acquired, developmental, and congenital structural brain abnormalities, e.g., focal cortical dysplasia and anti-NMDAR autoimmune encephalitis). Regardless of which group, epilepsy as a disease is the final common pathway for numerous pathophysiological processes (Sirven, 2015).

Epileptic seizures can be categorised into three types – generalised, localised, and epileptic spasms. Generalised seizures begin in bilateral distributed neuronal networks and are subtyped into tonic-clonic, absence (typical or atypical), and myoclonic (tonic or atonic). Localised seizures begin neuronal networks limited to one hemisphere but can lateral generalise. Seizures can begin in the cortex or sub-cortical structures and are named depending on the areas involved, e.g., temporal lobe epilepsy originates within structures of the temporal lobe(s) (Berg et al., 2010).

1.2.1. Seizures

The main symptom of epilepsy is uncontrollable seizures. A seizure is defined as 'a paroxysmal alteration of neurologic function caused by the excessive, hypersynchronous discharge of neurons in the brain' (Shorvon, 2011, Stafstrom and Carmant, 2015). The use of EEG has been imperative in helping researchers and clinical epileptologists identify, classify, and quantify seizures and seizure-like events (SLE) (Blume et al., 1984). Typical seizure/SLE patterns may including ictal discharges (IDs, prolonged epileptiform discharges lasting for more than a few seconds), inter-ictal discharges (IIDs, single population burst of ~100 ms duration) and post-ictal discharges (PIDs, single population bursting following post-ictal depression). *In vitro* studies have identified the existence of late recurrent discharges (LRDs) which are distinct from IDs and IIDs and are found to be resistant to some anti-epileptic drugs (e.g., valproic acid) (Dreier and Heinemann, 1990, Quilichini et al., 2002, Sokolova et al., 1998, Zhang et al., 1995) Although LRDs have been compared to status epilepticus, similar periodic epileptiform discharges have been identified in humans (Treiman et al., 1990).

Fundamentally, seizure initiation is due to an imbalance of excitation and inhibition in the network resulting in sustained neuronal depolarisation and resulting burst action potential firing. Recruitment of surrounding neurons leads to seizure propagation (Bromfield et al., 2006). Structural and functional changes which can occur to result in this imbalance include: neuronal loss (Buckmaster and Dudek, 1997, Lowenstein et al., 1992), granule cell dispersion (Del Río et al., 1997, Haas et al., 2002, Nitta et al., 2008), mossy fibre sprouting (Sloviter, 1992, Wuarin and Dudek, 1996, Wuarin and Dudek, 2001), loss of GABAergic interneurons and associated glutamic acid decarboxylase enzymes (Marx et al., 2013, Shetty and Turner, 2001) and hypometabolism (Akman et al., 2010, Kim et al., 2017, Theodore et al., 2004).

1.2.2. Temporal lobe epilepsy

Temporal lobe epilepsy (TLE) is the most common form of focal epilepsy, representing two thirds of cases of intractable (drug-resistant) epilepsy managed surgically. TLE is classified into two main groups (medial epilepsy (originating in the medial temporal structures, such as the hippocampus, entorhinal cortex, amygdala and parahippocampal gyrus), and lateral or neocortical epilepsy (originating in the temporal neocortex, such as the associative sensory areas for hearing, virtual and language, and the temporal-occipital and temporal-parietal junctions) (Pascual, 2007).

Cardinal signs of TLE include: prodromes (e.g., headache, personality changes, irritability), aura (e.g., viscerosensory symptoms such as a rising epigastric sensation, or déjà vu), altered consciousness (associated with decreases activity in the default mode network), amnesia, automatism (coordinated involuntary motor activity which often involves the hands or mouth, such as fumbling or chewing) (Blair, 2012).

1.2.3. Epileptogenesis

Epileptogenesis is defined as the chronic pathogenic process by which a normal brain is transformed to an epileptic brain, capable of generating spontaneous seizures. Several crucial, progressive steps which develop over a period of weeks, months or sometimes years have been identified - following the initial precipitating insult/injury (e.g., trauma, status epilepticus, genetics), the brain undergoes a period of 'silence' where molecular, cellular and network changes occur. This is known as the latent period and is thought to be responsible for progression to subsequent spontaneous recurrent seizures (SRS). Animal models of epileptogenesis have noted this to be too simplistic, and stated a non-linear progressive increase in seizure frequency involving 4 steps: (1) initial phase of no seizures (the latent period), (2) a second phase with a gradual increase in seizure frequency with highly variable inter-seizure intervals, (3) a third phase with an exponential increase in seizure frequency, and (4) a final plateau phase with seizure frequency stabilised at a maximal rate (Williams et al., 2009, Wong, 2009).

The progression of seizure frequency suggests continual molecular, cellular and network changes occur throughout epileptogenesis. During the early stages of epileptogenesis, pre/interictal spikes can be observed in the EEG of patients following brain injury which precede the first spontaneous seizure. Immediate interneurons loss has been noted following brain injury, leading to a reduction in GABAergic synaptic inhibition and the emergence of spikes. Spikes may guide sprouting axons back to their network of origin, increasing synaptic strength and network excitability, and alter the balance of ion channels in the epileptic foci, therefore increasing the likelihood of progression into SRS (Angeleri et al., 1999, Kelley and Steward, 1997, Staley and Dudek, 2006). Accumulating evidence shows these molecular, cellular and network changes continue even after the establishment of SRS, meaning 'epileptogenesis' should encompass the full disease process beyond the initial emergence of symptomatic epilepsy (Pitkänen and Lukasiuk, 2011).

The latent period has become a focal point of epilepsy research due to its potential use as a therapeutic target before patients progress into symptomatic epilepsy. In patients with traumatic brain injury, the latent period ranged from 1 day to 10 years showing a large variation in time to first clinical seizure. Factors which affected the disease progression include the occurrence of respiratory difficulties during the initial stages, age of patient at time of insult, the presence of intracranial haemorrhage, the presence of skull fracture(s), and gender of patient (Löscher et al., 2015). Of course, pinpointing the first clinical seizure and therefore the onset of epilepsy in humans is difficult. French *et al.* highlighted clinically unremarkable signs (such as staring or lip-smacking) are typical human behaviours, and other subtle signs (such as non-convulsive seizures) are not recognised as epileptic until the emergence of convulsive seizures (French et al., 1993). As such, an alternative method for studying the progression of epileptogenesis is the use of animal models.

1.2.4. Animal models of epilepsy

Animal models have been vital in allowing researchers to investigate the disease processes of various conditions, and the mechanism(s) of potential therapeutics. A popular animal used in neuroscience research is the rodent. Despite a considerably different time scale for brain development between humans and rodent, the sequence of key events in brain maturation is comparable and there are distinct parallels in regional vulnerability and functionality (Semple et al., 2013). For example, adult hippocampal neurogenesis (AHN) was first identified in adult rodents (Kaplan and Hinds, 1977) and later confirmed in humans (Eriksson et al., 1998). However, a notable species difference in AHN of granule cells is the maturation of newly generated cells. These new granule cells of long-living organisms (i.e., humans, primates) will mature slower than that of rodents, meaning there is a prolonged period of higher excitability of these cells which has been proposed to have an evolutionary advantage to long-living organisms by permitting increased cognitive flexibility (Kohler et al., 2011, Moreno-Jiménez et al., 2021, Yuan et al., 2014). Hence, despite translatability of rodent to humans, age-dependent neurobiological developmental differences should always be considered.

Animal models of epilepsy can be induced *in vivo* using a variety of methods: chemoconvulsants (pilocarpine, kainic acid), electrical stimulation (electroshock-induced seizures, kindling), brain pathology (neonatal hypoxia, hyperthermic seizures, post-traumatic injury) and genetics (Genetic absence Epilepsy Rat from Strasbourg/GAERS) (Kandratavicius et al., 2014). One of the most popular methods for studying epileptogenesis is the pilocarpine method used to model TLE. Pilocarpine, a muscarinic acetylcholine agonist, was first demonstrated as a successful chemoconvulsant in 1983 by Turski *et al.* This led to rodents displaying behavioural and electrographic epileptiform activity in limbic structures accompanied by motor limbic seizures, limbic status epilepticus and widespread brain damage. Despite being an effective method for inducing epileptogenesis, the authors noted difficulty in survival rates of rodents, particularly of those with extensive damage to the hippocampus (Turski et al., 1983). Later studies using lower doses of pilocarpine still found high rates of mortality (average 38%, range 22% – 56%) (Curia et al., 2008), therefore questioning the validity of the pilocarpine model of TLE.

As such, researchers at Aston University, led by Professor Gavin Woodhall, developed a low morality, high morbidity refined version of the lithium-pilocarpine model of TLE termed the Reduced Intensity Status Epilepticus (RISE) model of epilepsy and epileptogenesis (Modebadze et al., 2016).

1.2.4.1. Reduced Intensity Status Epilepticus model of epilepsy

The RISE model of epilepsy is an effective model for studying TLE. With only 1% mortality rate, the morbidity of the model remains high and shows consistent features of epileptogenesis in humans, such as a lack of gross damage to the brain, progressive network alteration within the temporal lobe, electrophysiological features like *in vitro* recordings of human brain tissue,

and 40% - 100% of animals in any cohort (mean 69%) progressing into SRS. This reliable and repeatable method differs from the original lithium-pilocarpine method by the addition of 2.5 mg/kg xylazine once seizure severity of >3 on Racine's scale is reached (bilateral forelimb clonus with rearing). This muscle relaxant is an agonist of the α_2 adrenergic receptor which reduces the wild running and jumping behaviour in rodents associated with brainstem seizure activity, therefore reducing the risk of cardiorespiratory depression and death (Lertwittayanon et al., 2019). The other refinement was a cocktail of anticonvulsant/antiepileptic drugs (termed the 'stop' solution: 0.1 mg/kg MK-801, 2.5 mg/kg diazepam and 20 mg/kg MPEP) which results in rapid cessation of SE. This cocktail of drugs aims to increase overall inhibition within the brain, while decreasing excitation, therefore resulting in cessation of SE. Specifically, MK-801 is an NMDAR antagonist, diazepam is a positive allosteric modulator of the $GABA_A$ receptor, and MPEP is an antagonist of the metabotropic glutamate receptor mGluR5.

The reduced mortality rate and refined severity level means the RISE model fulfils at least two (refinement and reduction) of the 3Rs in line with the National Centre for Replacement, Refinement and Reduction guidelines (Modebadze et al., 2016). Hence, the work carried out in the thesis is a continuation of the current knowledge of epilepsy and epileptogenesis gained through studying the RISE model of TLE.

Studies examining the electrophysiological and receptor changes in the hippocampus which occur throughout epileptogenesis using the RISE model found reductions in spontaneous and evoked (using kainic acid) gamma oscillations during the latent period of epileptogenesis compared with control. However, following establishment of SRS, there appeared to be a substantial increase in gamma oscillatory power. Study of receptor expression in the hippocampus during the latent period of epileptogenesis found decreases in many excitatory ionotropic receptor groups, such as AMPAR subunits GluA1, GluA2, and GluA3; KAR subunits GluK2 and GluK5; and NMDAR subunits GluN1 and GluN2A. Also, reductions in the AMPAR accessory protein PSD-95 used for AMPAR trafficking and post-synaptic stabilisation was found. Following establishment of SRS, recovery to control values were observed in KAR subunits GluK2 and GluK5, and the NMDAR subunit GluN1. A substantial increase beyond control values was observed in PSD-95. However, chronic reductions in AMPARs subunits GluA1, GluA2 and GluA3; and NMDAR subunits GluN2A and GluN2B were observed following transition to SRS. Meaning, expression of some excitatory receptor groups in the hippocampus of RISE animals remain low even once animals transition into SRS. Importantly, the authors suggest this chronic reduction in AMPARs may underlie the transition into the SRS stage of epileptogenesis by causing a chronic imbalance between excitability and inhibition within the hippocampus (Modebadze et al., 2016, Needs et al., 2019).

1.3. Tianeptine

Given our understanding of network excitability and receptor expression using the RISE model of epileptogenesis in the hippocampus (Modebadze et al., 2016, Needs et al., 2019), targeting certain receptor groups could offer anti-epileptogenic therapeutic potential.

The atypical tricyclic antidepressant tianeptine (7-[(3-chloro-6-methyl-5,5-dioxo-11*H*-benzo[c][2,1]benzothiazepin-11-yl)amino]heptanoate), also known as Stablon, is used as a treatment for major depressive disorder and anxiety. Chronic administration of tianeptine has been found to increase GluA1 phosphorylation in both the frontal cortex and hippocampus, with a more pronounced effect in the CA3 subregion of the hippocampus than in CA1. Tianeptine also reduced stress-induced dendritic atrophy and modulates excitatory synaptic neurotransmission in CA3 of chronically stress rats (Kole et al., 2002, Magariños et al., 1999, Svenningsson et al., 2007).

Unlike typical antidepressants, such as selective serotonin re-uptake inhibitors (SSRIs), tianeptine does not bind to adrenergic, dopaminergic or serotonergic receptors or transporters (Kato and Weitsch, 1988). Instead, tianeptine is thought to potentiate AMPARs by activation CaMKII and PKA via various signalling cascades associated with synaptic plasticity (the p38, p42/44 mitogen-activated protein kinase (MAPK) and the c-Jun N-terminal kinase (JNK) pathway), and decreased surface diffusion of AMPARs by activation of CaMKII which leads to phosphorylation of AMPAR auxiliary subunit stargazin, with the resulting AMPAR-stargazin interaction forming a complex with PDZ scaffold proteins such as postsynaptic density 95 (PSD-95). This leads to immobilisation and anchoring of AMPARs in the postsynaptic membrane, meaning tianeptine increases both AMPAR channel conductance, and trafficking and stabilisation in the postsynaptic membrane (Szegedi et al., 2011, Zhang et al., 2013).

Also, studies have demonstrated that tianeptine is a full agonist of the mu opioid receptor (MOR). Widely expressed in the hippocampus, MOR is a Gi/o-coupled receptor, with presynaptic activation altering neuron excitability via suppression of presynaptic release of GABA. Activation of MOR requires a smaller concentration than that of glutamatergic receptors, meaning Gassaway *et al.* hypothesises that tianeptine's modulation of the glutamatergic system may occur indirectly, via opioid receptor signalling. For example, activation of MOR on CA1 inhibitory interneurons results in decreased activity, therefore disinhibiting CA1 glutamatergic neurons, resulting in enhanced excitability. As such, tianeptine may have several receptor targets within the hippocampus (Gassaway et al., 2014, Samuels et al., 2017, Svoboda et al., 1999).

1.4. Neurotransmitters and receptors

1.4.1. Glutamate

Glutamate is the most abundant excitatory neurotransmitter in the central nervous system (CNS) (Curtis and Watkins, 1960). Glutamate has a number of roles across the CNS but is particularly important for fast excitatory neurotransmission and neuronal excitability via Ca^{2+} influx (Hack and Balázs, 1994, Yano et al., 1998). However, excessive glutamate stimulation can cause excitotoxicity due to excessive cation influx, leading a cascade of events resulting in neuronal death and lysis (Rothman, 1985).

Glutamate binds to two major groups of membrane-bound receptors – ionotropic and metabotropic. Ionotropic receptors are cation-specific ion channels, including N-methyl D-aspartate (NMDA) receptors, α-amino-3-hydroxy-5-methyl-4-isoxazolepropionic acid (AMPA) receptors and kainic acid (KA) receptors (Eccles and Mcgeer, 1979). Metabotropic receptors are G-protein coupled receptors (GPCR) meaning binding of glutamate results in activation of intracellular signal transduction pathway(s) leading to production/modification of other proteins, including ion channels. The metabotropic group of receptors contains eight receptor subtypes split across three groups – group I (mGluR1/5), group II (mGluR2/3) and group III (mGluR4/6/7/8) (Bonsi et al., 2005). Interestingly, mGluR groups II and III are found primarily on axon terminals (presynaptic receptors) and suppress excitatory synaptic activity by suppressing glutamate release, therefore decreasing postsynaptic NMDA receptor activity and reducing the risk of excitotoxicity (Fagni et al., 2004, Grueter and Winder, 2005).

1.4.1.1. NMDA receptors

NMDA receptors (NMDARs) are di-heteromeric transmembrane ion channels consisting of four subunits derived from three families (NR1, NR2 and NR3, now termed GluN1, GluN2 (A – D) and GluN3 (A – B), respectively) (Collingridge et al., 2009). Commonly, two GluN1 (glycine-binding subunits) join with two GluN2 (glutamate-binding subunits) to form a functional dimer-of-dimers receptor (figure 1.2.). Different to other ionotropic glutamate receptors, NMDARs have a high permeability to Ca^{2+}, voltage-dependant Mg^{2+} block, and require binding of a co-agonist with glutamate (glycine or D-serine/D-alanine) for activation. Neuronal depolarisation by NMDAR activation results in excitatory postsynaptic potentials (EPSPs) (Kleckner and Dingledine, 1988, Traynelis et al., 2010).

NMDAR subunit composition is highly plastic, changing during neurodevelopment and according to neuronal activity. During neonatal synaptic maturation, there is a profound change from predominantly GluN2B-containing to GluN2A-containing NMDARs during the second postnatal week (Sanz-Clemente et al., 2013). This early expression of GluN2B-containing NMDARs confers to slower receptor decay kinetics (~280 ms compared to ~54 ms with GluN2A-containing NMDARs), leading to a >5 fold increased channel open time (Vicini et al., 1998). Furthermore, GluN2A-containing NMDARs have peak current densities which are

approximately four times larger than those of GluN2B-containing NMDARs, meaning peak charge transfer is enhanced. As a result, the predominance of GluN2B-containing NMDARs during early neurodevelopment allows for appropriate temporal integration of non-synchronous synaptic inputs, while this switch to GluN2A-containing NMDARs favours precise timing and rapid synchronous synaptic function (Chen et al., 1999).

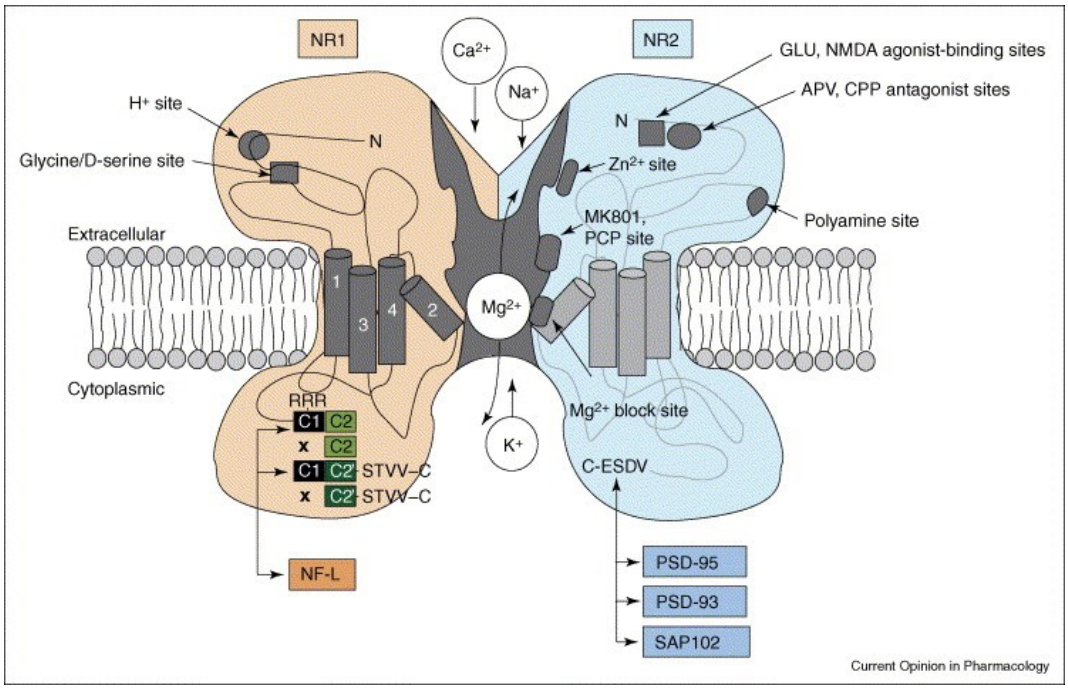

Figure 1.2. Schematic representation of the organisation/structure of an NMDA receptor (Kristiansen et al., 2007).

Illustration of the NMDAR with GluN1/NR1 and GluN2/NR2 subunits. N-terminus of the GluN1 shows H^+ binding site and glycine/D-serine binding site. C-terminus of GluN1 shows binding sites for intracellular proteins (e.g., NF-L). N-terminus of GluN2 shows agonist binding site (glutamate/NMDA) and antagonist binding site (D-2-amino-5-phosphono-valerate, APV and 3-(2-Carboxypiperazin-4-yl)propyl-1-phoshonic acid, CPP)). C-terminus of GluN2 shows Mg^{2+} blocking site and other protein/kinase binding sites (e.g., post-synaptic density protein PSD-95). Within the lumen of the channel shows the Mg^{2+} binding site and MK-801/PCP binding site, where direct flow of ions Na^+, Ca^{2+} and K^+ occurs.

A major role of NMDARs is synaptic plasticity. Increases or decreases in neuronal activity may cause a strengthening or weakening of synaptic strength. Increased synaptic strength is often referred to as long-term potentiation (LTP), whereas weakening is referred to as long-term depression (LTD). Particularly well documented in the hippocampus, LTP is considered one of

the major cellular mechanisms that underlies learning and memory (Ge et al., 2010, Whitlock et al., 2006). Although the mechanism(s) for NMDA-dependent LTP and LTD are still to be elucidated, it is thought similar but distinct mechanisms involve synaptic insertion and removal of AMPA receptors (AMPARs), respectively. For LTP, NMDAR activation resulting in a large influx of calcium will activate calcium/calmodulin-dependent kinase II (CaMKII), leading to increased AMPAR conductance and insertion of new AMPARs into the postsynaptic membrane, therefore increasing synaptic strength. Of course, this is simplified, with other kinases (e.g., cAMP-dependent protein kinase A and protein kinase A) are also believed to contribute to LTP. Although still under investigation, it is thought the tri-heteromeric GluN1/GluN2A/GluN2B NMDAR is critically involved in LTP induction at adult hippocampal CA3 – CA1 synapses (Paoletti et al., 2013). Inversely, LTD is thought to result from activation of protein phosphatases, such as the calcium/calmodulin-dependent protein phosphatase calcineurin and protein phosphatase 1 (PP1). Inactivation/internalisation of AMPARs this way leads to a reduced synaptic strength (Lisman, 1989, Lisman et al., 2002, Lu et al., 2001, Lüscher and Malenka, 2012).

1.4.1.2. AMPA receptors

AMPA receptors (AMPARs) are tetrameric transmembrane ion channels which mediate the majority of fast excitatory neurotransmission in the central nervous system. AMPARs consist of four groups of subunits (GluA1, GluA2, GluA3, and GluA4, previously GluR1-4) with assembly following a dimer-to-dimer formation (Dingledine et al., 1999, Greger et al., 2007). Although permeable to both Ca^{2+} and Na^{2+}, permeability to Ca^{2+} is mediated by the GluA2 subunit. Editing of GluA2 mRNA to replace glutamine for arginine at residue 607 (Q/R editing) (Sommer et al., 1991) by the enzyme adenosine deaminase acting on RNA 2 (ADAR2) leads to Ca^{2+}-impermeability. Thus, unedited or non-GluA2 containing AMPARs are important for Ca^{2+}-mediated depolarisation (Wright and Vissel, 2012).

Interestingly, there is evidence that AMPARs on hippocampal and neocortical principal cells (e.g., pyramidal cells) display low permeability to Ca^{2+} and desensitise relatively slowly (time constant of 10 – 15 ms), suggesting a predominance for GluA2-lacking AMPARs. Comparatively to hippocampal and neocortical GABAergic interneurons, which show faster desensitisation (3 – 6 ms) with increased sensitivity to Ca^{2+}, resulting in increased gating properties. This demonstrates neuron specific AMPAR subunit configuration patterns (Geiger et al., 1995, Hestrin, 1993, Jonas and Burnashev, 1995, Koh et al., 1995, Wenthold et al., 1996).

Desensitisation is a reduction in response to a sustained stimulus. Although seen in all glutamate receptors, this process is particularly fast in AMPAR, with >90% decrease in current amplitudes at steady state following a 20 ms stimulus (Traynelis et al., 2010). Occupancy of a single AMPAR subunit with glutamate is enough to trigger desensitisation which follows with two receptor confirmational changes that slow glutamate dissociation (figure 1.3.). These

conformational changes involve rearrangement and stabilisation of one subunit in each dimer into a partially closed conformation. Resensitisation follows disengagement of these stabilising interactions to allow rapid dissociation of bound glutamate, with an inverse rate of resensitisation to subunit occupancy, meaning AMPARs may re-enter desensitisation at different rates. Therefore, it is hypothesised desensitisation constrains membrane conductance by affecting neuronal excitability (Bowie and Lange, 2002, Robert and Howe, 2003).

Trafficking and anchoring of AMPAR is mediated by transmembrane AMPA receptor regulatory proteins (TARPs), including γ-2, γ-3, γ-4 and γ-8. Besides trafficking and anchoring, TARPS increase single channel conductance, increase activation rate, increase open probability, slow deactivation, and reduce desensitisation (Priel et al., 2006, Tomita et al., 2005, Yamazaki et al., 2004, Zhang et al., 2006).

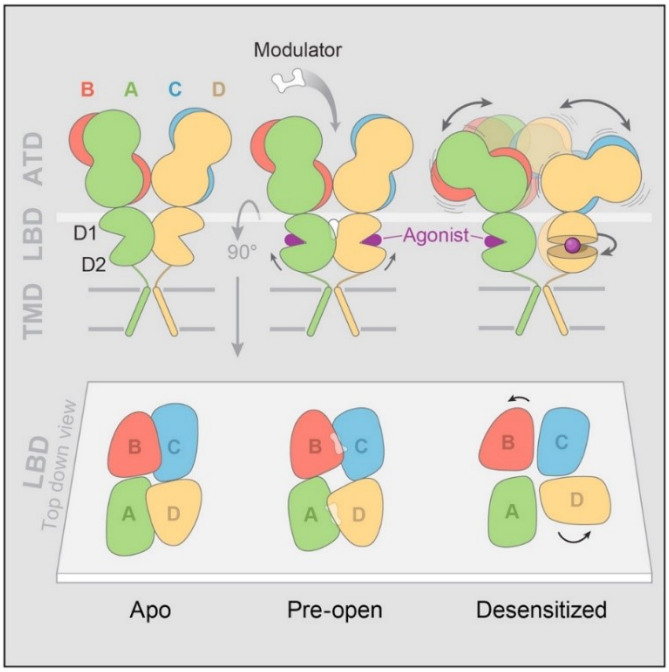

Figure 1.3. Schematic representation of the AMPAR structure and the confirmational changes which occur during desensitisation (Dürr et al., 2014).

Illustration of the AMPAR with the four subunits (A, B, C, D). Above: AMPARs harbour a modular architecture composed of an amino-terminal domain (ATD), an agonist-recognising ligand-binding domain (LBD) and the transmembrane domain (TMD). Binding of agonists occurs in the D1 and D2 lobes of the LBD. Middle illustration also shows the modulator and its binding site. Below: shows the top-down view of the receptor in its different shapes. Apo is the shape of the AMPAR under resting conditions. Pre-open shows the AMPAR in the presence of a positive allosteric modular, demonstrating a more open channel with increased probability of agonist binding. Desensitisation reveals a 90° confirmational rearrangement of subunits B and D at the ATD and LBD, leading to increased stabilisation and an overall reduction in conductance.

Glutamate-induced AMPAR desensitisation also increases their synaptic diffusion, therefore modulating short-term plasticity. AMPARs undergo constant movement, with ~50% continually cycling between synaptic and extrasynaptic sites by Brownian diffusion (random, microscopic movement of particles). It has been demonstrated that desensitisation of AMPARs with glutamate leads to increased AMPAR diffusion to allow for the rapid exchange of desensitised receptors by naïve ones in the synapse. The speed of this AMPAR diffusion is made possible by reduced interactions of the AMPAR-Stargazin complex with the postsynaptic scaffold protein PSD-95. Stargazin is involved in AMPAR stabilisation in the post-synaptic density (PSD) via its interaction with scaffolding proteins (e.g., PSD-95). When glutamate-induced AMPAR desensitisation occurs, the AMPAR-Stargazin complex will unbind from PSD to allow for rapid diffusion to extrasynaptic sites before being replaced with naïve AMPARs, thus allowing for maintenance of high-frequency synaptic transmission (Bats et al., 2007, Constals et al., 2015).

1.4.2. GABA

Gamma-amino butyric acid (GABA) is the chief inhibitory neurotransmitter in the mammalian CNS. Binding of GABA to its associated receptors results in hyperpolarisation and inhibition of action potential firing via inhibitory post-synaptic potentials (IPSPs). Like glutamate, GABA binds to both ionotropic and metabotropic receptors, named $GABA_A$/$GABA_C$ (also known as $GABA_A$-rho) and $GABA_B$, respectively. Ionotropic GABA receptors allow for fast inhibitory neurotransmission via Cl^- influx, leading to hyperpolarisation. Conversely, slow GABAergic inhibition is conducted by metabotropic $GABA_B$ receptors who supress neuronal Ca^{2+} conductance and activate inwardly rectifying K^+ channels, leading to hyperpolarisation (Bowery et al., 2002, Pin et al., 2004). GABA is synthesised from glutamate via the enzyme glutamic acid decarboxylase (GAD, two isoforms exist – GAD-65 and GAD-67). After use, GABA is then metabolised within the cell or in the synaptic cleft by GABA transaminase to form succinic semialdehyde dehydrogenase and then to gamma-hydroxybutyric acid (GHB) (Wong et al., 2003).

1.4.2.1. $GABA_A$ receptors

The $GABA_A$ receptor is a pentameric protein ion channel composed of five subunits (figure 1.4.) from 19 total identified subunits within eight groups - six α, four β, three γ, one δ, one ε, one π, one θ, and three ρ subunits (Olsen and Sieghart, 2008). Typically, the $GABA_A$ receptor contains two GABA binding sites and one benzodiazepine binding site. The GABA binding sites are located on the extracellular surface of the joining of the alpha and beta subunits (α-β interface), whereas the benzodiazepine binding site is located on the extracellular surface of the alpha and gamma subunits (α-γ interface). Ligands acting via the benzodiazepine binding site (e.g., diazepam) cannot directly open the channel, but only allosterically enhance (positive allosteric modular) or reduced (negative allosteric modular) GABA-induced currents (Sigel and Buhr, 1997). $GABA_A$ receptors can be located at synaptic, perisynaptic and extrasynaptic sites,

and can be found in non-neuronal cells outside of the nervous system (e.g. lung airway smooth muscle) (Mizuta et al., 2008).

Fascinatingly, during neonatal development, GABA plays the role of main excitatory neurotransmitter due to an inverted Cl^- gradient. Meaning, binding of GABA to $GABA_A$ causes depolarisation. Activation of $GABA_A$ receptors in the rat neonatal hippocampus causes activation of voltage-gated Na^+ and Ca^{2+} channels, potentiating NMDARs by removing their voltage-depending Mg^{2+} block (Leinekugel et al., 1999). This regulation is mainly dependent on the two co-transporters – K^+/Cl^- co-transporter KCC2 (chloride exporter) and $Na^+/ K^+/Cl^-$ co-transporter NKCC1 (chloride importer) – whose activity can decrease or increase neuronal Cl^- concentrations, respectively. NKCC1 is found predominantly during neonatal development, resulting in the high intracellular Cl^- concentration. Establishment of the glutamatergic system causes increased expression of KCC2 and formation of the normal Cl^- gradient, allowing for hyperpolarisation by Cl^- influx following $GABA_A$ activation. Altered expression and/or activity of either of these co-transporters has been associated with a variety of brain disorders including epilepsy, schizophrenia, and stroke (Schulte et al., 2018, Sieghart and Savić, 2018).

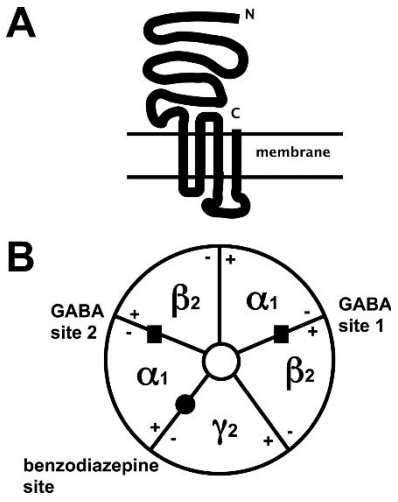

Figure 1.4. Schematic illustration of the major isoform of $GABA_A$ receptor (Sigel and Steinmann, 2012).

(A) Topology of a single subunit containing the extracellular N- and C-terminus and four transmembrane sequences (M1 – M4, M2 lines the ion channel). (B) Top view of the pentamer containing two α_1, two β_2 and one γ_2 subunits. Also contains two GABA binding sites (α-β interface) and a single benzodiazepine binding site (α-γ interface) within the Cl^- ion channel pore.

1.4.2.2. Inhibitory interneurons

Inhibitory interneurons are providers of inhibitory GABAergic synaptic input, with post-synaptic $GABA_A$ activation resulting in Cl^- influx and suppression of post-synaptic activation via

hyperpolarisation or shunting of the cell membrane. Local circuit inhibitory interneurons only represent ~10 – 15% of the total neuronal population with the rest comprising of excitatory pyramidal cells. However, these interneurons are responsible for countering excitation, and modulating the gain, timing, tuning, and bursting properties of principal cell firing. As such, exerting selective filtering of synaptic excitation. Interneurons are classified into five groups based on the expression of specific molecular markers: parvalbumin (PV), somatostatin, neuropeptide Y, vasoactive intestinal peptide, and cholecystokinin. PV-expressing basket cells are of significance within the hippocampus. These interneurons can contact 2,500 pyramidal cells with an average of six synapses onto each one. Primarily, PV interneurons innervate the perisomatic regions of principal cells. This is important for the generation of fast neuronal network oscillations, such as gamma, as fast-spiking interneurons (e.g., PV-expressing basket cells) fire at continuous high frequency (>50 Hz) resulting in larger hyperpolarising bursts. Following delay of this IPSP, local pyramidal cells can fire EPSPs, resulting in generation of coherent and synchronous network oscillations (Nahar et al., 2021, Pelkey et al., 2017, Roux and Buzsáki, 2015).

1.5. Neuronal network oscillations

Neuronal oscillations are rhythmic patterns of neural activity in the brain. Grouped by the frequency of voltage deflections per second (hertz, Hz), these include delta (0 – 3 Hz), theta (4 – 8 Hz), alpha (9 – 13 Hz), beta (14 – 24 Hz) and gamma (>25 Hz) (Roohi-Azizi et al., 2017) (table 1.1. adapted from (Abhang et al., 2016)). Neuronal oscillations are believed to support temporal representation and long-term information consolidation by temporally linking neurons into assemblies (binding theory), facilitating synaptic plasticity and allowing for bias input selection (Buzsáki and Draguhn, 2004).

Frequency band	Frequency (Hz)	Brain states
Delta	0.5 – 3	Sleep (non-REM)
Theta	4 – 8	Focused, activate motor behaviour, exploration
Alpha	9 – 14	Relaxed (with eyes closed), passive attention, drowsiness
Beta	15 – 24	Anxiety dominant, static motor control
Gamma	>25	Concentration, cognitive processes

Table 1.1. Common frequency bands within the brain and their functions.

The first recordings of electrical activity made directly from the cortex of mammals were conducted by Richard Caton in 1875. In 1929, German psychiatrist Hans Berger published the first non-invasive recordings of human brain activity (electroencephalogram, EEG), terming the waves ‘alpha’ and ‘beta’ and citing the importance of Caton’s pioneering work. Given the lack of diagnostic options during this period, the discovery of EEG revolutionised neurological and neurosurgical procedures, particularly for patients with seizures (İnce et al., 2021, Tudor et al., 2005).

Experimental and clinical recordings, such as EEG, are made possible because the field potential (synaptic activity) that is generated by the linear sum of numerous overlapping fields generated by current sources (current travelling from the intracellular space to the extracellular space) and current sinks (current travelling from the extracellular space to the intracellular space). In the case of an incoming EPSP, influx of Na^+ and Ca^{2+} ions at the dendrites via glutamatergic receptors (e.g., AMPA receptors) will form a sink. To maintain electroneutrality, a passive return current out of the cell will occur upstream (current source) to the dendrites (such as the soma), therefore forming a dipole between the dendrites and soma and leading to current flow across the membrane (figure 1.5.). Membrane currents will pass along the extracellular space between cells which will contribute to the perpetual voltage variability of the extracellular space. Besides synaptic activity, other non-synaptic events may contribute to the generation of local field potentials, including Ca^{2+} spikes, voltage-dependent oscillations, and spike afterpotentials (Buzsáki et al., 2012).

Oscillations of different frequencies are known to interact with each other, known as cross-frequency coupling (CFC). For example, this is commonly seen when the higher frequency gamma oscillation is ‘nested’ within the peak of the lower frequency theta oscillations – named phase-amplitude coupling. Meaning, inhibitory interneurons fire at gamma frequencies and their activity is phase-locked to the theta rhythm. This is most notably seen in the hippocampal perforant pathway, which can be entrained by inputs from the medial entorhinal cortex (Bragin et al., 1995).

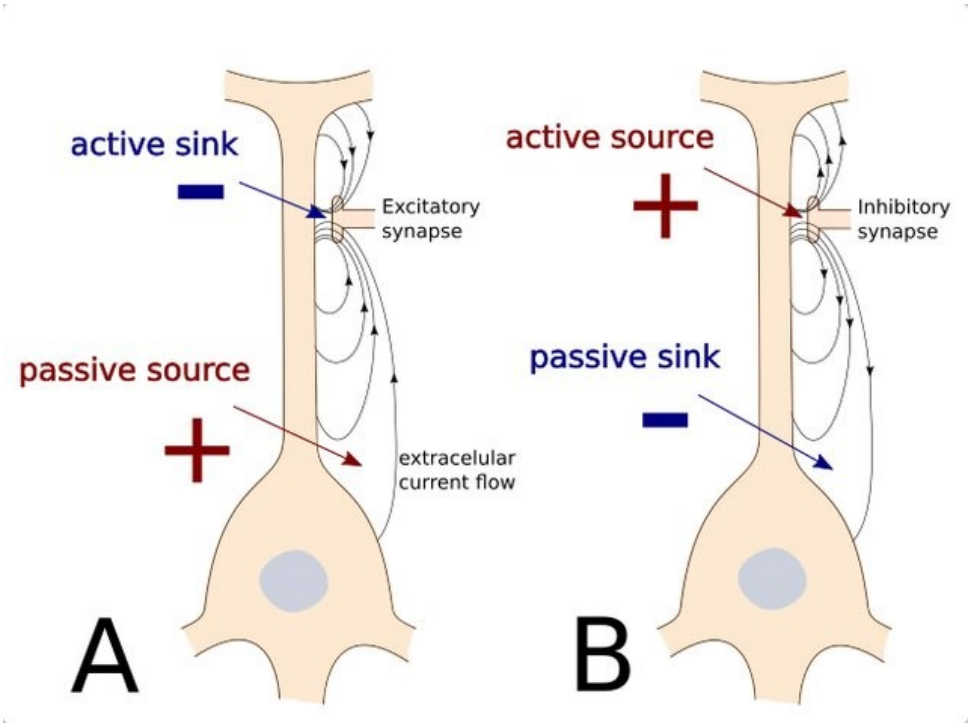

Figure 1.5. Illustration of current flow and the sink-source interaction (Maksymenko, 2019).

(A) Activation of excitatory synapses results in inward current flow at the level of the dendrite, resulting in membrane depolarisation and a net flow of positive current into the cell. This results in an active sink forming. Near the soma, a passive source forms resulting in extracellular potential of positive polarity. (B) Activation of inhibitory synapses results in an outward current flow at the level of the dendrite, resulting in membrane hyperpolarisation and a net flow of positive current out of the cell. This results in a passive sink at the level of the soma.

1.5.1. Gamma oscillations

Gamma oscillations are relatively high frequency rhythmic fluctuations believed to be important for a number of cognitive functions, including attention, memory and perception (Ray and Maunsell, 2015). Observed during both waking and sleep states, gamma rhythms are short-lived and are believed to emerge from the coordination of excitation and inhibition in the brain (Buzsáki and Wang, 2012).

Specifically, for memory retrieval and encoding, it is believed the coordination of slower (30 – 50 Hz) and faster (>50 Hz) gamma oscillations in the hippocampus are required, respectively. These faster oscillations can also interact with and be nested in slower, larger amplitude theta rhythms, allowing for synchronisation between distant networks (e.g., between the hippocampus and prefrontal cortex) (Colgin and Moser, 2010).

Aberrant gamma oscillations have been noted in a number of conditions, including epilepsy, schizophrenia and Alzheimer's disease (Uhlhaas and Singer, 2006). As such, this warrants

further investigation into the mechanisms of pathological gamma oscillations and their involvement in the development of neurological conditions.

The two favoured models for the generation of gamma oscillations are the interneuron network gamma (ING) model and pyramidal-interneuron network gamma (PING) model, both of which centre around postsynaptic $GABA_A$-mediated inhibition (Buzsáki and Wang, 2012). Other theories include the slowly inactivating K^+ currents with persistent Na^+ currents (Wang, 1993), and superficial pyramidal cells called 'chattering cells' in the cortex which can generate intrinsic gamma oscillations (Gray and McCormick, 1996).

1.5.1.1. ING model of gamma oscillations

The ING model of gamma oscillations explains how following activation of inhibitory PV+ interneurons, synchronised interneurons will begin discharging together to generate synchronous $GABA_A$-mediated IPSPs onto partner interneurons and neighbouring pyramidal cells, allowing for entrainment of pyramidal cell firing (figure 1.6.). These now inhibited partner interneurons will spike again following the decay of the $GABA_A$-mediated IPSP, and the cycle repeats. This model states the duration of the IPSP is determined by the subunit composition of the $GABA_A$ receptor, and the frequency of the oscillation is determined by the kinetics of the IPSP and the net excitation of interneurons.

Gamma oscillations can arise via two ways according to the ING model – via tonic or stochastic input. When input is tonic, the interneurons fire with well-defined periodicity. When input is stochastic, the interneurons fire irregularly until the whole network is activated and groups of neurons can randomly depolarise together to produce synchrony, thus allowing oscillations to emerge. When pyramidal cells and other interneuron typed are added to the ING model, the entire network can become phase-locked to the gamma oscillation (Buzsáki and Wang, 2012, Traub et al., 1996)

1.5.1.2. PING model of gamma oscillations

The more widely accepted PING model of gamma oscillations explains how an alteration between fast glutamatergic excitation and delayed feedback inhibition allows for the generation of fast oscillations (figure 1.6.). Pyramidal cells discharge which activates connected AMPARs on inhibitory (PV+) interneurons, leading to the generation of EPSPs, resulting in shunting (perisomatic) inhibition of pyramidal cells via $GABA_A$-induced IPSPs. Following decay of this $GABA_A$-mediated IPSP, the pyramidal cell can fire again, resulting in cyclic behaviour. A phase shift is produced due to the axon conduction and synaptic delays of approximately 5ms. The frequency of gamma oscillation is determined by the decay time of the IPSP (Buzsáki and Wang, 2012).

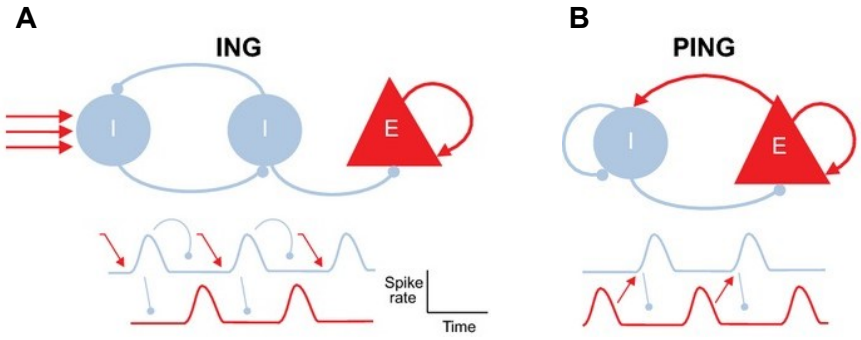

Figure 1.6. Schematic representation of the ING and PING models of gamma oscillations (Bosman et al., 2014).

(A) The ING model of gamma oscillations. Upper panel: following excitatory drive (red arrows on the left), mutual inhibition between interneurons is produced, resulting in rhythmic inhibition of pyramidal cell. Lower panel: shows the spike rate fluctuations between the two neuron groups. Excitation of interneurons results in reciprocal inhibition between interneurons, allowing pyramidal cells to fire. This period is determined by the recovery of the interneurons, thus leading to the emergence of gamma oscillations. (B) The PING model of gamma oscillations. Upper panel: excitatory pyramidal cell (E) and inhibitory interneuron (I) with reciprocal connections. Lower panel: shows the spike rate fluctuations between the two neuronal population groups (I in blue and E in red). Excitatory stimulation by pyramidal cell results in an increase in the firing rate of interneurons, leading to feedback inhibition. Following decay of this IPSP, the pyramidal cell can fire again, producing an oscillatory response.

Studies of *in vitro* and *in vivo* hippocampal gamma rhythms show evidence for the PING model of gamma oscillations. Pyramidal cells were shown to fire at ~3 Hz at the negative phase of the oscillation, with perisomatic inhibitory interneurons firing at ~18 Hz and were phase-coupled to the pyramidal rhythm (with a slight delay of ~2 ms). More distal interneurons, including dendritic and interneurons with cell body in the stratum radiatum, showed little to no phase relationship to the field oscillation. This shows two things: (1) pyramidal cells are not required to fire every cycle when entrained in the gamma rhythm, and (2) phase-locking of pyramidal neurons and perisomatic interneurons allows for synaptic feedback, as predicted by the PING model. Two gamma rhythm generators in the hippocampus were identified, being the dentate gyrus and CA3 (Bragin et al., 1995, Csicsvari et al., 2003, Hájos et al., 2004).

1.5.1.3. The role of glutamate receptors in gamma oscillations

AMPA receptors (AMPARs) drive the majority of fast excitatory neurotransmission in the brain, including in the generation of gamma oscillations. In the PING model of gamma oscillations, this AMPAR drive from pyramidal cells to interneurons would initiate the gamma oscillation, resulting in post-synaptic AMPAR activation, leading to EPSP generation and the influx of Na^+ and K^+ ions. This excitatory drive by AMPARs is so sensitive that the use of AMPAR antagonists, such as NBQX and GYK152466, has been shown to readily abolish *in vitro* gamma oscillations generated in the hippocampus (Fisahn et al., 1998, Mann et al., 2005) and

entorhinal cortex (Cunningham et al., 2003). Taken together these data suggest the central role AMPAR neurotransmission play in the generation and abolition of gamma oscillations.

Kainic acid (KA) receptors (KARs) are ubiquitously expressed throughout the hippocampus at both pre- and postsynaptic sites. A common method of generating persistent *in vitro* gamma oscillations is the bath application of 100 nM KA. Fiashn *et al.* studied the roles of KA-induced hippocampal gamma oscillations and found KA causes AMPAR-independent membrane depolarisation and an increase in action potential firing in both pyramidal cells and interneurons, leading to the generation of persistent gamma oscillations. However, as with the *in vivo* use of KA as a pro-convulsant, excessive KAR activation *in vitro* can lead to the generation of epileptiform activity. Meaning, small changes in overall activity can alter the balance between excitation and inhibition and cause the network to switch from gamma oscillations to epileptiform bursts (Fisahn et al., 2004).

There are varying reports on the role(s) of NMDA receptors (NMDARs) in gamma oscillations. However, these contradicting results are likely down to the region-specific effects, and the kinetics and concentration-dependent effects of the different antagonists studied. Studies have reported no significant effect on the power of induced gamma oscillations using the NMDAR antagonist D-AP5 (Mann et al., 2005), suggesting NMDARs are not necessary for the generation of gamma oscillations. A studying using a knockout animal model for schizophrenia also found no change in power of gamma oscillations in the hippocampus, but significant decreases in gamma power only in the superficial layers (layer II) of the medial entorhinal cortex (Cunningham et al., 2006). Acute NMDAR blockade with non-competitive NMDAR antagonists, namely ketamine, MK-801 and phencyclidine, offer a different story. Studies using these non-competitive NMDAR antagonists found increased gamma power in the hippocampus (Caixeta et al., 2013, Kehrer et al., 2007, Wang et al., 2020) and neocortex (McNally et al., 2011, Pinault, 2008).

A proposed mechanism for this increased gamma power seen in the presence of non-competitive NMDAR antagonists is, at resting membrane potential, NMDARs have a voltage-dependent Mg^{2+} block which prevents binding of NMDAR antagonists (e.g., ketamine) (Paoletti and Neyton, 2007). Due to the fast-spiking nature of PV+ interneurons, they are more likely to depolarise and be relieved of this Mg^{2+} block than regular spiking pyramidal cells, allowing for the binding of such open-channel, non-competitive NMDARs antagonists. As such, there will be preferential binding and blocking of NMDARs on PV+ interneurons, leading to disinhibition of recurrent pyramidal cells (Carlén et al., 2012). Hyperexcitability of pyramidal cells leads to increased activation of non-NMDARs (i.e., AMPARs and KARs), allowing for the potentiation of gamma oscillations (Grunze et al., 1996). An *in vivo* study by Carlén *et al.* supports this. Using an animal model of selective deletion of NMDARs on PV+ interneurons, these authors found enhanced cortical gamma oscillations and a deficit in gamma induction. This leads to behavioural disturbances associated with the development of schizophrenia (Carlén et al.,

2012). Altered NMDAR function and resulting aberrant gamma oscillations is heavily linked with the development of schizophrenia and schizophrenia-like symptoms (Krystal et al., 1994). As such, the role(s) of glutamatergic receptors in generation and maintenance of gamma oscillations has application in both physiology and pathology.

1.6. Aims and objectives

1. To further characterise the changes in brain excitability in the hippocampus throughout epileptogenesis, particularly during the latent period.
2. To investigate the effects of 10μM tianeptine on brain oscillations and synaptic activity.
3. To assess the use of tianeptine as an anti-epileptogenic drug for modifying the progression of epileptogenesis.
4. To assess seizure susceptibility of the RISE model of epilepsy throughout epileptogenesis.

Chapter 2 Methods

2.1. Animals and ethical approval

All procedures were carried out in accordance with the Animals Scientific Procedures Act (ASPA) 1986 UK, European Communities Council Directive 2010, and Aston University ethical review document.

2.2. Reduced Intensity Status Epilepticus model of epilepsy and epileptogenesis

The Reduced Intensity Status Epilepticus (RISE) model of epilepsy and epileptogenesis was created in our laboratory (Modebadze et al., 2016) as a low mortality, high morbidity modification of the pilocarpine model. In short, 24 hours prior to induction, the animals were treated with lithium chloride (LiCl, 127 mg/kg, SC). The use of LiCl reduces the dose of pilocarpine needed to induce SE by about 10-fold (Vezzani, 2009). On the day of induction, α-methyl scopolamine (1mg/kg, SC) was administered to reduce the peripheral effects of muscarinic cholinergic receptor activation with pilocarpine. Thirty minutes later, low dose pilocarpine (25 mg/kg, SC) was administered. Animals were then closely monitored for seizure activity using the Racine scale (table 2.1.) (Racine, 1972).

Racine seizure stage	Behavioural expression
0	No changes in behaviour
1	Mouth and facial movement
2	Head nodding
3	Unilateral forelimb clonus
4	Rearing and bilateral forelimb clonus
5	Rearing and falling with bilateral forelimb clonus – generalised motor convulsions

Table 2.1. The Racine scale of seizures (Racine, 1972).

Quantifiable means to describe seizure severity in rodents. Levels further down the Racine scale also contain symptoms of the previous stages.

Those rats who progress to stage 5, recovered, and entered stage 5 a second time (table 2.1.) were said to have entered status epilepticus (SE). To reduce seizure severity, xylazine (2.5 mg/kg, IM) was immediately administered. Those who failed to enter stage 5 within 30 – 45 min of pilocarpine administration were given a second dose. Animals then remained in xylazine-modified SE for no more than one hour, at which point seizure activity is terminated using 1 mg/kg (SC) ‘stop’ solution of MK-801 (0.1 mg/kg), diazepam (2.5 mg/kg) and MPEP (20 mg/kg). This cocktail of drugs aims to increase overall inhibition within the brain, while

decreasing excitation, therefore resulting in cessation of SE. Specifically, MK-801 is an NMDAR antagonist, diazepam is a positive allosteric modulator of the $GABA_A$ receptor, and MPEP is an antagonist of the metabotropic glutamate receptor mGluR5. Behavioural signs of SE ceased within 30 minutes and animals were closely monitored while allowed to recover on a heat pad with treats. 1 ml 0.9% saline with glucose SC also given to rehydrate animals. In most cases, animals regained normal behaviour within a few hours, with complete recovery within 12 hours.

Throughout this PhD, approximately 120 animals were used for induction of epileptogenesis using the RISE model. Of that, three animals died during the protocol. For studying the process of epileptogenesis, particular timepoints were used to study the latent period and seizure period (spontaneous recurrent seizures, SRS). For study of the latent period, timepoints of 2-, 3-, 4-, 5- and 6-weeks post-induction were used (AMC is p35 – p56). For SRS, seizure states were confirmed by visual confirmation and/or by using the Racine scale. Typically, animals were >3 months post-induction (AMC is >p98) (figure 2.1.).

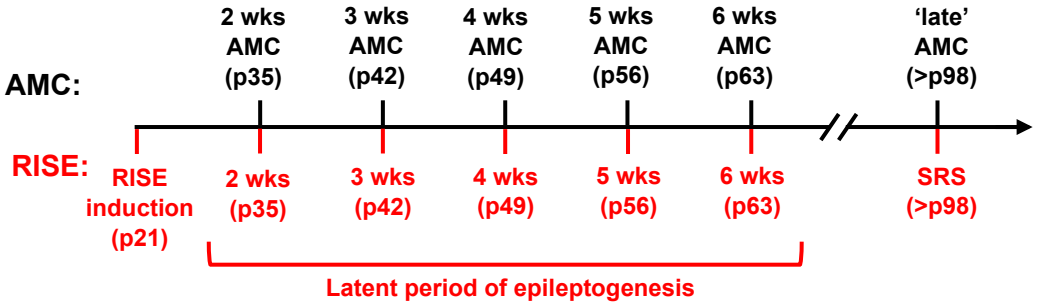

Figure 2.1. Timeline for *in vitro* extraction and experimentation for studying epileptogenesis in AMC and RISE animals.

Timepoints for extraction and experimentation for studying the timeline of epileptogenesis in control animals begins at approximately p35 (equivalent of 2 weeks post-induction in RISE animals). To study the weekly changes associated with the latent period in RISE animals, AMC animals were extracted each week up until p63 (6 weeks AMC). 'Late' AMC extraction and experimentation began after p98 to align with the emergence of SRS in RISE animals. In the RISE group, induction of epileptogenesis using the RISE model began at p21. Week-by-week extraction and experimentation of the latent period of epileptogenesis began at 2 weeks post-induction (p35) until 6 weeks post-induction (p63). Following behavioural confirmation of seizures, animals which entered SRS were extracted for experimentation beyond p98.

2.3. Behavioural experiments

2.3.1. Post-seizure behavioural battery test

The post-seizure behavioural battery test (PSBB) test was developed by Rice *et al.* as a way of quantifying behavioural changes seen in rats following induction of epileptogenesis using

pilocarpine-induced SE (Rice et al., 1998). The test involves gently prodding the animal ('touch') in the hindlimb with a blunt object (e.g., pen) and then attempting to pick the animal up around their body behind the forelimbs ('pick up'). The behavioural response was quantified (table 2.2.) and the two scores are multiplied to give a final total score. If this score is ≥10 for 4 sessions in a row that animal is deemed to be chronically epileptic and/or displaying spontaneous recurrent seizures (SRS). PSBB tests were performed twice weekly (typically Monday and Thursday).

Score	Touch	Pick up
1	No reactions	Very easy pick up
2	Rat turns towards instrument	Easy pick up (with vocalisations)
3	Rat moves away from instrument	Some difficult in pick up (rat rears and faces hand)
4	Rat freezes	Rat freezes
5	Rat turns towards the touch	Difficult pick up (rat moves away from hand)
6	Rat turns away from the touch	Very difficult pick up (rat behaves defensively or attacks hand)
7	Rat jumps (with or without vocalisations)	

Table 2.2. The PSBB test.

Scored behavioural aberrations to a touch- and pick-up test used for investigation of epileptogenesis in rats.

2.4. Brain slice preparation

Slices were prepared from male Wistar rats. Experimental objectives determined the age of animal used. For local field potential (LFP) recordings, 450 µm thick slices were prepared. For whole cell patch-clamp recordings, 350 µm thick slices were prepared.

To prepare for brain extraction, each animal was first anaesthetised using 5% isoflurane in N2/O2. Once anaesthetised, the animals were injected subcutaneously (SC) with pentobarbital (600mg/kg), and intramuscularly (IM) ketamine (100mg/kg) and xylazine (10mg/kg) to induce terminal anaesthesia and neuroleptanalgesia. Correct depth of anaesthesia was observed by absence of normal paw pinch and corneal reflex. Next, the animals were bathed in ice-cold

water for ~45 seconds before the transcranial perfusion was performed using 20 – 40ml ice-cold sucrose-based artificial cerebrospinal fluid (aCSF, cutting solution) containing (in mM): 180 sucrose, 2.5 KCl, 10 MgSO4, 1.25 NaH2PO4, 25 NaHCO3, 10 glucose, 0.5 CaCl2, 1 L-ascorbic acid, 2 N-acetyl-L-cysteine, 1 taurine and 20 ethyl pyruvate. Neuroprotectants were also added to the cutting solution to improve slice viability, including (in mM): 0.045 indomethacin (a cyclo-oxygenase (COX-2) inhibitor (Asanuma et al., 2001)), 0.2 aminoguanidine (a nitric oxide synthase (iNOS) inhibitor (Griffiths et al., 1993)), 0.4 uric acid (an anti-oxidant (Proctor, 2008)), 0.13 ketamine (non-competitive NMDAR antagonist (MacDonald et al., 1991)) and 0.2 brilliant blue G (a P2X7 antagonist and anti-inflammatory agent (Peng et al., 2009)). The complete cutting solution was saturated prior to perfusion with 95% O2/5% CO_2 (carbogen), pH 7.3, 300 – 310 Osm/L.

Follow rapid dissection and extraction of the brain, the brain was placed in the remaining cutting solution for transportation. Slicing was performed at room temperature in the ice-cold cutting solution using a 7000smz-2 model Vibrotome (Campden Instruments Ltd). Horizontal slices were made to contain the hippocampus and mEC. Slices were then transferred to the holding chamber and stored at room temperature for 1 hour in a standard aCSF containing (in mM): 126 NaCl, 2.5 KCl, 1 MgCl2, 2.5 CaCl2, 26 NaHCO3, 2 NaH2PO4 and 10 D-glucose. Neuroprotectants were also added (in mM): 0.045 indomethacin and 0.4 uric acid. Continual perfusion of 95% O2/5% CO_2 (carbogen) helped maintain pH 7.3, 300 – 310 Osm/L.

2.5. *In vitro* electrophysiology experiments

2.5.1. Extracellular recordings

Following one-hour recovery in the holding (interface) chamber, slices being used for extracellular recordings were transferred onto the LFP rig which contained an interface chamber (Scientific Systems Design Inc, Canada, figure 2.2.). Slices were continually perfused with saturated NaCl-based aCSF (95% O2/5% CO_2 (carbogen)) at a flow rate of 5 – 6 ml/min and temperature of 30 – 33°C using a proportional temperature controller PTC03 (Scientific Systems Design Inc, Canada). Microelectrodes were pulled from borosilicate glass (1.5mm diameter, Warner Instruments, USA) at a resistance of 3 – 5 MΩ using a PC-10 micropipette/microelectrode puller (Narishige Ltd, Japan). These microelectrodes were filled with NaCl-based aCSF and a chloride coated silver wire was inserted into the microelectrode, which was then placed in one of the four headstages.

Using an Olympus SZ51 (Olympus, UK) stereomicroscope for visualisation, the microelectrodes were lowered into the slice using the MM-3 micromanipulator (Narishige Ltd, Japan) with the aid of the rat brain atlas (Paxinos and Watson, 1998). Microelectrodes were

placed into hippocampal regions CA1 and CA3. Depending on the experiment, drugs were also bath applied and perfused onto the slices.

The voltage signal was first amplified x100 using an EX10-2F amplifier (NPI Electronics GMBH, Germany) with a high-pass filter of 0.1 Hz and low-pass filter of 1 KHz. 50 Hz electrical noise was filtered using Hum bugs (Quest Scientific, Canada). The signal was further amplified x20 using LHBF-48X amplifier (NPI Electronics GMBH, Germany) with a high-pass filter of 0.3 Hz and low-pass filter of 700 Hz, making a total signal gain of x2,000. The signal was then digitised at 5 KHz using a CED Micro1401-4 analogue-to-digital converter (Cambridge Electronic Design, UK) and recorded using Spike2 software (Cambridge Electronic Design, UK).

In short, the signal is a summation of transient fluctuations in extracellular ion concentrations. The generators of the LFP are local neuronal ensembles which produce current sinks (inward currents) and sources (outward currents) (Mitzdorf, 1985). These currents emerge mainly from synaptic activity (EPSP and IPSP), but with influences from Ca^{2+} spikes, other voltage-dependent intrinsic events, action potentials and spike after-potentials. So, LFP gives an insight into cooperative behaviour of neurons (Buzsáki et al., 2012). It is important to note the tip of the microelectrode has a recording area of approximately 250 μm (Katzner et al., 2009), meaning the sampling area is small, especially in comparison to other field recording techniques such as electroencephalography.

.

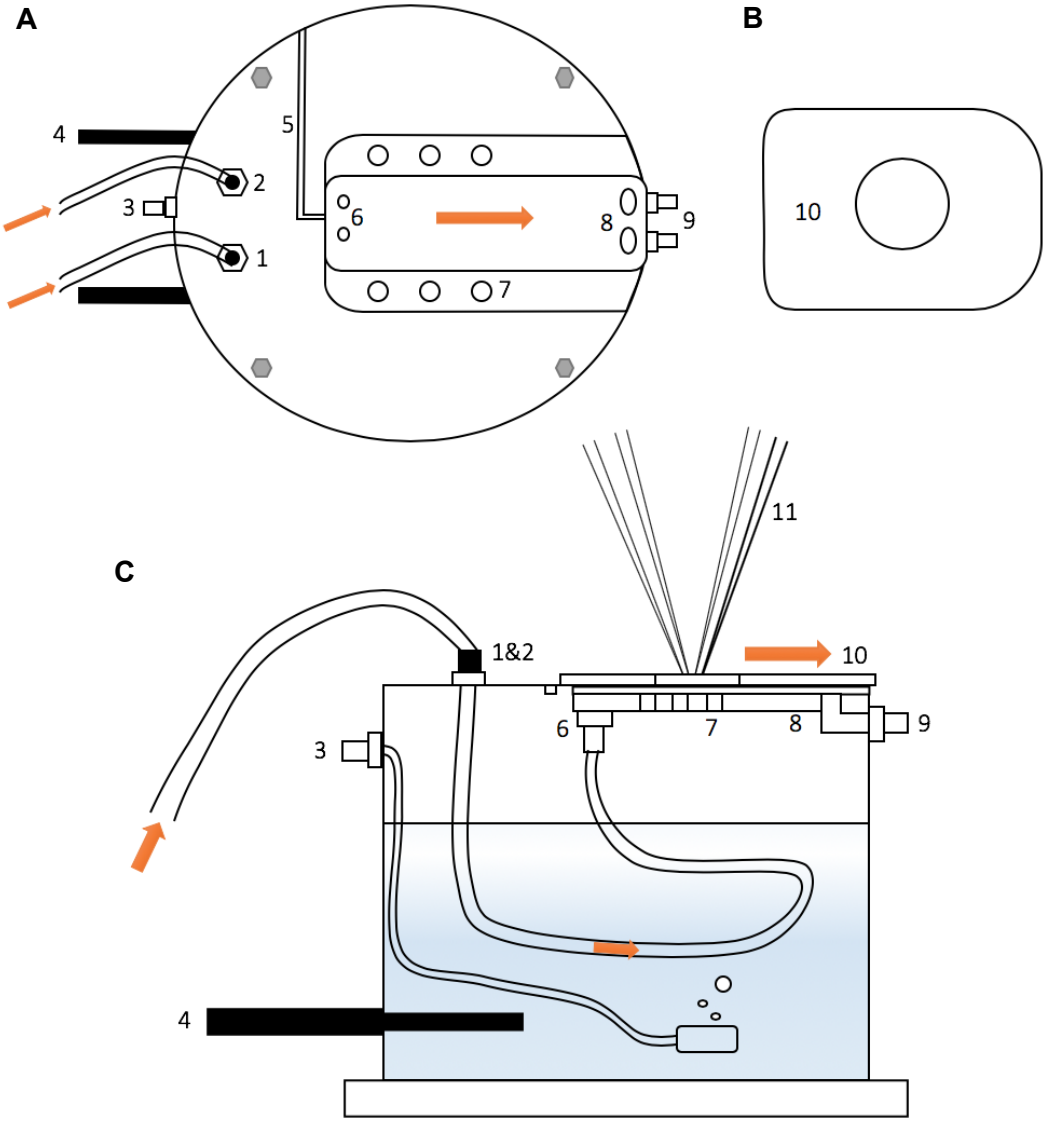

Figure 2.2. The local field potential interface recording chamber.

(A) Plan view of the interface chamber. aCSF (with circulating drugs) enters via points 1 and 2 before circulating into the inside of the interface chamber and exiting at point 6. Slice(s) are placed in the centre of the tray, and such will be saturated by the flow of aCSF. Point 3 shows the gas feed in connector. The two heater inputs/feedback centre are shown by point 4 which helps maintain the temperature between 30 – 33 ^{o}C. Point 5 shows the guide for the grounding wire. Six port holes (point 7) are for the rising humidified gas. Outflow is shown at point 8, which feeds into the drippers at point 9 and allows for recirculation of the aCSF. (B) Acrylic lid which is placed over the slice(s). The central hole allows for microelectrode access. (C) Side view of diagram A. Also shows water level within the interface chamber, which is bubbled with carbogen via the gas feed in point 3. The perfusion solution feed (1 & 2) feeds into the water to warm up the aCSF. Up to four microelectrodes (11) were inserted into the slice(s) at once via the hole in the acrylic slide (10). Orange arrows show the direction of flow.

2.5.2. Intracellular recordings

Whole cell patch-clamp experiments were conducted to understand aberrant ion channel behaviour in the temporal lobes associated with epileptogenesis. Whole cell voltage-clamp involves holding a cell at a particular membrane potential (mV) to measure the current (flow of ions, pA) through the ion channels. Ion channel activation by neurotransmitters causes ion influx across the membrane, and due to the voltage clamp, the current required to negate such flux acts as a proxy measurement for the synaptic currents generated by receptor activation. Hence, voltage clamp circuity will pass a current equal and opposite to the current through the channels to maintain the clamped membrane potential. This is displayed as 'events'. Although an effective method for studying ion channel behaviour, a disadvantage of the voltage clamp technique is space clamp. Meaning, the incapability for full voltage control of electrotonically distant parts of the cell (Jones, 1990).

Borosilicate capillary glass micropipettes were pulled using a P-1000 Micropipette Puller (Sutter Instruments, USA) with a tip resistance of 3 – 6 MΩ. Depending on the objectives of the experiments, these electrodes were filled with an internal solution specific for recording either spontaneous inhibitory postsynaptic currents (sIPSC) or spontaneous excitatory postsynaptic currents (sEPSC). Composition of sIPSC (in nM): 100 CsCl, 40 HEPES, 1 QX-314, 0.6 EGTA, 5 $MgCl_2$, 10 TEA-Cl, 80 ATP-Na, 6 GTP-Na, 1 IEM1460. Composition of sEPSC (in nM): 100 D-Gluconate, 40 HEPES, 1 QX-314, 0.6 EGTA, 2 NaCl, 5 Mg-Gluconate, 5 TEA-Cl, 10 Phosphocreatine, 4 ATP-Na, 0.3 GTP-Na. Both internal solutions had a final osmolality of 285 mOsmol and pH 7.3.

Like LFP experiments, following the one-hour acclimatisation period, slices were transferred to the patch clamp rig and recordings were performed in a submerged chamber. Temperature of the circulating ACSF was maintained at ~30 ^{o}C using a TC-324C Single Channel Temperature Controller (Warner Instruments, USA). Filled electrodes were attached to a CV 203BU head stage (Molecular Devices, USA) which was controlled using PatchStar Micromanipulator (Scientifica, UK). Basler Ace 2.3 MP PowerPack Microscopy camera (Basler, Germany) is used for visualisation of target cells. Once an appropriate cell was identified and the electrode is lowered to just above the cell, a seal was formed between the membrane and the electrode, and a resistance of at least 1 GΩ (GigaOhm) was achieved before breaking through. Upon breaking through, a seal test (5 mV pulse) was applied for 10 minutes to allow for adequate filling of the cell with the internal solution and space-clamp. An Axopatch 200B Microelectrode Amplifier (Molecular Devices, USA) was used to hold cells at -70 mV. After filling, at least 5 minutes of baseline was recorded before the bath application of drugs. A seal test was applied every 5 minutes to monitor any changes in the access resistance. Any recordings where the seal test altered >30% of the original access resistance

were discarded. Large changes in access resistance could alter the amplitude and kinetics of the events, therefore undermining the effect of any drugs, making the results invalid.

Data was acquired using Clampex 10.7 software with a sampling rate of 10 KHz and filtered at 2 KHz which was digitised using a Digidata 1440A. Data was analysed using Clampfit 10.7, GraphPad prism 8 and Microsoft Excel.

2.6. Data collection and analysis

2.6.1. LFP data analysis

All LFP data was analysed in Spike2 (version 7.10c, Cambridge Electronic Design) and extracted for storage/further analysis in Microsoft Excel or GraphPad Prism (version 8.0.1). All statistical analysis was performed in GraphPad Prism. Due to the nonparametric nature of much of the data, for analysis comparing just two groups, the Mann-Whitney test was employed for unpaired groups and the Wilcoxon matched-pairs signed rank test was employed for paired groups. For analysis of multiple groups, Friedman's test with Dunn's multiple comparisons post-hoc test was employed. * denotes $p \leq 0.05$, ** denotes $p \leq 0.01$, and *** denotes $p \leq 0.001$. All data in this thesis is expressed as mean ± standard error of the mean (SRS).

2.6.1.1. FFT algorithms

Fast fourier transform (FFT) is a measurement method which converts a signal from its original waveform to a power spectrum separated into discrete frequency bins. The in-built FFT algorithm in Spike2 was used to generate FFTs to examine power-frequency components of oscillations during experiments. Typically, two-minute (120 second) epochs were used for analysis at the end of each (drug) condition, before being transferred to Microsoft Excel or GraphPad Prism for further analysis.

2.6.1.2. Peak gamma power

Following the generation and extraction of FFTs for appropriate drug or time conditions, pooled data is transferred to GraphPad Prism for further analysis. To maintain consistency, FFTs of 0 – 100 Hz were transferred. For analysis of peak raw power within the gamma frequency range, a manual bandpass of 15 – 49 Hz was employed in GraphPad Prism. Area Under Curve (AUC) analysis allows for extraction of peak raw power, AUC, and peak frequency of the gamma oscillation (figure 2.3.). Normalisation of data was then possible by calculating the change from the starting value (taken as 100%). Statistical analysis was then performed was mentioned above.

For extraction and presentation of raw data, data was filtered directly in Spike2 using the infinite impulse response (IIR) filter at a bandpass of 20 – 49 Hz to isolate the gamma oscillation. IIR was chosen over a finite impulse response (FIR) due to ease and computational efficiency.

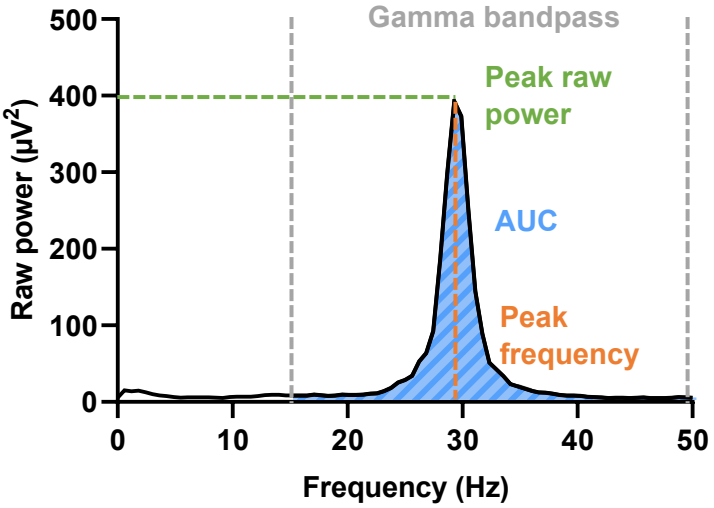

Figure 2.3. An example FFT showing analysis parameters for studying gamma oscillations.

An example FFT extracted from Spike2 showing a gamma oscillation generated by bath application of 200nM KA in hippocampal region CA3. A manual gamma bandpass can be generated in GraphPad Prism to isolate 15 – 49 Hz (grey). AUC analysis (blue), peak raw power (green) and peak frequency (orange) can then be achieved.

2.6.1.3. Seizure-like activity *in vitro*

All seizure-like activity (SLA) was analysed in Spike2 and transferred to GraphPad Prism for further analysis. To be considered for analysis, SLA (or 'seizures') had to be ≥10 seconds in length and have a characteristic shape (increasing pre-ictal spiking before a sharp transition into high power, repetitive discharging which subsides within 10 – 180 seconds) (figure 2.4.). Manual analysis and extraction were performed to examine: (1) percentage of slices to seize overall, (2) time to first seizure (seconds), (3) total number of seizures (count), (4) duration of seizures (seconds) and (5) inter-seizure interval (ISI, seconds). Again, statistical analysis was then performed was mentioned above.

For extraction and presentation of raw data, no filtering was performed prior to extraction to preserve the true shape and characteristics of the SLA.

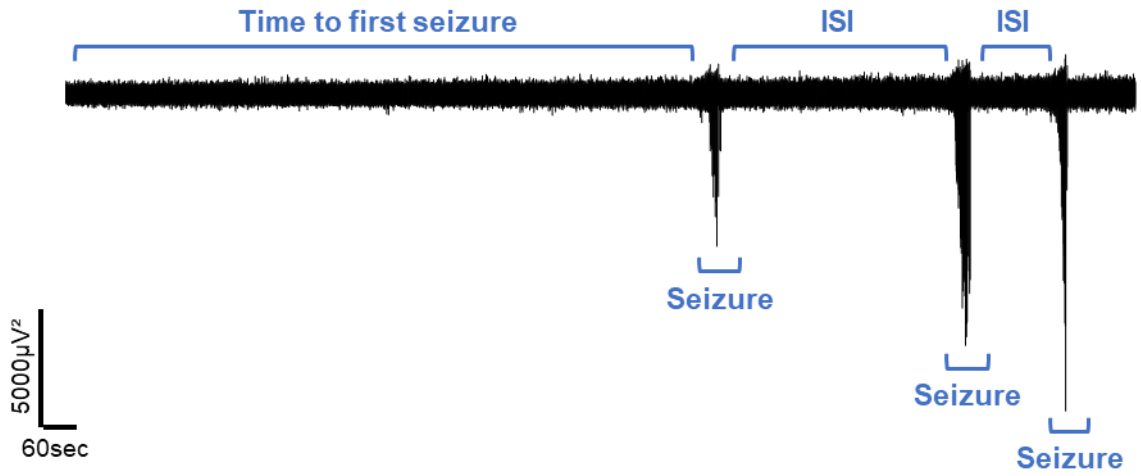

Figure 2.4. An example of a section of trace showing seizures in CA1 *in vitro*.

An example of a typical seizure generation in CA1 of a RISE animal in the SRS stage of epileptogenesis following introduction of 0 Mg^{2+} ACSF. This allows for analysis of certain parameters for studying brain slice excitability and susceptibility to seizure generation: time to first seizure (s), inter-seizure interval (ISI, s), and seizures (total seizure count/frequency and duration of seizures).

2.6.2. Patch clamp data analysis

All patch clamp data was analysed in ClampFit (version 10.4.2.0, Molecular Devices) and extracted for storage/further analysis in Microsoft Excel or GraphPad Prism (version 8.0.1). For event detection, an event template of ~5 example events were created before template search could commence. For each condition, 200 events were extracted. For effectively analysis, amplitude (pA), decay tau (ms), and inter-event interval (IEI, ms) were used. Again, data was transferred for statistical analysis in GraphPad Prism.

2.7. Drugs

Stock solutions of drugs were prepared at known concentrations by diluting drugs with water, DMSO or ethanol depending on the solubility. Drugs were stored at -20 °C before use and were kept for no longer than 12 months. All drugs were purchased from Sigma, Tocris or Abcam. Drugs used for *in vitro* experiments were applied directly to the aCSF cylinder for bath perfusion and allowed to circulate for at least 30 minutes. All drugs and their final concentrations are detailed in table 2.3.

Drug	Final concentration
Kainic acid (KA)	200nM
Tianeptine	10μM
D-AP5	50μM
Corticosterone	10μM
s-AMPA	1μM

Table 2.3. All drugs and the final concentrations used *in vitro*.

Chapter 3 Modelling the progression of epileptogenesis *in vitro*

3.1. Introduction

3.1.1. Current understanding of epileptogenesis using the RISE model of epilepsy

It is now accepted that epilepsy is not an acute process which happens overnight. When a seizure first appears, it reflects an underlying process that may often lead to a second such event, and seizures themselves would appear to be involved in increasing the likelihood for future seizures. As Sir William Gowers noted, 'seizures beget seizures' (Gowers, 1901). More recently, the term 'epileptogenesis' has been coined to describe the process that underlies the establishment of epilepsy, turning normal circuits into epileptogenic ones.

Our laboratory has previously shown that epileptogenesis involves dynamic changes in the function of hippocampal and parahippocampal networks, mediated by alterations in expression of various receptors and ion channels (e.g., chronic reductions in AMPAR subunits GluA1, GluA2 and GluA3). For example, previous research exploring epileptogenesis using the RISE model investigated specific timepoints in the progression of the disorder – status epilepticus (SE, 24 hours post-induction), latent period (weeks 2 – 4 (as studied in Needs *et al.*) and weeks 5 – 6 (as studied in Modebadze *et al.*) post-induction) and spontaneous recurrent seizures (SRS, >3 months post-induction). Electrophysiological and molecular biology techniques were employed to examine brain excitability and protein/receptor expression across the temporal lobe at these stages of epileptogenesis. Work on the early post status epilepticus (SE) stage of epileptogenesis found no significant difference in gamma power between age matched controls (AMC) and RISE animals, showing the excitatory-inhibitory balance required to generate coherent, spontaneous network gamma activity remained intact during the early stages of epileptogenesis (Modebadze et al., 2016, Needs et al., 2019).

However, work on the latent period found a different story. Significant reductions in the power of spontaneous gamma oscillations *in vitro* were observed at 5 – 6 weeks post-induction (Modebadze et al., 2016). Similar deficits in spontaneous gamma oscillations were shown at 2 – 4 weeks into the latent period, with profound deficits in network excitability also seen when the brain slices were challenged with 100nM kainic acid (KA). Significant decreases in some AMPAR subunits (GluA1, GluA2, GluA3) and the NMDAR subunit GluN2A were also observed in the hippocampus during the latent period. Based on these data, it was hypothesised that decreased AMPAR and KAR expression in the hippocampus causes this profound decrease in network excitability during the latent period (Needs et al., 2019).

Interestingly, following the establishment of SRS, hippocampal subregion CA3 was still spontaneously active when compared to AMC. Following bath application of 100nM KA, there were significant increases in gamma power in comparison to AMC, suggesting elevated excitability in CA3. Furthermore, spontaneously generated ictal-like discharges in the hippocampus and medial entorhinal cortex were commonly observed, with authors hypothesising this increased excitability during SRS may be linked to the appearance of

behavioural seizures. Despite this, the AMPAR and NMDAR subunits lost during the latent period did not recover during SRS, meaning brain slice excitability apparently increased in the absence of the return or re-expression of key glutamatergic receptors (Needs et al., 2019).

These initial studies were of significant interest given that we now understand that glutamate receptors undergo plastic change both at individual synapse level (LTP, LTD) and more globally (synaptic scaling). However, we did not have detailed data on the time course of the processes we were investigating. As such, the first results chapter of this thesis is dedicated to exploring the week-by-week changes which occur in the hippocampus during the latent period using the *in vitro* electrophysiology techniques local field potential (LFP) and whole-cell voltage clamp recordings. Latent period weeks 2 – 6 (P35 – P63) and SRS (>3 months) were explored. The very early stages of epileptogenesis (SE and 1-week post-induction) were not explored as previous research found no noticeable network and molecular changes (Modebadze et al., 2016, Needs et al., 2019). For LFP experiments, a similar protocol for measuring network excitability was employed by using the KA-challenge model.

3.2. Results

3.2.1. Network excitability – spontaneous local field potential oscillations in epileptogenesis

Horizontal hippocampal-entorhinal slices were prepared from AMC and RISE-induced rats during timepoints for the latent period (weeks 2, 3, 4, 5, and 6 post-induction) and SRS (>3 months post-induction) using the standard LFP method (chapter 2.5.). When low resistance (2 – 10 MOhm) glass microelectrodes were inserted into the cell body layers, healthy brain slices readily generated spontaneous gamma oscillations in both CA1 and CA3 region of the hippocampus. Two analysis parameters were examined to assess the differences in network excitability – peak raw power of the oscillations and area under the curve (AUC). The first measure captured the peak power and frequency of gamma oscillations and is a standard measure for oscillatory activity. Due to the propensity for gamma activity to vary in peak frequency between RISE and AMC networks, a second, more holistic measure of overall oscillatory power was made by calculating the AUC of a 15 – 49 Hz band that is often referred to as beta-gamma. However, is it worth nothing that, in some cases, spontaneous gamma oscillations were not generated in RISE animals, particularly during the later stages of the latent period. Meaning, to maintain consistency across this thesis, the term ‘spontaneous gamma oscillations’ is used throughout which includes instances of no defined gamma peak (which could also be termed ‘spontaneous activity in the gamma band’).

As noted above, we set out to plot the time course of changes that lead to a collapse in network oscillatory function in the RISE model during the latent period. Rats were taken at 2, 3, 4, 5, and 6 weeks post-induction, and again once epilepsy had become established (SRS

timepoint). Control (AMC) slices were taken at similar timepoints. Following stabilisation of spontaneous gamma band activity for at least 30 minutes, 200nM KA was added for a further 30 minutes minimum. As can be seen in figure 3.1., spontaneous gamma oscillations were readily generated in both CA1 (figure 3.1. Ai, Bi) and CA3 (figure 3.1. Aii, Bii). Across both parameters, there were no significant differences in spontaneous network excitability between AMC and RISE during the early stages of the latent period (weeks 2 and 3 post-induction). By week 4, CA1 saw a considerable difference in spontaneous gamma oscillations, with peak gamma power being significantly higher in AMC (figure 3.1. Ai, 6.5 ± 2.8 μV^2, n = 15, $p \leq 0.05$) compared with RISE (1.4 ± 0.3 μV^2, n = 22). The same trend was observed in CA1 4 weeks post-induction using AUC analysis (figure 3.1. Bi), with spontaneous gamma oscillations being significantly higher in AMC (75.6 ± 24.7, $p \leq 0.05$) than RISE (19.7 ± 3.2). This deficit in spontaneous gamma oscillations in RISE at week 4 post-induction was also observed in CA3 (figure 3.1. Aii, Bii). Peak gamma power was significantly higher for AMC (figure 3.1. Bi, 63.3 ± 18.9 μV^2, n = 16, $p \leq 0.05$) than RISE (15.8 ± 4.1 μV^2, n = 20). AUC exhibited the same findings, with AMC (figure 3.1. Bii, 537.7 ± 128.6, n = 15, $p \leq 0.01$) being substantially higher than RISE (143.2 ± 37.6, n = 21). These results show the deficit in spontaneous network excitability begins as early as 4 weeks post-induction and occurs simultaneously in both CA1 and CA3.

This loss of network excitability and the inability to generate spontaneous gamma oscillations in the hippocampus of RISE animals continues into week 5 post-induction. For CA1, both peak gamma power (5.9 ± 3.8 μV^2, n = 17 vs 0.5 ± 0.1 μV^2, n = 20, $p \leq 0.001$, AMC vs RISE respectively) and AUC (81.1 ± 43.4, n = 17 vs 7.9 ± 1.9, n = 20, $p \leq 0.01$, AMC vs RISE respectively) are significant reduced in RISE. The same is true for CA3, both peak gamma power (38.9 ± 10.3 μV^2, n = 19 vs 5.5 ± 4.2 μV^2, n = 20, $p \leq 0.001$, AMC vs RISE respectively) and AUC (311.2 ± 87.8, n = 19 vs 31.3 ± 19.4, n = 20, $p \leq 0.001$, AMC vs RISE respectively) showing the largest difference in network excitability between AMC and RISE. Week 5 post-induction appears to show the most consistent loss of network excitability in RISE across both parameters in both CA1 and CA3. Similar trends for week 6 post-induction were seen throughout CA1 and CA3.

Interestingly, there appears to be some recovery in network excitability and the ability to generate spontaneous gamma oscillations in the hippocampus of RISE animals when they are in the SRS stage. In CA1, the recovery in peak gamma power of RISE (4.4 ± 2.0 μV^2, n = 16) is comparable to that of AMC (1.8 ± 0.3 μV^2, n = 18, p = ns). Although the gamma power of RISE is notably higher than AMC, this was non-significant. The same is true for AUC, with RISE (20.7 ± 5.9, n = 15) regaining spontaneous network excitability to AMC (22.5 ± 4.0, n = 18, p = ns). In CA3, the recovery in peak gamma power of RISE (71.7 ± 22.9 μV^2, n = 15) is like that of AMC (61.1 ± 22.2 μV^2, n = 18, p = ns). This is also seen in AUC, with RISE (456.6 ± 121.5, n = 15) recovering to that of AMC (346.9 ± 126.4, n = 18, p = ns).

Overall, this shows there is a loss of network excitability and spontaneous gamma oscillations in the hippocampus during the latent period, which is first present at week 4 post-induction and most significant by week 5. There appears to be recovery in the ability to generate gamma oscillations once epileptic animals reach the SRS stage of epileptogenesis despite animals now presenting with clinical seizures. This demonstrates that there are ongoing network and receptor changes occurring throughout the different stages of epileptogenesis which may drive the progression into clinical seizures.

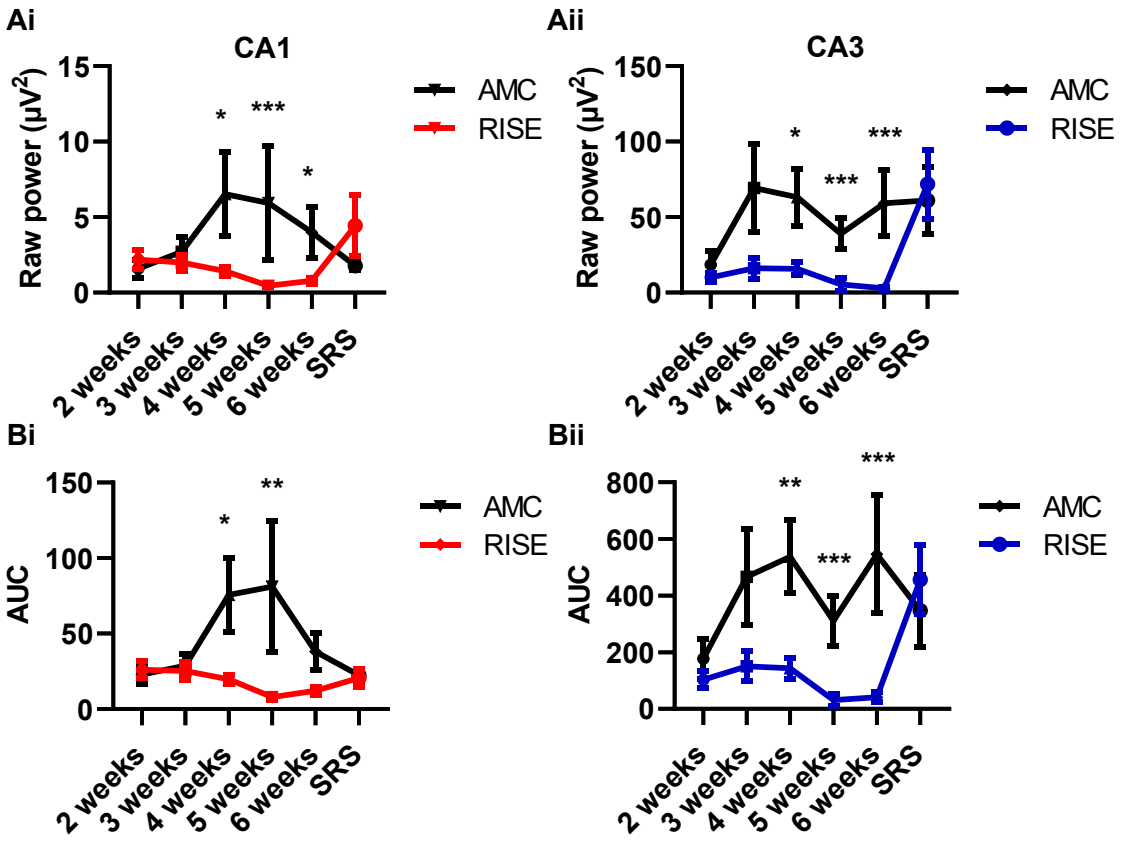

Figure 3.1. Comparison of spontaneous network excitability in the hippocampus throughout epileptogenesis for AMC and RISE.

Connected column mean graphs of weeks 2, 3, 4, 5, 6 and SRS (>3 months) post-induction. (A) Graphs Ai and Aii show raw peak power (μV^2) for CA1 and CA3, respectively. (B) Graphs Bi and Bii show AUC analysis for CA1 and CA3, respectively. A manual band-pass of 15 – 49 Hz was used to isolate gamma oscillations. Red (left) represents CA1 and blue (right) represents CA3. Error bars show SEM. * denotes $p \leq 0.05$, ** denotes $p \leq 0.01$ and *** denotes $p \leq 0.001$ (Mann-Whitney test).

3.2.2. Network excitability – kainic acid-induced local field potential oscillations in epileptogenesis

A key approach to assessment of network excitability developed in our laboratory is the *in vitro* KA-challenge model. Here, once spontaneous oscillations had been recorded, K was applied to the network and allowed to reach maximum power. The percentage increase in oscillatory power between spontaneous and KA-induced gamma was then calculated and used as an index of synaptic excitability. Similar to previous research using the RISE model (Modebadze et al., 2016, Needs et al., 2019), 200nM KA was bath applied to AMC and RISE brain slices at the different stages of epileptogenesis (weeks 2, 3, 4, 5, 6 and SRS) to assess network responsiveness to AMPAR and KAR stimulation. Like spontaneous network excitability (figure 3.1.), there were no differences in KA-induced gamma oscillations between AMC and RISE in the initial stages of epileptogenesis (weeks 2 and 3, figure 3.2.). Differences in KA-induced network excitability between AMC and RISE begin at week 4, however this is only shown to be significantly different in CA1 using the AUC analysis (figure 3.2. Bi, 518.3 ± 167.9, n = 6, $p \leq 0.01$ for AMC vs 157.9 ± 32.1, n = 12 for RISE).

By week 5, all measured parameters in both CA1 and CA3 revealed a significant difference in KA-induced network excitability between AMC and RISE. In CA1, raw gamma power was significantly higher in AMC (figure 3.2. Ai, 26.1 ± 8.4 μV^2, n = 7, $p \leq 0.001$) compared to RISE (1.6 ± 0.5 μV^2, n = 10). The same was seen for AUC (figure 3.2. Bi, 261.3 ± 83.0, n = 7, $p \leq 0.01$ for AMC, and 29.8 ± 10.2, n = 10 for RISE). In CA3, a similar consistent loss of KA-induced network excitability was seen. Raw gamma power was significantly higher in AMC (figure 3.2. Aii, 157.0 ± 49.2 μV^2, n = 8, $p \leq 0.001$) compared to RISE (9.9 ± 4.2 μV^2, n = 10), and the same for the AUC analysis (figure 3.2. Bii, 3283 ± 1610, n = 9, $p \leq 0.001$ for AMC, compared to 82.6 ± 36.3, n = 10 for RISE). Similar trends for week 6 post-induction were seen throughout CA1 and CA3.

Parallel to spontaneous network excitability, there appears to be recovery in responsiveness to KA once RISE animals move into the SRS stage in both CA1 and CA3. In CA1 (figure 3.2. Ai, Bi), the response to KA in RISE animals for raw gamma power (figure 3.2. Ai, 67.1 ± 26.1 μV^2, n = 7) and AUC (figure 3.2. Bi, 899.3 ± 450.6, n = 7) is increased compared to AMC despite being non-significant (25.4 ± 8.4 μV^2, n = 9, and 237.2 ± 91.3, n = 9, respectively).

Overall, these data reveal a loss of network excitability and responsiveness to KA in the hippocampus during the latent period that is most prevalent by week 5 post-induction. Like spontaneous gamma oscillations, there appears to be recovery in the ability to generate KA-induced gamma oscillations once epileptic animals reach the SRS stage of epileptogenesis. Combined with the above data on loss of spontaneous network excitability, there are demonstratable network changes occurring throughout the early stages of epileptogenesis appear to reduce excitability and which may reflect a compensatory mechanism driven by the seizures during induction.

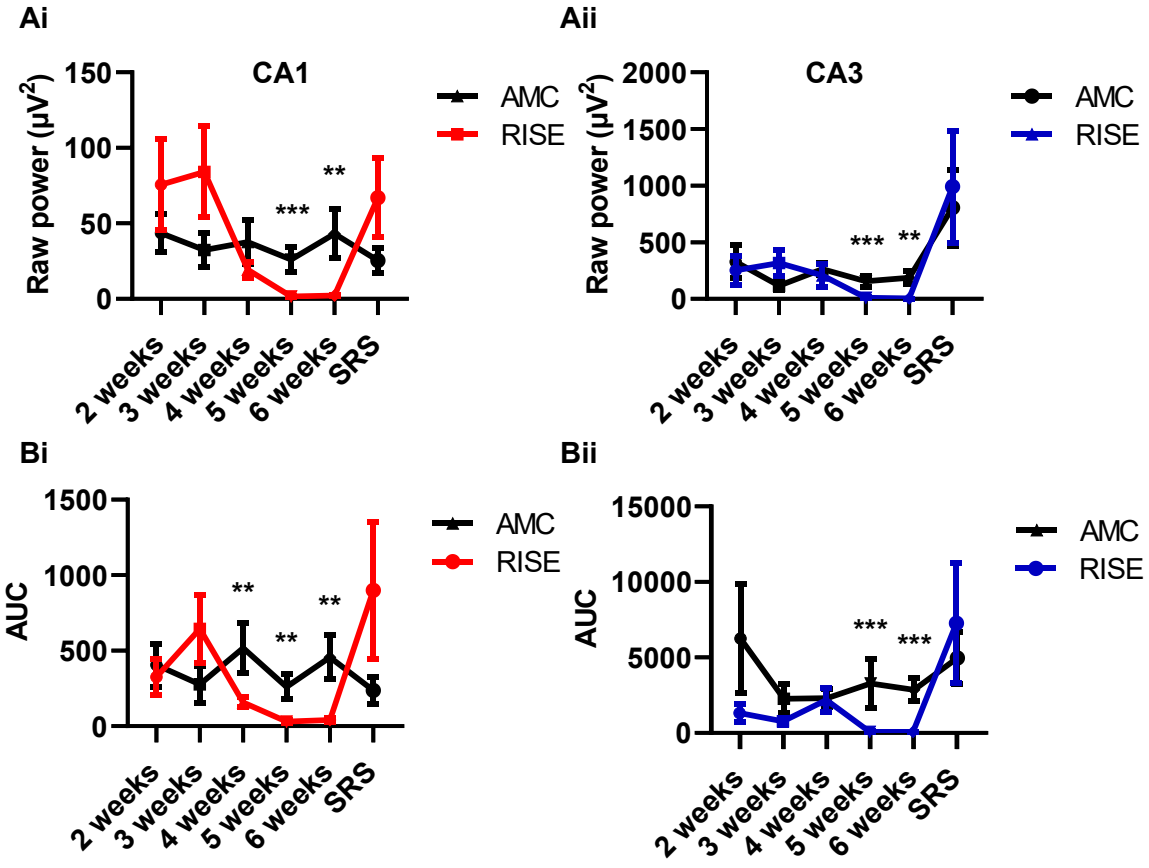

Figure 3.2. Comparison of kainic acid-induced network excitability in the hippocampus throughout epileptogenesis for AMC and RISE.

Connected column mean graphs of weeks 2, 3, 4, 5, 6 and SRS (>3 months) post-induction. (A) Graphs Ai and Aii show raw peak power (μV^2) for CA1 and CA3, respectively. (B) Graphs Bi and Bii show AUC analysis for CA1 and CA3, respectively. A manual band-pass of 15 – 49 Hz was used to isolate gamma oscillations. Red (left) represents CA1 and blue (right) represents CA3. Error bars show SEM. ** denotes $p \leq 0.01$ and *** denotes $p \leq 0.001$ (Mann-Whitney test).

Finally, for further confirmation of loss of KAR excitation in the hippocampus by weeks 5 and 6 of the latent period, figure 3.3. shows normalised percentage change of peak gamma power from spontaneous to KA. Consistently, weeks 2 – 4 are non-significant when compared with AMC in both CA1 (figure 3.3. A) and CA3 (figure 3.3. B), showing a robust increase in gamma power in response to the KA-challenge. By week 5, there is a 2597.0 ± 894.5% (figure 3.3. A, n = 6, $p \leq 0.05$) increase in CA1 in response to KAR activation in AMC, compared to 622.8 ± 168.7% in RISE (n = 9). A similar story emerges in CA3, with a 3462.0 ± 1625.0% (figure 3.3. B, n = 9, $p \leq 0.05$) increase in CA3 in response to KAR activation in AMC, compared to 737.0 ± 340.3% in RISE (n = 9). This deficit in response to KAR activation continues into week 6, with CA1 showing a 2073.0 ± 802.4% (n = 7, $p \leq 0.05$) increase in gamma power in AMC compared to 377.3 ± 72.9% (n = 7) in RISE. CA3 demonstrates a 1689.0 ± 483.1% (n = 11, $p \leq 0.05$) increase in gamma power in AMC, compared to 318.1 ± 67.0% (n = 8) in RISE. The KA-challenge gives us an indication of the amount of AMPAR/KAR excitation that could be produced in each slice, strongly suggesting there must be a significant loss of AMPAR and KAR in the RISE slices by week 5 post-induction and which blunts the gamma response.

As the data show, there is a subtle trend towards recovery in network excitability which becomes robust and significant in SRS and manifests as a large increase in spontaneous KAR excitation and KA-induced gamma oscillations. CA1 (figure 3.3. A) and CA3 (figure 3.3. B) both produce robust response to KAR activation, with CA1 producing a 2779.0 ± 815.4% (n = 9, p = ns) increase in gamma power in RISE compared to AMC (1575.0 ± 538.8%, n = 9). A similar story emerges in CA3, with RISE animals producing a 3852.0 ± 2576.0% (n = 8, p = ns) increase in gamma power compared to a 1407.0 ± 410.4% (n = 8) increase in AMC.

Overall, this demonstrates a loss of both spontaneously generated (figure 3.1.) and KA-induced (figure 3.2., 3.3.) gamma oscillations and network excitability in the hippocampus weeks 4 – 6 in RISE animals compared to AMC, with the most significant loss in network excitability being week 5 post-induction. Network excitability appears to recover to that of AMC once animals have reached the SRS stage, therefore showing there are continual network and receptor changes occurring throughout epileptogenesis which likely drives the progression of the disorder and eventual presentation of clinical seizures. In previous work (Needs et al., 2019) we shows a similar robust return of network excitation at the SRS stage, however, western blots from SRS hippocampi strongly indicated that GluA1 – 3 protein levels remained low, suggesting that recovery of network function is not simply due to upregulation of AMPAR subunit expression. This issue is further explored below.

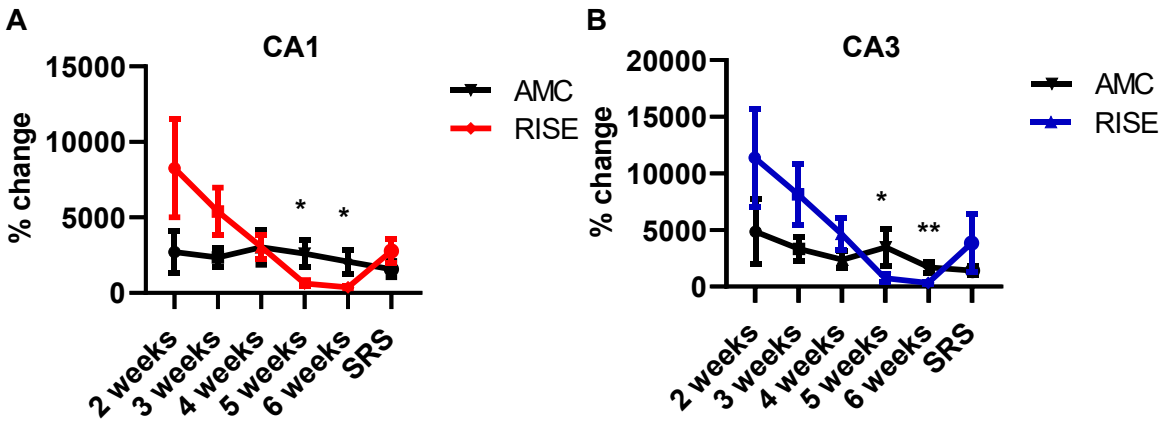

Figure 3.3. Normalised percentage change response to kainic acid in the hippocampus throughout epileptogenesis for AMC and RISE.

Connected column mean graphs of weeks 2, 3, 4, 5, 6 and SRS (>3 months) post-induction. (A) % change of gamma power from spontaneous to KA-induced oscillations for CA1. (B) % change of gamma power from spontaneous to KA-induced oscillations for CA3. A manual band-pass of 15 – 49 Hz was used to isolate gamma oscillations. Red (left) represents CA1 and blue (right) represents CA3. Error bars show SEM. * denotes $p \leq 0.05$ and ** denotes $p \leq 0.01$ (Mann-Whitney test).

3.2.3. Exploring the latent period of epileptogenesis - week 5 post-induction

The work above on spontaneous gamma oscillations (figure 3.1.) and KA-induced gamma oscillations (figures 3.2. and 3.3.) shows obvious and significant deficits in gamma oscillations by 5 weeks post-induction. The next section of this chapter will be delving more deeply into the local field changes which occur in week 5 post-induction in CA1 (figure 3.4.) and CA3 (figure 3.5.) of the hippocampus.

Figure 3.4. shows the response to the KA-challenge in AMC animals (figure 3.4 A) and RISE animals (figure 3.4. B) in CA1. In AMC, there is a clear increase in gamma power following bath application of 200nM KA. Figure 3.4. Ai shows an example FFT with its corresponding raw trace (figure 3.4. Aii). A highly synchronous gamma peak forms of ~30Hz following KAR activation. Peak raw gamma power saw an increase from 1.3 ± 0.4 μV^2 (figure 3.4. Aiii, n = 7) for spontaneous oscillations to 26.1 ± 8.4 μV^2 (n = 7, $p \leq 0.05$) following bath application of KA. There were however no significant differences in peak gamma frequency between spontaneous and KA (figure 3.4. Aiv, 29.4 ± 1.1 Hz for spontaneous and 32.4 ± 1.3 Hz for KA, p = ns).

In RISE animals 5 weeks post-induction, low power, incoherent oscillations emerge (figure 3.4. Bi, Bii) showing lower powered gamma oscillations both pre- and post-bath application of KA. However, this KA-induced gamma oscillation which is produced still oscillates at a similar

frequency to AMC, showing no deficits in the speed of the gamma oscillation produced. Peak raw gamma power saw an increase from 0.2 ± 0.04 μV^2 (figure 3.4. Biii, n = 10) for spontaneous oscillations to 1.6 ± 0.5 μV^2 (n = 10, $p \leq 0.01$) following bath application to KA. Despite peak gamma power being considerably smaller in comparison to AMC (figure 3.4. Aiii), bath application of KA caused a highly significant increase in gamma power in RISE. This is likely due to the persistent inability for CA1 to produce any robust spontaneous gamma oscillation at 5 weeks post-induction in RISE animals. As the baseline is so low, any increase would be very large due to the simple fact of dividing a larger number by a minuscule one. Meaning, any KAR activation following bath application with KA will cause a substantial increase in the overall oscillation. Like AMC, there is no significant difference in peak gamma frequency between spontaneous and KA in CA1 (figure 3.4. Biv, 29.9 ± 1.1 Hz for spontaneous and 29.9 ± 1.6 Hz for KA, p = ns).

Equally, figure 3.5. shows the response to the KA-challenge in AMC animals (figure 3.5. A) and RISE animals (figure 3.5. B) in CA3. In AMC, there is a huge increase in gamma power following bath application of 200nM KA. Figure 3.5. Ai shows an example FFT with its corresponding raw trace (figure 3.5. Aii). A highly synchronous gamma peak forms again ~30Hz following KAR activation. Peak raw gamma saw an increase from 12.7 ± 4.6 μV^2 (figure 3.5. Aiii, n = 8, $p \leq 0.01$) for spontaneous oscillations to 157.0 ± 48.2 μV^2 (n = 8, $p \leq 0.01$). There were no significant differences in peak gamma frequency between spontaneous and KA (figure 3.5. Aiv, 30.8 ± 1.2 Hz for spontaneous and 31.8 ± 1.1 Hz for KA, p = ns).

Conversely, in RISE animals 5 weeks post-induction, there is little evidence of coherent oscillations either pre- or post-bath application of KA (figure 3.5. Bi, Bii). Figure 3.5. Bi shows an example FFT with no defined gamma peak, showing defective network synchrony. However, like CA1, despite peak gamma being substantially smaller in comparison to AMC (figure 3.5. Aiii), bath application of KA caused a highly significant increase in gamma power in RISE. Again, this is likely due to the persistent inability for CA3 to produce any robust spontaneous gamma oscillation at 5 weeks post-induction. Bath application of KA caused an increase in gamma power from 0.6 ± 0.3 μV^2 (figure 3.5. Biii, n = 10) to 9.9 ± 4.2 μV^2 (n = 10, $p \leq 0.01$). Like AMC, there is no significant difference in peak gamma frequency between spontaneous and KA in CA3 (figure 3.5. Biv, 33.1 ± 2.1 Hz for spontaneous and 30.8 ± 1.0 Hz for KA, p = ns).

Taken together, this local field potential work on the different stages of epileptogenesis points to significant gamma power changes both in spontaneous conditions and in response to an excitatory network challenge with KA. This deficit is most prominent by week 5 of the latent period but appears to recover once RISE animals enter the SRS stage. The next section of this chapter looks to explore this recovery seen during the SRS stage of epileptogenesis.

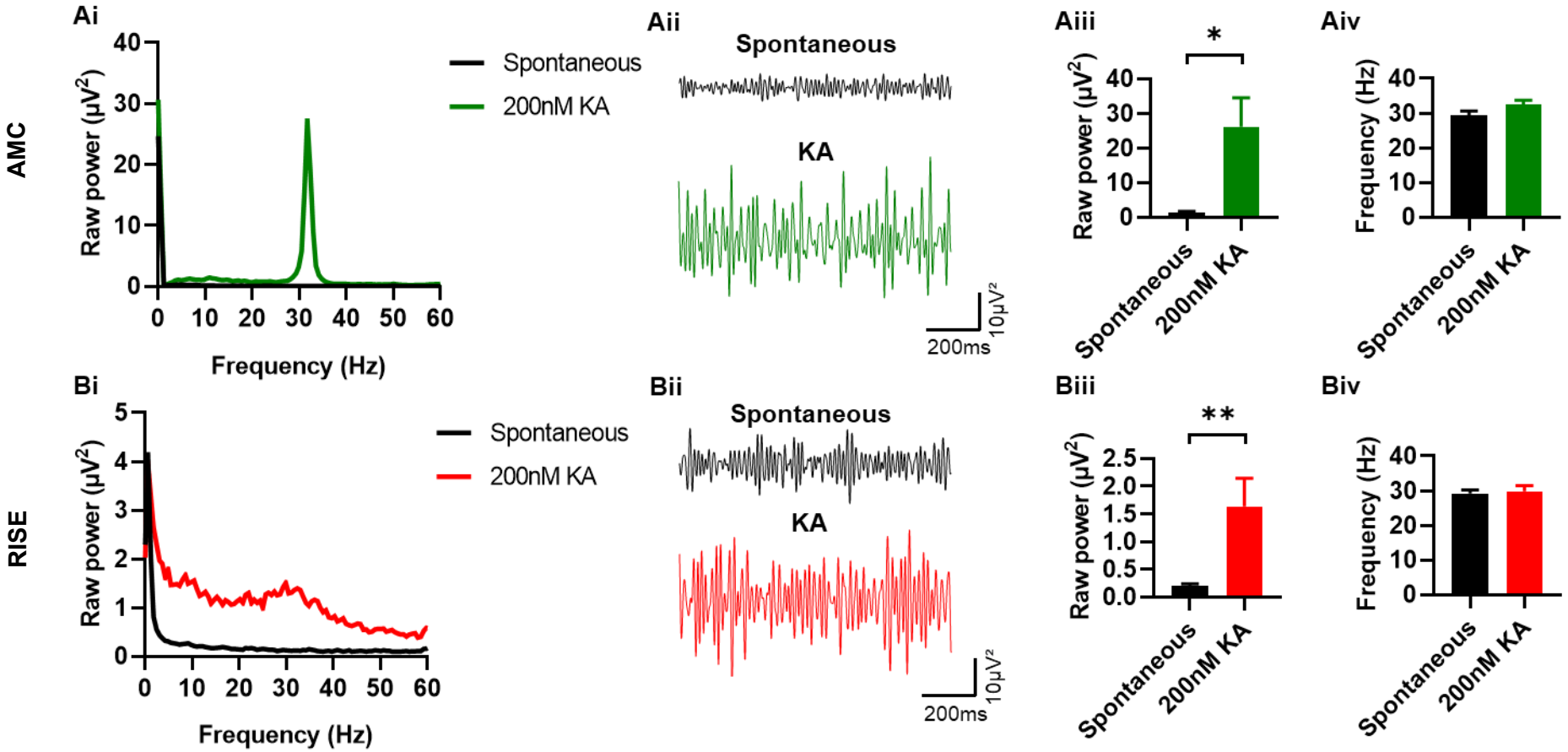

Figure 3.4. Exploring CA1 - week 5 post-induction of epileptogenesis.

(A) represents AMC and (B) represents RISE. (Ai) AMC example FFT showing spontaneous oscillations (black) and in the presence of 200nM KA (green). (Aii) one second raw trace from the same experiment (IIR filtered to a band-pass of 15 – 49 Hz). (Aiii) bar chart showing raw gamma power for both spontaneous and KA. (Aiv) bar chart showing peak gamma frequency for spontaneous and KA. (Bi) RISE example FFT showing spontaneous oscillations (black) and in the presence of 200nM KA (red). (Bii) one second raw trace from the same experiment (IIR filtered to a band-pass of 15 – 49 Hz). (Biii) bar chart showing raw gamma power for both spontaneous and KA. (Biv) bar chart showing peak gamma frequency for spontaneous and KA. Error bars show SEM. * denotes $p \leq 0.05$ and ** denotes $p \leq 0.01$ (Wilcoxon matched-pairs signed rank test).

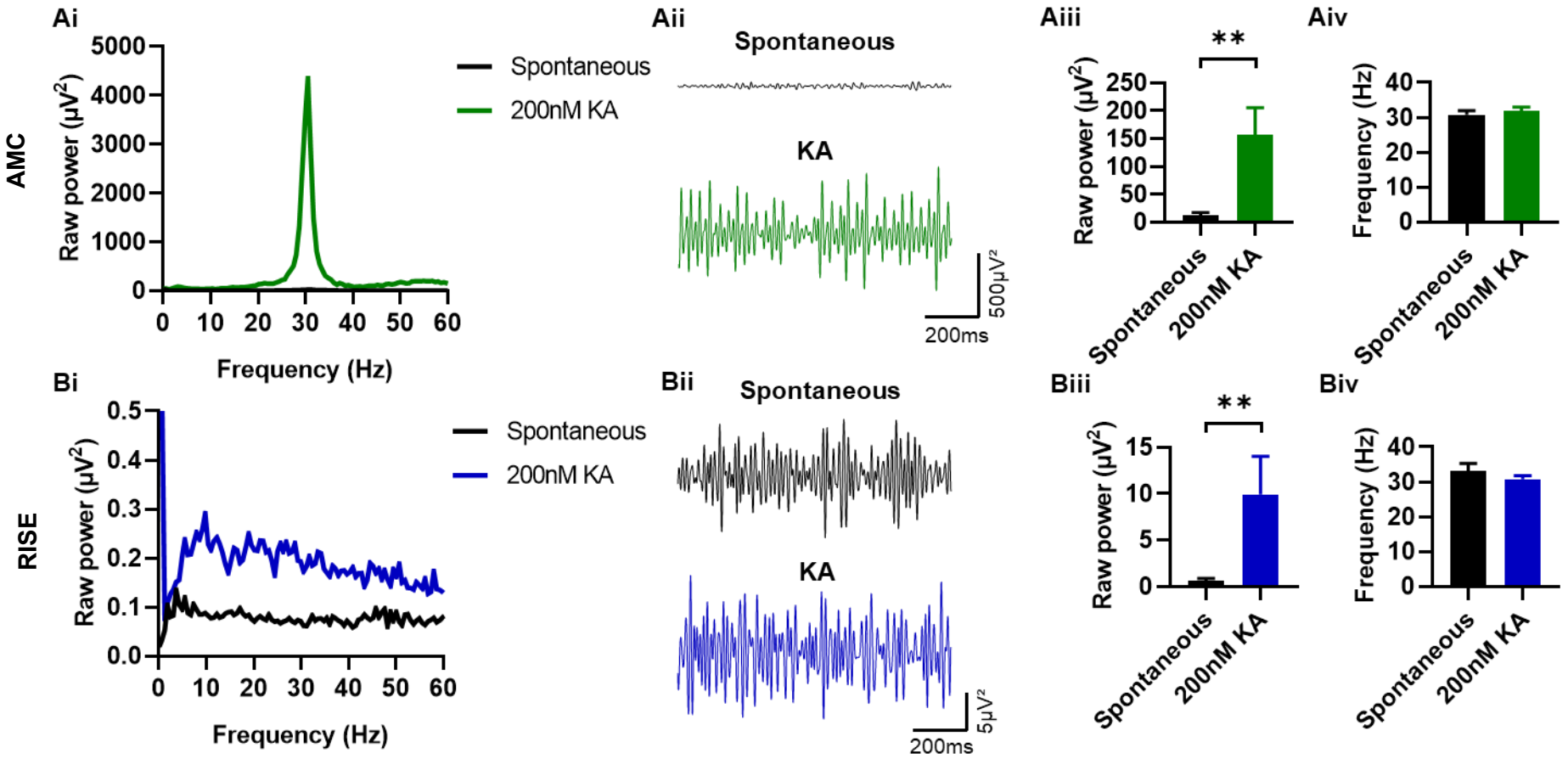

Figure 3.5. Exploring CA3 - week 5 post-induction of epileptogenesis.

(A) represents AMC and (B) represents RISE. (Ai) AMC example FFT showing spontaneous oscillations (black) and in the presence of 200nM KA (green). (Aii) one second raw trace from the same experiment (IIR filtered to a band-pass of 15 – 49 Hz). (Aiii) bar chart showing raw gamma power for both spontaneous and KA. (Aiv) bar chart showing peak gamma frequency for spontaneous and KA. (Bi) RISE example FFT showing spontaneous oscillations (black) and in the presence of 200nM KA (blue). (Bii) one second raw trace from the same experiment (IIR filtered to a band-pass of 15 – 49 Hz). (Biii) bar chart showing raw gamma power for both spontaneous and KA. (Biv) bar chart showing peak gamma frequency for spontaneous and KA. Error bars show SEM. ** denotes $p \leq 0.01$ (Wilcoxon matched-pairs signed rank test).

3.2.4. Network excitability and the transition from the latent period to SRS

Reduced network excitability during the latent period appears to be central to the progression of epileptogenesis. However, as previous work on the RISE model has shown, there is 'recovery' in network excitability once animals enter the SRS stage. Figure 3.6. looks to explore this further by comparing the peak raw gamma power of the latent period (week 6 post-induction) and the SRS stage for both spontaneous (figure 3.6. Ai and Aii) and KA-induced (figure 3.6. Bi and Bii) gamma oscillations in the hippocampus.

In spontaneous conditions, CA1 saw a peak raw gamma power of 0.7 ± 0.2 μV^2 (figure 3.6. Ai, n = 15) during the latent period which seemingly increased to 4.7 ± 2.2 μV^2 (n = 15, $p \leq 0.05$) once animals had transitioned into presentation of clinical seizures. CA3 showed a similar change, with spontaneous gamma oscillations producing a peak raw power of 2.7 ± 1.0 μV^2 (figure 3.6. Aii, n = 16) during the latent period which increased to 71.7 ± 22.9 μV^2 (n = 15, $p \leq 0.001$) once animals entered the SRS stage.

Similarly, in KA conditions, CA1 saw a peak raw gamma power of 2.2 ± 0.5 μV^2 (figure 3.6. Bi, n = 8) during the latent period which increased to 67.1 ± 26.1 μV^2 (n = 7, $p \leq 0.001$) once animals entered the SRS stage. Likewise, in CA3, KA-mediated gamma oscillations produced a peak raw power of 3.4 ± 1.3 μV^2 (figure 3.6. Bii, n = 8) during the latent period which increased substantially to 991.6 ± 496.0 μV^2 (n = 7, $p \leq 0.001$) once animals entered the SRS stage.

This demonstrates in both CA1 and CA3, there are substantial increases in both spontaneous and KA-induced network excitability once animals enter the SRS stage of epileptogenesis. This could be vital for our understanding of the progression of epileptogenesis and how an individual may transition from the seizure-free latent period into the presentation of clinical seizures. The rest of this chapter will focus on the synaptic changes occurring during epileptogenesis.

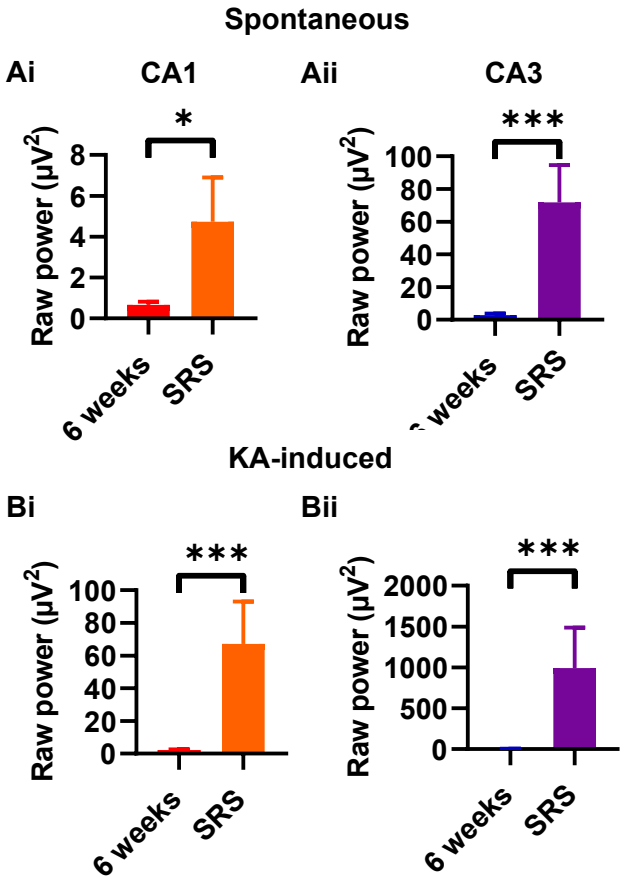

Figure 3.6. Comparison of network excitability during the latent period and SRS in spontaneous and KA conditions in RISE animals.

Bar graphs showing raw peak gamma power (μV^2) between the latent period (6 weeks post-induction) and the SRS stage of epileptogenesis. (Ai) raw gamma power of spontaneous gamma oscillations in CA1, (Aii) raw gamma power of spontaneous gamma oscillations in CA3, (Bi) raw gamma power of KA gamma oscillations in CA1, and (Bii) raw gamma power of KA gamma oscillations in CA3. A manual band-pass of 15 – 49 Hz was used to isolate gamma oscillations. Red/orange represents CA1, and blue/purple represents CA3. Error bars show SEM. * denotes $p \leq 0.05$ and *** denotes $p \leq 0.001$ (Mann-Whitney test).

3.2.5. Changes in synaptic excitability during epileptogenesis

The experiments described up to this point are entirely consistent with our previous work (Needs et al., 2019) showing that the collapse in network excitability in the latent period is accompanied by reduced expression of GluA1, GluA2 and GluA3 AMPAR subunits as measured by Western blotting. Up to this point, however, there was no functional evidence that synaptic AMPAR expression was altered. Voltage-clamp experiments were conducted to investigate the changes to sEPSCs in AMC and RISE across the progression of epileptogenesis in the hippocampus using the standard whole-cell patch method (chapters 2.2, 2.3.2). Like LFP experiments, timepoints during the latent period (weeks 2, 3, 4, 5 and 6 post-induction) and SRS (>3 months post-induction) were taken. Parameters studied to assess the effect of epileptogenesis on sEPSCs were amplitude (pA), decay time constant (tau, ms) and interevent interval (IEI, ms) (figure 3.7.). Due to the fragility of neurons in CA3 following

epileptogenesis, which is likely due to chronic inflammation, patch clamp recordings were only possible in the CA1 subregion of the hippocampus.

As can be seen in figure 3.7. A, the amplitude of sEPSCs trends towards decreasing amplitudes during the latent period of epileptogenesis but is only significantly different by week 6 post-induction. At week 6, the mean median amplitude of RISE sEPSCs was 8.3 ± 0.5 pA (n = 8), compared to 13.9 ± 2.3 pA (n = 4, $p \leq 0.05$) for AMC. Remarkably, there appears to be a significant increase in amplitude once RISE animals enter the SRS stage of epileptogenesis, with the RISE mean median amplitude being 16.4 ± 1.5 pA (n = 8) compared to 9.8 ± 1.4 pA (n = 5, $p \leq 0.05$) for AMC. This means there is a reduction of excitatory neurotransmission as the latent period progresses, with an increase in amplitude and excitatory neurotransmission seen once animals enter the SRS stage of epileptogenesis and are presenting with clinical seizures. This follows the trends seen in the LFP experiments (figures 3.1. – 3.6.).

sEPSC decay analysis of epileptogenesis (figure 3.7. B) found a trending increase in decay tau during the latent period of epileptogenesis that is only significant by week 5. At week 5, the mean median decay tau of sEPSCs is significantly slower in RISE animals (7.1 ± 1.1 ms, figure 3.6. B, n = 9) compared with AMC animals (3.6 ± 0.8 ms, n = 5, $p \leq 0.05$). This is also the case for 6 weeks post-induction, with the decay of sEPSCs in RISE animals being 9.7 ± 1.7 ms (n = 7) compared to 4.7 ± 0.9 ms (n = 5, $p \leq 0.05$) for AMC. This shows there is a change in sEPSC receptor kinetics as the latent period progresses.

Finally, there appears to be no significant difference between AMC and RISE in the IEI of sEPSCs across all timepoints of epileptogenesis (figure 3.7. C), meaning the frequency of sEPSCs are relatively stable throughout epileptogenesis.

Overall, this indicates there is a reduction in synaptic neurotransmission and excitability by week 6 of the latent period and an increase in excitatory neurotransmission once animals enter SRS, with a notable change in decay kinetics during the later stages of the latent period.

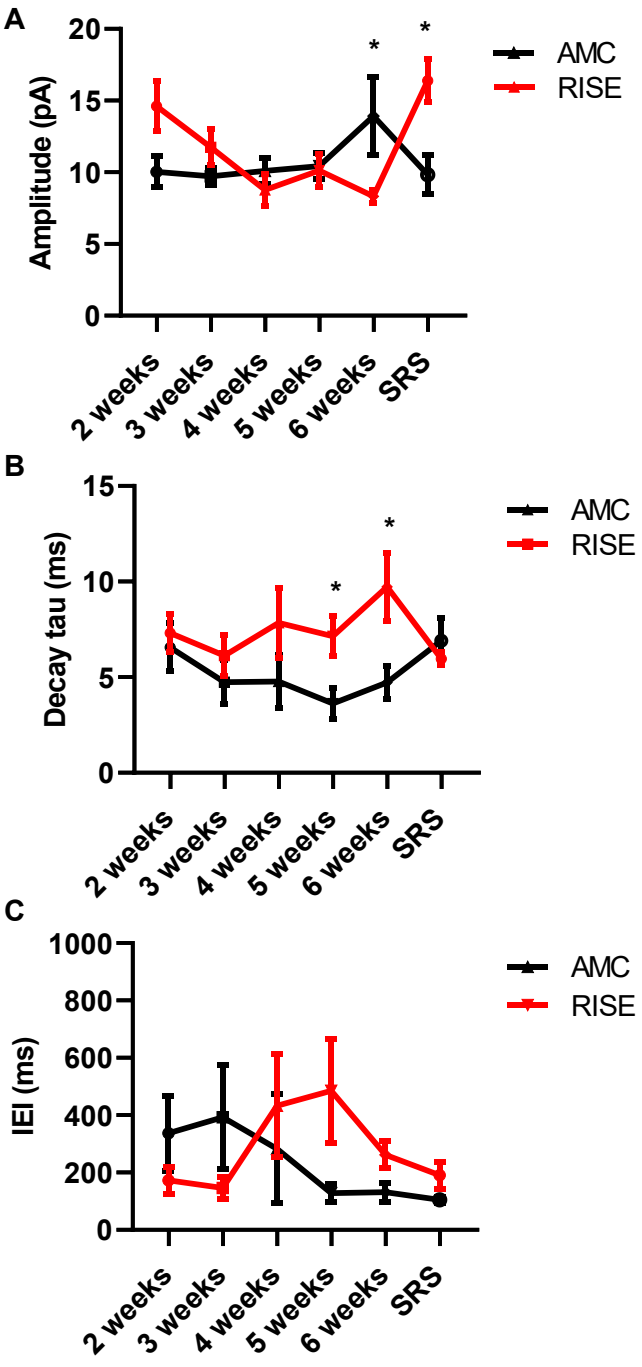

Figure 3.7. Changes in synaptic excitability during epileptogenesis.

Connected column mean graphs of sEPSC results for (A) mean median amplitude, (B) mean median decay tau, and (C) mean median IEI. Black lines indicate AMC and red lines indicate RISE. Error bars show SEM. * denotes $p \leq 0.05$ (Mann-Whitney test).

Figure 3.7. demonstrates how synaptic changes during epileptogenesis appear to arise significantly by week 6 post-induction. As such, figure 3.8. will be exploring this further, looking at week 6 post-induction (figure 3.8. A) and the SRS stage of epileptogenesis (figure 3.8. B).

During week 6 post-induction, there is a significant reduction in mean median amplitude of sEPSCs, reducing from 13.9 ± 2.7 pA (figure 3.8. Ai, n = 4) for AMC to 8.3 ± 0.5 pA (n = 8, $p \leq 0.05$). This is converse to the SRS stage of epileptogenesis, where there is an increase in amplitude of sEPSCs from 9.8 ± 1.4 pA (figure 3.8. Bi, n = 5) for AMC to 16.4 ± 1.5 pA (n = 8, $p \leq 0.05$). This reduction in sEPSC amplitude for week 6 post-induction is visible in the example raw trace (figure 3.7. Aiv), while the increase in sEPSC amplitude during SRS can be seen in figure 3.8. Biv. Meaning, there is a significant increase in the size of sEPSCs from week 6 post-induction to SRS.

There is also a significant increase in mean median decay of sEPSCs during week 6 post-induction. AMC shows a 4.8 ± 0.9 ms decay tau (figure 3.8. Aii, n = 5) compared to 9.7 ± 1.8 ms decay tau for RISE (n = 7, $p \leq 0.05$). There is however no significant different in sEPSC decay kinetics between AMC and RISE during the SRS stage of epileptogenesis (figure 3.8. Bii, AMC: 6.9 ± 1.2 ms, n = 5; RISE: 6.0 ± 0.3 ms, n = 10, p = ns). This shows there are changes in decay kinetics during week 6 of the latent period which recover once the animals enter the SRS stage of epileptogenesis and are presenting with clinical seizures.

Both week 6 and the SRS stage of epileptogenesis display increased but non-significant changes in the IEI of sEPSCs (figure 3.8. Aiii, Biii), meaning there is little change in the frequency of the sEPSCs.

Together, these data suggest there is a reduction in excitatory synaptic neurotransmission at 6 weeks post-induction which increases beyond AMC once animals enter the SRS stage of epileptogenesis. This fits with the above data exploring local field potential network dynamics in the hippocampus.

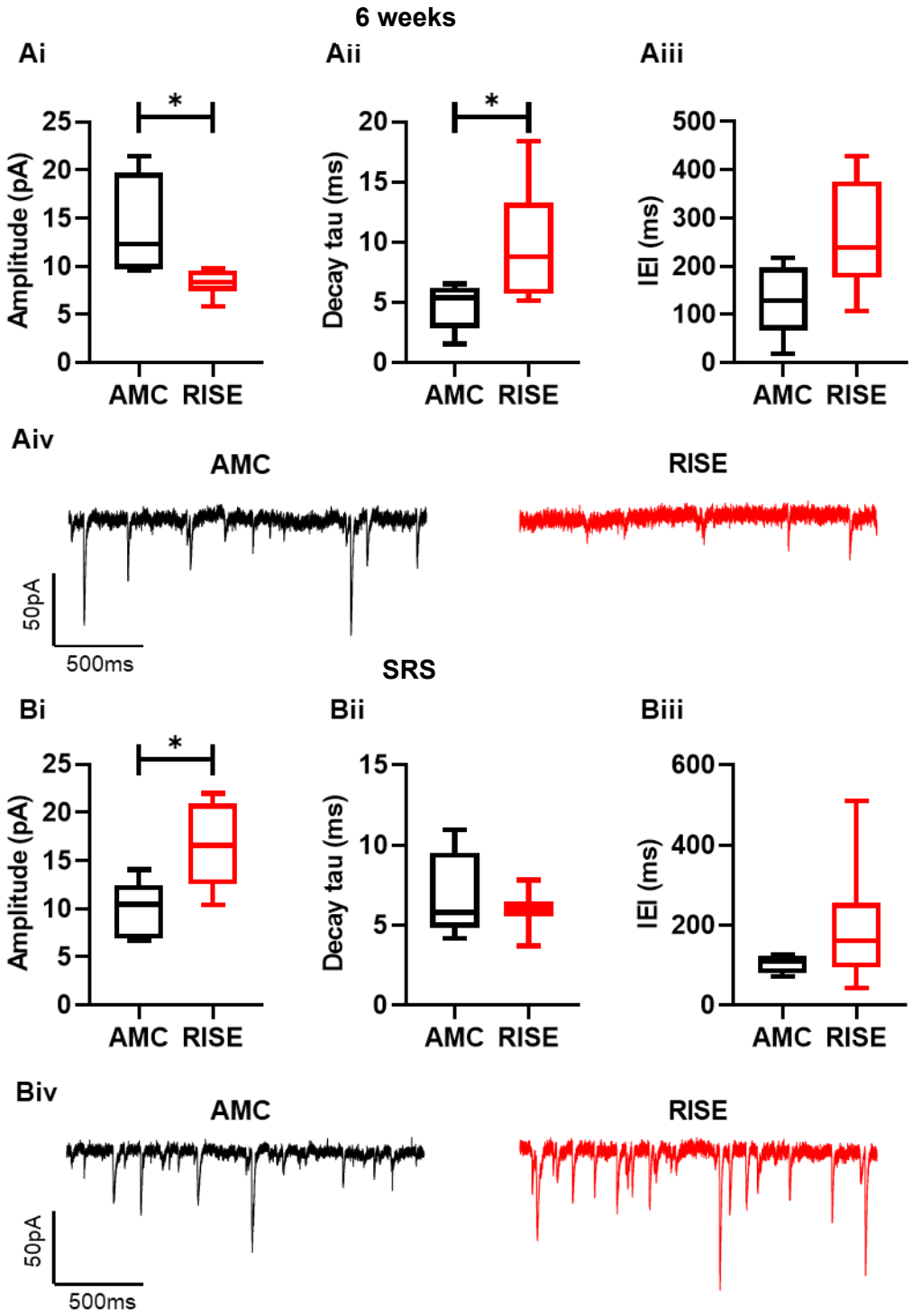

Figure 3.8. sEPSC changes during week 6 post-induction and the SRS stage of epileptogenesis.

(A) Week 6 post-induction, and (B) SRS stage. (Ai) Min to max graph showing mean median amplitude (pA) of sEPSCs during week 6 post-induction. (Aii) Min to max graph showing mean median decay tau (ms) during week 6 post-induction. (Aiii) Min to max graph showing mean median IEI (ms) during week 6 post-induction. (Aiv) Example raw trace of AMC (left, black) and RISE (right, red) at 6 weeks post-induction. (Bi) Min to max graph showing mean median amplitude (pA) of sEPSCs during SRS stage. (Aii) Min to max graph showing mean median decay tau (ms) during SRS stage. (Aiii) Min to max graph showing mean median IEI (ms) during SRS stage. Black lines indicate AMC and red lines indicate RISE. Error bars show SEM. * denotes $p \leq 0.05$ (Mann-Whitney test).

Further exploration of these synaptic changes which occur in RISE animals between the latent period (week 6 post-induction) and the SRS stage of epileptogenesis can be seen in figure 3.9. A substantial increase in hippocampal CA1 peak amplitude of sEPSCs is seen following the transition into SRS, with the latent period demonstrating a mean amplitude of 8.3 ± 0.5 pA (figure 3.9. A, n = 8) which increases to 14.5 ± 1.8 pA (n = 10, $p \leq 0.05$) as animals begin displaying clinical seizures. The decay tau demonstrates a significant decrease as epileptogenesis evolves, with animals in the latent period demonstrating a mean decay tau of 9.9 ± 1.7 ms (figure 3.9. B, n = 7) which decreases to 6.0 ± 0.3 ms (n = 10, $p \leq 0.05$) as animals begin displaying clinical seizures. However, there is no significant difference in the frequency of sEPSCs between the latent period and SRS stage of epileptogenesis (figure 3.9. C; 6 weeks: 211.0 ± 48.1 ms, n = 8; SRS: 174.5 ± 46.3 ms, n = 10; p = ns). Overall, this demonstrates that following the evolution of epileptogenesis into SRS, there are significant increases in peak amplitude and decreases in the decay of sEPSCs, with non-significant changes in the frequency of the excitatory events in the hippocampal CA1 subregion. This could be vital in advancing out understanding of how animals can transition from the seizure-free latent period into developing behavioural and electrographic seizures.

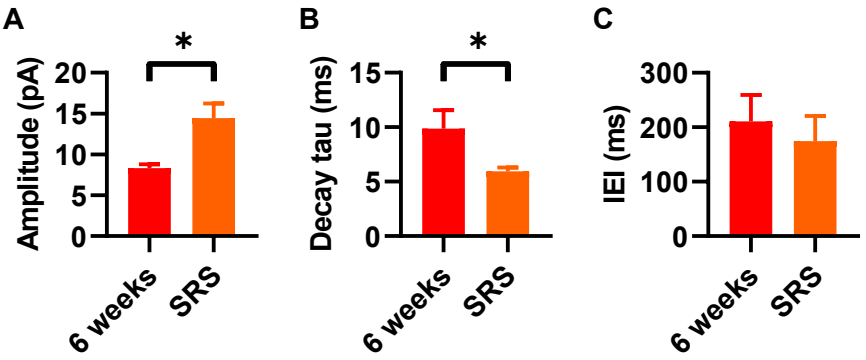

Figure 3.9. Comparison of sEPSCs between the latent period (6 weeks post-induction) and the SRS stage of epileptogenesis in RISE animals

Bar graphs showing mean amplitude (pA, A), mean decay tau (ms, B), and IEI (ms, C) for RISE animals during the latent period (6 weeks post-induction) and the SRS stage of epileptogenesis in the hippocampal CA1 subregion. Red represents the latent period and orange represents SRS. Error bars show SEM. * denotes $p \leq 0.05$ (Mann-Whitney test).

Finally, cumulative frequency graphs were produced (figure 3.10.) to highlight the change in sEPSC peak amplitude from 6 weeks post-induction (figure 3.10. A) to the SRS stage of epileptogenesis (figure 3.10. B). A clear shift from the left to the right is shown, meaning there is a considerable increase in the amplitude of sEPSC events once RISE animals enter SRS. This shift could be significant for the progression of epileptogenesis and the presentation of clinical seizures.

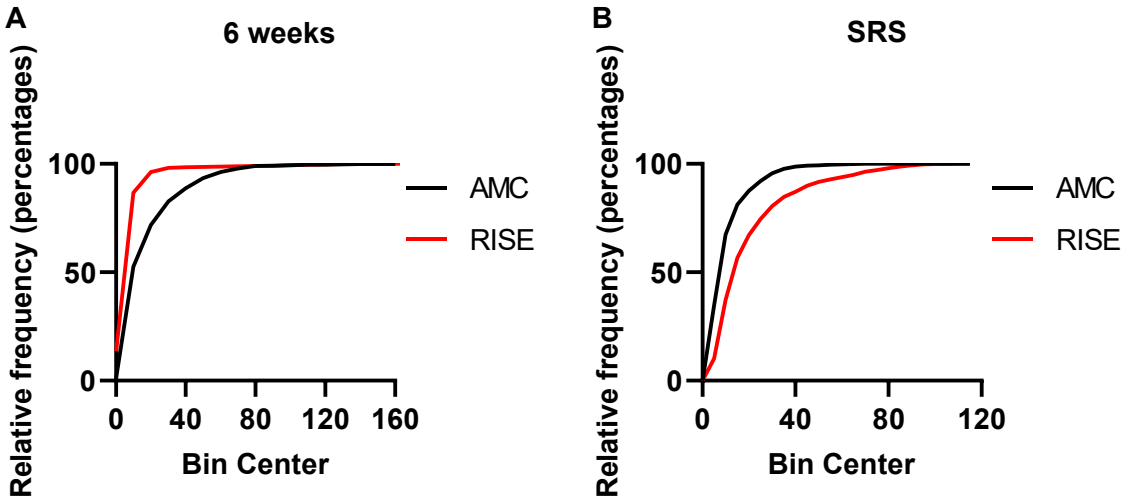

Figure 3.10. Cumulative frequency graphs of sEPSC amplitude during week 6 post-induction and the SRS stage of epileptogenesis.

Cumulative frequency graphs of sEPSC amplitude for 6 weeks post-induction (A) and SRS (B). Black lines indicate AMC and red lines indicate RISE.

Combined, the LFP and whole-cell voltage-clamp data shows there are significant network and cellular changes which occur during the latent period of epileptogenesis, particularly by weeks 5 – 6 post-induction. Overall, it appears there is a loss of network excitability in the hippocampus. Once animals enter the SRS stage of epileptogenesis, it appears there is recovery in some of these mechanisms, with some increasing beyond AMC. This shows two things – (1) there are continual cellular and network changes which are occurring, meaning epileptogenesis is a dynamic and evolving process, and (2) this increase in network and cellular excitability is likely associated with the clinical manifestation of seizures.

3.3. Discussion

This hypo-excitability in both spontaneous and KA-induced neurotransmission in the hippocampus during the latent period was noted in previous work studying the RISE model of epileptogenesis (Modebadze et al., 2016, Needs et al., 2019), with Needs *et al.* documenting

significant losses of certain AMPAR subunits (GluA1, GluA2 and GluA3) and the NMDAR subunit GluN2A. The above work fits with this idea of loss of vital glutamatergic neurotransmission, possibly AMPARs, leads to a loss of network excitability (figure 3.1. – figure 3.6.) and synaptic excitability (figure 3.7. – figure 3.9.).

Paradoxically, how could there be an increase in network excitability during SRS once animals present with clinical seizures if there is a persistent loss in excitatory neurotransmission, particularly AMPARs? The answer may lie in homeostatic plasticity. Homeostatic synaptic plasticity is the ability for neurons to stabilise their own excitability so that firing rates remain constant to prevent hyper- or hypo-excitability. A candidate mechanism for homeostatic plasticity (synaptic scaling and intrinsic excitability) involves the calcium/calmodulin-dependent protein kinase type IV (CaMKIV) which is Ca^{2+} sensitive. Increased neuronal activity and influx of Ca^{2+} leads to increased activity of CaMKIV, resulting in a homeostatic down-scale of excitatory synaptic strength and intrinsic excitability. Conversely, reduced neuronal activity and influx of Ca^{2+} leads to reduced activity of CaMKIV and the resulting up-scale of excitatory synaptic strength and intrinsic excitability. Activated CaMKIV regulates transcription via phosphorylation of cAMP responsive element binding protein (CREB), which alters trafficking and accumulation of synaptic AMPARs to scale the synaptic strength and intrinsic excitability of neurons to its target firing rate (Joseph and Turrigiano, 2017, Turrigiano, 2008).

As such, when activity decreases (like in the loss of AMPARs) excitation between pyramidal cells in the hippocampus is boosted and feedback inhibition is reduced, therefore increasing pyramidal cell firing rates. This aims to maintain the excitatory-inhibitory balance (Turrigiano and Nelson, 2004). Although non-significant, figure 3.7. C shows a trending increase in IEI as the latent period progresses into weeks 4 and 5, meaning there is a decrease in firing rates. This appears to recover to AMC once RISE animals reach the SRS stage, possibly showing a homeostatic regulation in intrinsic excitability of pyramidal cells in the hippocampus despite persistent loss of AMPAR neurotransmission.

A study examining the KA rodent model of epileptogenesis also found parallel reductions in the AMPAR subunits GluA1 and GluA2 when studying the chronic process of TLE (Egbenya et al., 2018), again pointing to hypo-excitability driving epileptogenesis. But how could this loss of excitation lead to the development of seizures? This could be explained by studying the autoimmune condition anti-AMPAR encephalitis. Auto-antibodies generated against AMPARs lead to internalisation of the receptor complex and temporal lobe seizures. There is a reduction in excitatory currents in hippocampal pyramidal cells, and a corresponding ‘homeostatic’ decrease in inhibitory currents with overall increased intrinsic excitability. Peng *et al.* hypothesises that pyramidal cells will maintain a constant firing rate even in response to chronic inactivity, which may mean firing at a higher intrinsic rate while receiving less synaptic input, therefore leading to the generation of epileptic activity (Dalmau et al., 2017, Day et al., 2023, Haselmann et al., 2018, Peng et al., 2015).

Finally, given the consistent frequency of the gamma oscillations, it is possible that all neuron types, particularly GABAergic inhibitory interneurons, are still present in the hippocampus. Evidence for this comes from the non-significant changes in peak gamma frequency in the hippocampus for CA1 (figure 3.4. Biv) and CA3 (figure 3.5. Biv) both in spontaneous and KA-induced conditions. The role inhibitory interneurons play in the generation of gamma oscillations is well established (Buzsáki and Wang, 2012), meaning there is no significant loss of inhibitory interneurons at this stage and that the loss of network and cellular excitability is likely due to a loss of excitatory, glutamatergic receptors.

Overall, it is clear there are significant losses in hippocampal excitability during the latent period of epileptogenesis, which are most prevalent by weeks 5 – 6 post-induction. The network and synaptic activity appears to recover coincidentally with the appearance of SRS, but the intrinsic mechanisms for the generation of epileptic activity are still to be elucidated. In conjunction with previous research studying TLE using the RISE model, it is hypothesised that a specific loss of AMPARs drives this hypo-excitability and eventual progression to clinical seizures. An avenue for future research studying epileptogenesis using the RISE model could be to record miniature EPSCs (mEPSCs). In the presence of tetrodotoxin, neurons are unable to generate action potentials. However, presynaptic release of neurotransmitter vesicles is probabilistic and will therefore occasionally be released into the synapse, leading to activation of postsynaptic receptors and the generation of a mEPSC. Recording of mEPSCs would allow for analysis of synaptic scaling of AMPARs during epileptogenesis. Chronic down-scaling of AMPARs leads to a paradoxical increase in mEPSC amplitude and prolonged AMPAR half-life, consequently modulating the size of the mEPSC and reducing receptor turnover (O'Brien et al., 1998).

Chapter 4 Local field and synaptic effects of tianeptine *in vitro*

4.1. Introduction

Chapter 3 demonstrates how the latent period of epileptogenesis has significant reductions in network and synaptic excitability. Given previous research using the RISE model, this is hypothesised to be caused by a reduction in AMPAR neurotransmission. However, network excitability appears to recover to control values as the networks progress towards spontaneous recurrent seizures. But what if it were possible to alter the progression into clinical seizures, using the changes in latent period as a disease target? One potential approach would be to try and restore AMPAR excitation during the latent period and hence to subvert the process of epileptogenesis that is driven by network quiescence.

The atypical tricyclic antidepressant tianeptine (7-[(3-chloro-6-methyl-5,5-dioxo-11*H*-benzo[c][2,1]benzothiazepin-11-yl)amino]heptanoate), also known as Stablon, is used as a treatment for major depressive disorder and anxiety.

Chronic administration of tianeptine has been found to increase GluA1 phosphorylation in both the frontal cortex and hippocampus, with a more pronounced effect in the CA3 subregion of the hippocampus than in CA1. Tianeptine also reduced stress-induced dendritic atrophy and modulates excitatory synaptic neurotransmission in CA3 of chronically stress rats (Kole et al., 2002, Magariños et al., 1999, Svenningsson et al., 2007).

Phosphorylation of two sites (Ser831 and Ser845) on the GluA1 subunit of postsynaptic AMPARs is thought to affect the functional properties of AMPARs. Phosphorylation of the Ser831 residue on GluA1 by calcium/calmodulin-dependent protein kinase II/protein kinase C (CaMKII/PKC) results in increased channel conductance (Derkach et al., 1999, Jenkins and Traynelis, 2012). Conversely, phosphorylation of the Ser845 residue on GluA1 by protein kinase A (PKA) results in altered AMPAR trafficking by increasing GluA1-containing AMPAR localisation in the postsynaptic membrane and decreasing AMPAR internalisation (Lee et al., 2000, Liu et al., 2009, Man et al., 2007). Overall, phosphorylation of these two sites results in increased AMPAR neurotransmission and this may underlie tianeptine's antidepressant properties.

Unlike typical antidepressants, such as selective serotonin re-uptake inhibitors (SSRIs), tianeptine does not bind to adrenergic, dopaminergic or serotonergic receptors or transporters (Kato and Weitsch, 1988). Instead, tianeptine is thought to potentiate AMPARs by activation CaMKII and PKA via various signalling cascades associated with synaptic plasticity (the p38, p42/44 mitogen-activated protein kinase (MAPK) and the c-Jun N-terminal kinase (JNK) pathway), and decreased surface diffusion of AMPARs by activation of CaMKII which leads to phosphorylation of AMPAR auxiliary subunit stargazin, with the resulting AMPAR-stargazin interaction forming a complex with PDZ scaffold proteins such as postsynaptic density 95 (PSD-95). This leads to immobilisation and anchoring of AMPARs in the postsynaptic

membrane, meaning tianeptine increases both AMPAR channel conductance, and trafficking and stabilisation in the postsynaptic membrane (Szegedi et al., 2011, Zhang et al., 2013).

As such, given our current understanding of epileptogenesis using the RISE model of TLE, tianeptine was identified as a drug with therapeutic potential for altering the progression of epileptogenesis by increasing AMPAR conductance and synaptic localisation, with hope of stopping/slowing progression into clinical seizures. This results chapter aims to characterise the *in vitro* LFP and sEPSC effects of acute tianeptine on hippocampal pyramidal cells using the same timepoints as studied for epileptogenesis in chapter 3 (AMC weeks 2 – 6, p35 – 63 and >3 months, >p90), and the chronic response to tianeptine *in vitro*.

4.2. Results

4.2.1. Effect of acute tianeptine on spontaneous local field hippocampal gamma oscillations

In advance of any experiments to explore the use of tianeptine as a disease-modifying drug during epileptogenesis, we decided firstly to characterise its basic effects on neuronal network function. Horizontal hippocampal-entorhinal slices were prepared from AMC Wistar rats at the timepoints mentioned above using the standard LFP method (chapter 2.5). To investigate the effects of acute 10μM tianeptine on hippocampal gamma oscillations, both spontaneous and KA-induced gamma oscillations in both CA1 and CA3 were assessed. 10μM tianeptine was used as previous research has shown this concentration enhances the GluA1-dependent initial phase of LTP (Szegedi et al., 2011). Peak raw power analysis was used to examine the effect of tianeptine on spontaneous LFP gamma. A band-pass of 15 – 49 Hz was used to isolate gamma frequencies.

Following stabilisation of spontaneous gamma band activity for at least 30 minutes, 10μM tianeptine was added for a further 30 minutes minimum. As can be seen in figure 4.1., acute bath application of 10μM tianeptine onto spontaneous gamma oscillations in CA1 produces a robust increase in raw gamma power across all AMC timepoints studied. At 2 weeks AMC, there is an increase from 2.2 ± 1.3 μV^2 for spontaneous gamma oscillations (figure 4.1. A, n = 8) to 3.4 ± 1.4 μV^2 following acute application of tianeptine (n = 8, $p \leq 0.01$). At 3 weeks AMC, there is an increase from 4.0 ± 1.8 μV^2 for spontaneous gamma oscillations (figure 4.1. B, n = 9) to 17.1 ± 6.0 μV^2 following acute application of tianeptine (n = 9, $p \leq 0.01$). At 4 weeks AMC, there is an increase from 10.8 ± 4.8 μV^2 for spontaneous gamma oscillations (figure 4.1. C, n = 8) to 25.1 ± 8.0 μV^2 following acute application of tianeptine (n = 8, $p \leq 0.01$). At 5 weeks AMC, there is an increase from 10.6 ± 7.9 μV^2 for spontaneous gamma oscillations (figure 4.1. D, n = 8) to 51.4 ± 32.0 μV^2 following acute application of tianeptine (n = 8, $p \leq 0.01$). At 6 weeks AMC, there is an increase from 5.7 ± 2.8 μV^2 for spontaneous gamma oscillations (figure 4.1. E, n = 10) to 21.4 ± 10.5 μV^2 following acute application of tianeptine (n = 10, $p \leq$

0.01). And finally, at the latest timepoint for AMC ('late AMC' – equivalent to the age at appearance of SRS), there is an increase from 1.8 ± 0.4 μV^2 for spontaneous gamma oscillations (figure 4.1. F, n = 9) to 6.2 ± 1.5 μV^2 following acute application of tianeptine (n = 9, $p \leq 0.01$). The largest increase in spontaneous gamma oscillations in CA1 was week 5 AMC (figure 4.1. D), which saw a 484.9% increase in hippocampal power following application of tianeptine.

A similar story emerges with CA3. Figure 4.2. shows acute bath application of 10μM tianeptine onto spontaneous gamma oscillations in CA3. At 2 weeks AMC, there is an increase from 27.7 ± 17.0 μV^2 for spontaneous gamma oscillations (figure 4.2. A, n = 9) to 56.3 ± 39.4 μV^2 following acute application of tianeptine (n = 9, $p \leq 0.01$). At 3 weeks AMC, there is an increase from 50.1 ± 24.2 μV^2 for spontaneous gamma oscillations (figure 4.2. B, n = 9) to 164.3 ± 51.5 μV^2 following acute application of tianeptine (n = 9, $p \leq 0.01$). At 4 weeks AMC, there is an increase from 120.3 ± 31.6 μV^2 for spontaneous gamma oscillations (figure 4.2. C, n = 7) to 744.6 ± 301.8 μV^2 following acute application of tianeptine (n = 7, $p \leq 0.05$). At 5 weeks AMC, there is an increase from 57.6 ± 16.3 μV^2 for spontaneous gamma oscillations (figure 4.2. D, n = 8) to 276.6 ± 123.5 μV^2 following acute application of tianeptine (n = 8, $p \leq 0.01$). At 6 weeks AMC, there is an increase from 182.6 ± 78.2 μV^2 for spontaneous gamma oscillations (figure 4.2. E, n = 7) to 505.4 ± 263.1 μV^2 following acute application of tianeptine (n = 7, $p \leq 0.05$). And finally, at late AMC, there is an increase from 59.9 ± 38.1 μV^2 for spontaneous gamma oscillations (figure 4.2. F, n = 10) to 180.2 ± 121.9 μV^2 following acute application of tianeptine (n = 10, $p \leq 0.01$). The largest increase in spontaneous gamma oscillations in CA3 was week 4 AMC (figure 4.2. C), which saw a 619.0% increase in hippocampal power following application of tianeptine.

Overall, figures 4.1. and 4.2. demonstrate the ability for tianeptine to increase the gamma power of spontaneous gamma oscillations across all timepoints studied in both CA1 and CA3, respectively.

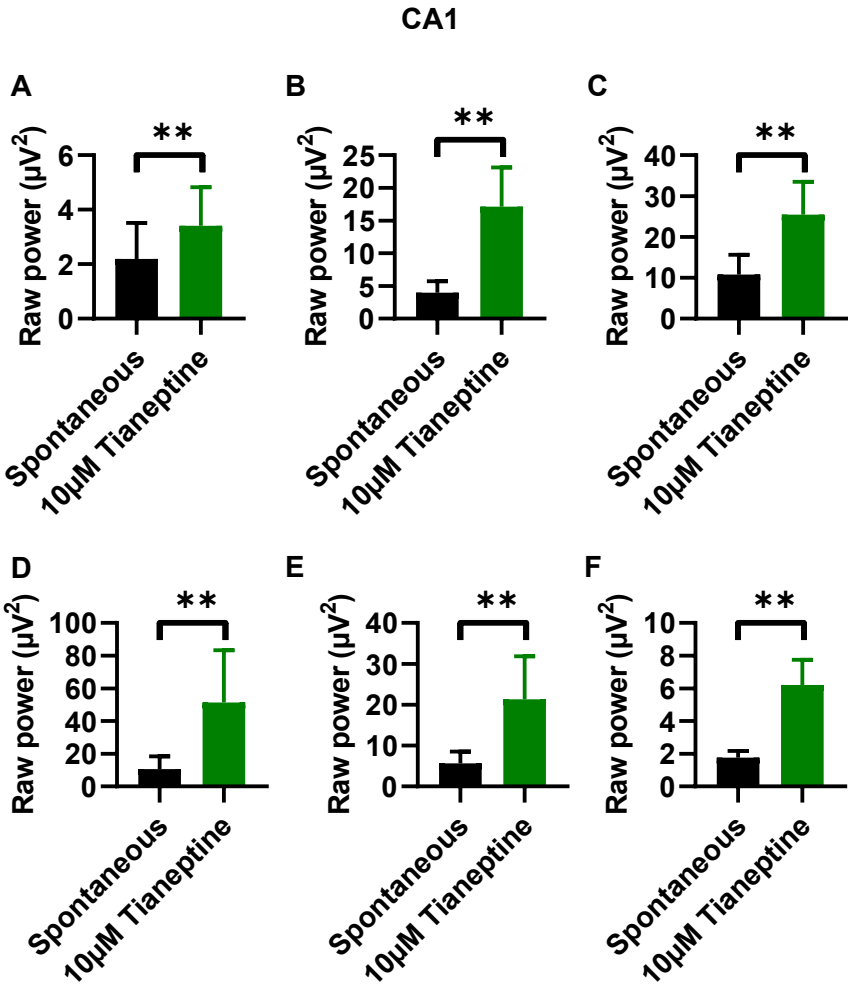

Figure 4.1. Effect of tianeptine on spontaneous gamma oscillations in CA1.

Bar charts showing raw gamma power (μV^2) in spontaneous conditions (black) and following bath application of 10μM tianeptine (green). (A) 2 weeks AMC, (B) 3 weeks AMC, (C) 4 weeks AMC, (D) 5 weeks AMC, (E) 6 weeks AMC, and (F) late AMC. Error bars show SEM. ** denotes $p \leq 0.01$ (Wilcoxon matched-paired signed rank test).

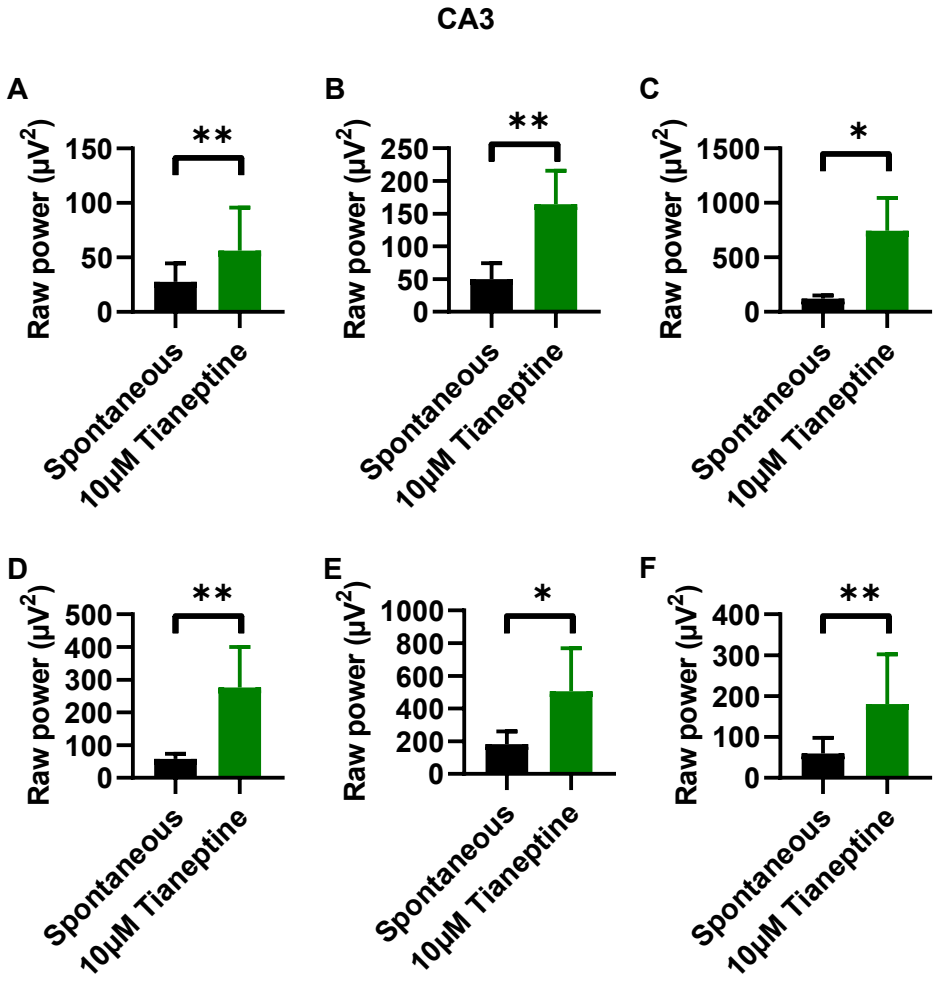

Figure 4.2. Effect of tianeptine on spontaneous gamma oscillations in CA3.

Bar charts showing raw gamma power (μV^2) in spontaneous conditions (black) and following bath application of 10μM tianeptine (green). (A) 2 weeks AMC, (B) 3 weeks AMC, (C) 4 weeks AMC, (D) 5 weeks AMC, (E) 6 weeks AMC, and (F) late AMC. Error bars show SEM. * denotes $p \leq 0.05$, and ** denotes $p \leq 0.01$ (Wilcoxon matched-paired signed rank test).

4.2.2. Effect of acute tianeptine on KA-induced local field hippocampal gamma oscillations

Since AMPAR trafficking in and out of the synapse is activity-dependent (Henley and Wilkinson, 2013), it is important to test the effects of tianeptine in conditions where AMPARs will be activated during a high degree of synaptic drive. We next tested the effect of acute tianeptine on hippocampal gamma oscillations that were generated with 200nM KA in both CA1 (figure 4.3.) and CA3 (figure 4.4.) across the same timepoints as above (AMC weeks 2 – 6 and >3 months).

Following stabilisation of spontaneous gamma band activity for at least 30 minutes, 200nM KA was added for a further 30 minutes minimum. Once stabilisation in KA was achieved, 10μM tianeptine was also added for 30 minutes. As can be seen in figure 4.3., 10μM tianeptine effectively potentiated KA-induced gamma oscillations in CA1 at all timepoints investigated (figure 4.3. A – F). At 2 weeks AMC, there is an increase from 88.4 ± 46.4 μV^2 for KA gamma oscillations (figure 4.3. A, n = 13) to 234.3 ± 129.7 μV^2 following acute application of tianeptine (n = 13, $p \leq 0.001$). At 3 weeks AMC, there is an increase from 28.5 ± 10.4 μV^2 for KA gamma oscillations (figure 4.3. B, n = 8) to 153.3 ± 101.7 μV^2 following acute application of tianeptine (n = 8, $p \leq 0.01$). At 4 weeks AMC, there is an increase from 37.7 ± 14.4 μV^2 for KA gamma oscillations (figure 4.3. C, n = 7) to 155.4 ± 62.9 μV^2 following acute application of tianeptine (n = 7, $p \leq 0.05$). At 5 weeks AMC, there is an increase from 209.6 ± 158.7 μV^2 for KA gamma oscillations (figure 4.3. D, n = 9) to 367.7 ± 255.9 μV^2 following acute application of tianeptine (n = 9, $p \leq 0.01$). At 6 weeks AMC, there is an increase from 43.2 ± 16.2 μV^2 for KA gamma oscillations (figure 4.3. E, n = 8) to 135.9 ± 50.2 μV^2 following acute application of tianeptine (n = 8, $p \leq 0.01$). At late AMC, there is an increase from 25.4 ± 8.4 μV^2 for KA gamma oscillations (figure 4.3. F, n = 9) to 143.8 ± 57.6 μV^2 following acute application of tianeptine (n = 9, $p \leq 0.01$). the largest increase in KA-induced gamma oscillations in CA1 was late AMC (figure 4.3. F), which saw a 566.1% increase in hippocampal power following application of tianeptine.

A similar story emerges with CA3. At 2 weeks AMC, there is an increase from 1520.0 ± 626.7 μV^2 for KA gamma oscillations (figure 4.4. A, n = 16) to 4060.0 ± 1495.0 μV^2 following acute application of tianeptine (n = 16, $p \leq 0.001$). At 3 weeks AMC, there is an increase from 2242.0 ± 1328.0 μV^2 for KA gamma oscillations (figure 4.4. B, n = 11) to 5209.0 ± 2950.0 μV^2 following acute application of tianeptine (n = 11, $p \leq 0.001$). At 4 weeks AMC, there is an increase from 237.5 ± 51.6 μV^2 for KA gamma oscillations (figure 4.4. C, n = 9) to 934.7 ± 298.5 μV^2 following acute application of tianeptine (n = 9, $p \leq 0.01$). At 5 weeks AMC, there is an increase from 2654.0 ± 1898.0 μV^2 for KA gamma oscillations (figure 4.4. D, n = 11) to 4526.0 ± 3002.0 μV^2 following acute application of tianeptine (n = 11, $p \leq 0.001$). At 6 weeks AMC, there is an increase from 478.7 ± 207.1 μV^2 for KA gamma oscillations (figure 4.4. E, n = 11) to 902.1 ± 287.2 μV^2 following acute application of tianeptine (n = 11, $p \leq 0.001$). And finally, at late AMC,

there is an increase from 805.3 ± 336.1 μV^2 for KA gamma oscillations (figure 4.4. F, n = 8) to 2310.0 ± 1106.0 μV^2 following acute application of tianeptine (n = 9, $p \leq 0.01$). The largest increase in KA-induced gammas oscillations in CA3 was 4 weeks AMC (figure 4.3. C), which saw a 393.6% increase in hippocampal power following application of tianeptine.

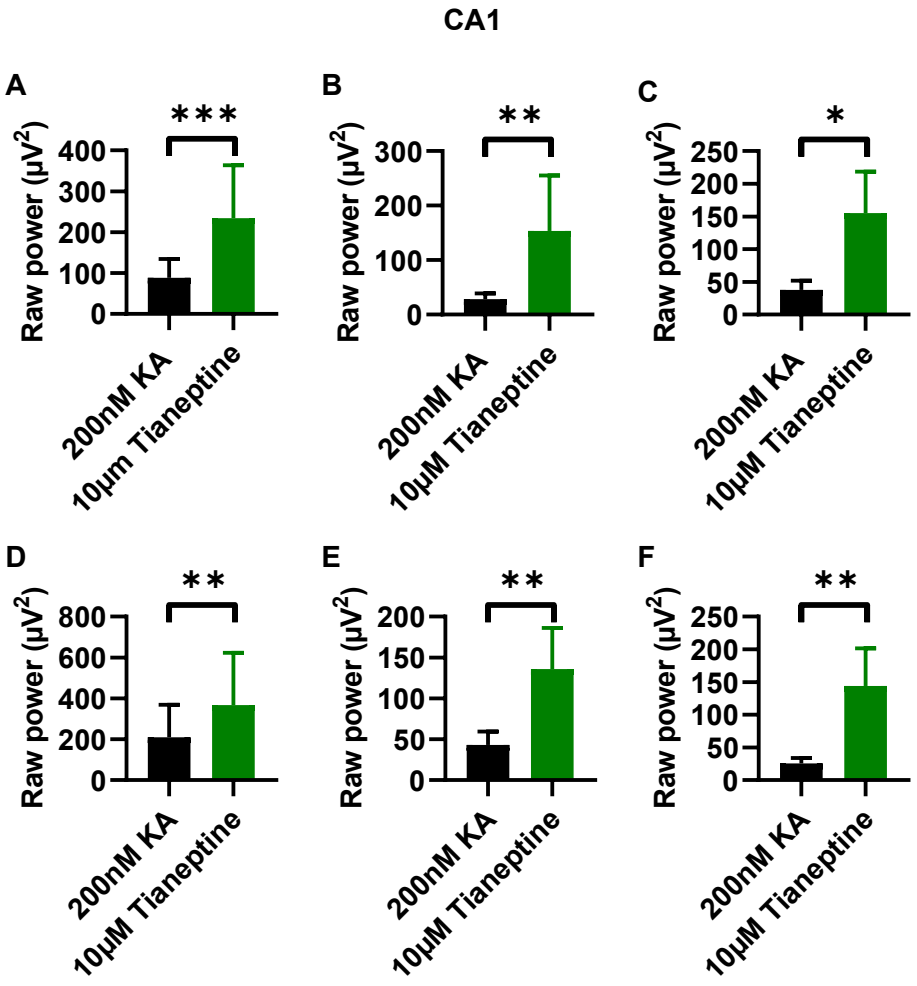

Figure 4.3. Effect of tianeptine on KA-induced gamma oscillations in CA1.

Bar charts showing raw gamma power (μV^2) in KA conditions (black) and following bath application of 10μM tianeptine (green). (A) 2 weeks AMC, (B) 3 weeks AMC, (C) 4 weeks AMC, (D) 5 weeks AMC, (E) 6 weeks AMC, and (F) late AMC. Error bars show SEM. * denotes $p \leq 0.05$, ** denotes $p \leq 0.01$, and *** denotes $p \leq 0.001$ (Wilcoxon matched-paired signed rank test).

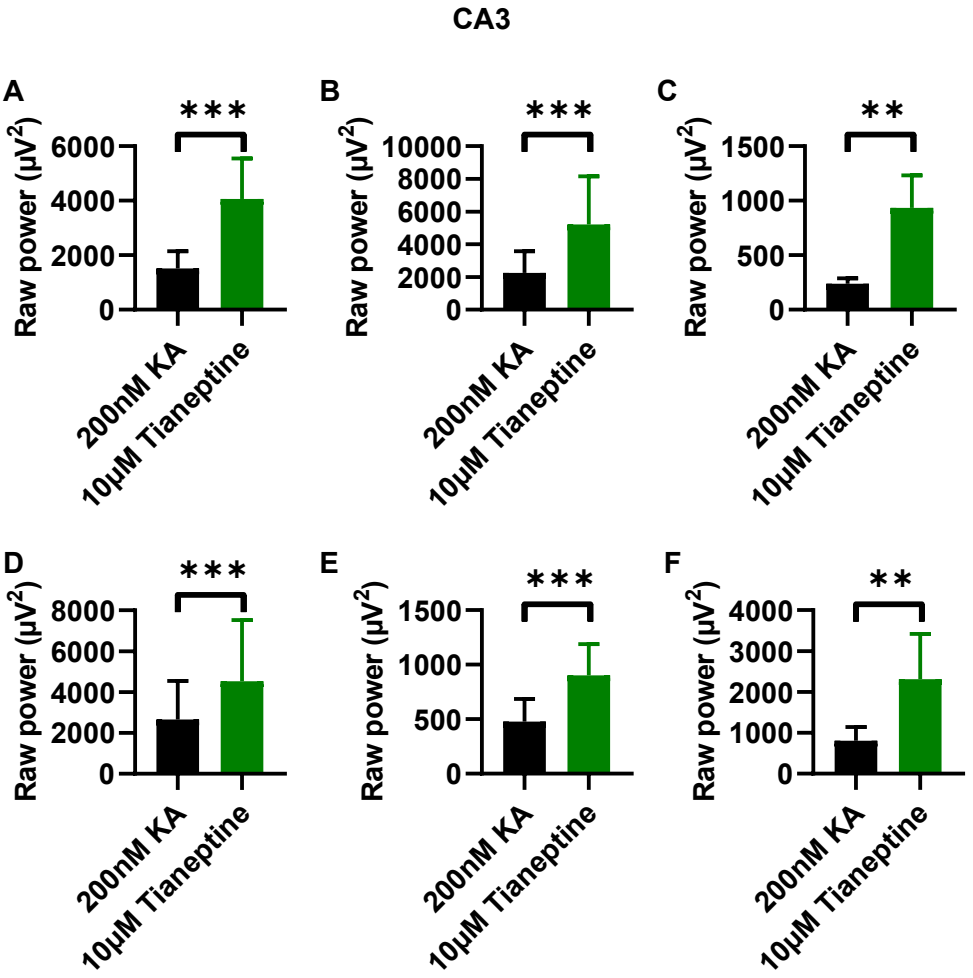

Figure 4.4. Effect of tianeptine on KA-induced gamma oscillations in CA3.

Bar charts showing raw gamma power (μV^2) in KA conditions (black) and following bath application of 10μM tianeptine (green). (A) 2 weeks AMC, (B) 3 weeks AMC, (C) 4 weeks AMC, (D) 5 weeks AMC, (E) 6 weeks AMC, and (F) late AMC. Error bars show SEM. ** denotes $p \leq 0.01$, and *** denotes $p \leq 0.001$ (Wilcoxon matched-paired signed rank test).

Overall, this demonstrates acute tianeptine can potentiate both spontaneous and KA-induced gamma oscillations in both CA1 and CA3 in the hippocampus of control animals, therefore increasing network excitability. Further consolidation of this is found in figure 4.5. which shows the combined % change of both CA1 and CA3 following application of tianeptine in spontaneous conditions (figure 4.5. A) and in the presence of KA (figure 4.5. B).

Figure 4.5. A shows the combined percentage increase from spontaneous gamma oscillations to tianeptine, with a 422.3 ± 52.4% increase in CA1 (n = 52) and 656.7 ± 268.7% in CA3 (n = 50, p = ns). Likewise, figure 4.5. B shows the combined percentage increase from KA-induced gamma oscillations to tianeptine, with a 479.3 ± 87.2% increase in CA1 (n = 54) and 420.0 ± 96.9% in CA3 (n = 66, p = ns). This demonstrates tianeptine can potentiate both CA1 and CA3 to the same degree in both spontaneous and KA conditions.

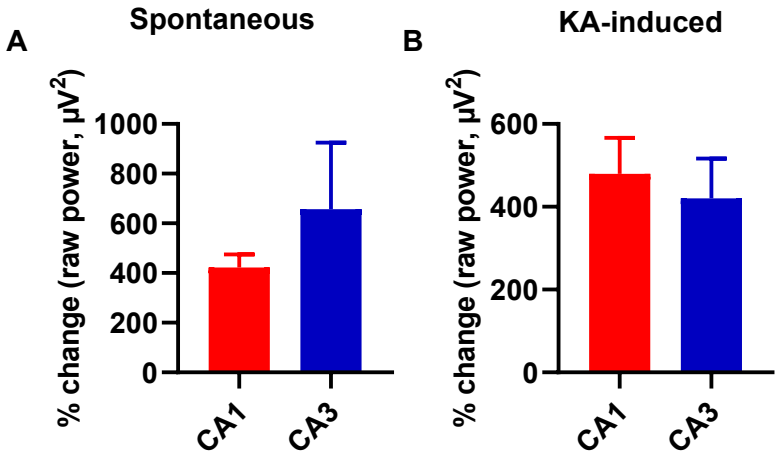

Figure 4.5. Combined percentage increase following tianeptine application in spontaneous and KA conditions.

Bar charts showing % change of raw gamma power (μV²) follow tianeptine application in spontaneous conditions (A) and KA conditions (B). Red bars indicate CA1, and blue bars indicate CA3. Error bars show SEM (Mann-Whitney test).

4.2.3. Effect of acute tianeptine on synaptic neurotransmission in CA1

Whole-cell voltage-clamp experiments were conducted to investigate the effect acute 10μM tianeptine has on sEPSCs of control hippocampal CA1 pyramidal cells. The standard patch method was used (chapters 2.2, 2.3.2). Like LFP experiments, timepoints to match the equivalent ages during the latent period (weeks 2, 3, 4, 5 and 6 post-induction) and SRS (>3 months post-induction, named 'late AMC') were taken. Parameters studied to assess the effect

of tianeptine on sEPSCs were amplitude (pA), decay time constant (tau, ms) and interevent interval (IEI, ms). To maintain consistency, only CA1 pyramidal cells were studied.

For sEPSC amplitude, there is a trending increase in the size of sEPSCs once 10μM tianeptine is bath applied onto slices (figure 4.6. A). This was only significantly different at 2 weeks AMC, with baseline events showing a mean median peak amplitude of 10.0 ± 1.1 pA (n = 6) which increases to 13.6 ± 1.8 pA (n = 6, $p \leq 0.05$) once tianeptine is added.

Both decay tau (figure 4.6. B) and IEI (figure 4.6. C) found no significant differences between baseline and the addition of tianeptine across all timepoints studied. Meaning, tianeptine likely does not affect the kinetics or frequency of sEPSCs, respectively.

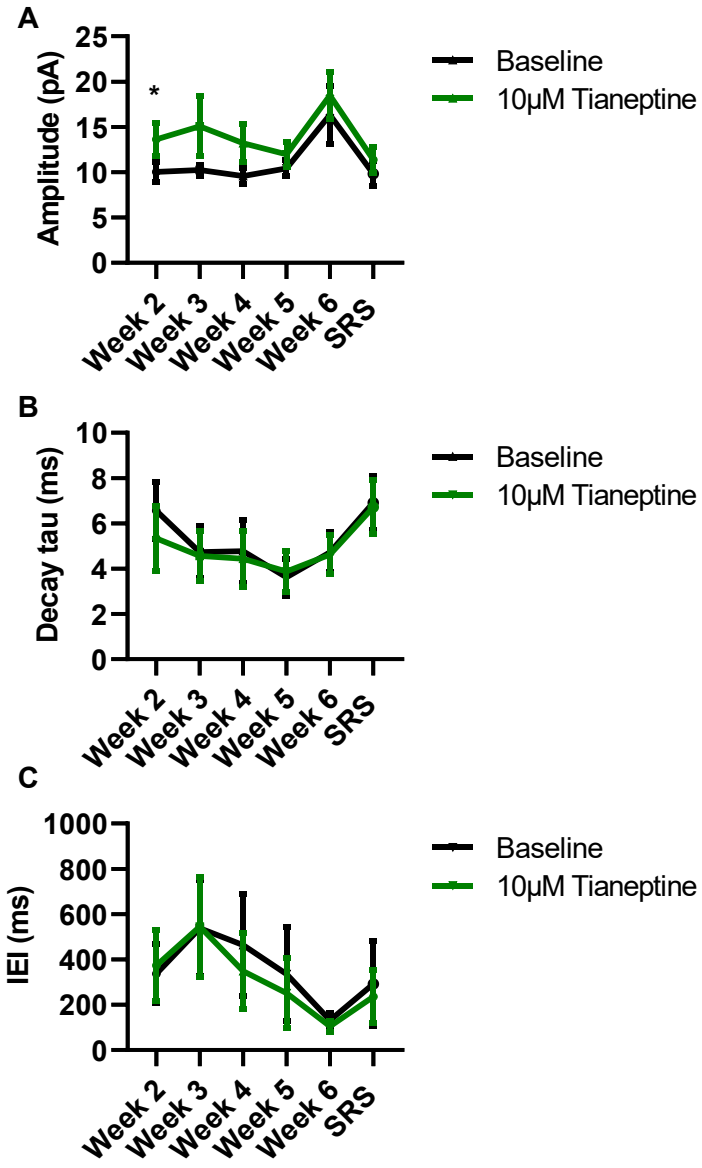

Figure 4.6. Changes in synaptic excitability by tianeptine.

Connected column mean graphs of sEPSC results for (A) mean median amplitude, (B) mean median decay tau, and (C) mean median IEI. Black lines indicate baseline and green lines indicate 10μM tianeptine. Error bars show SEM. * denotes $p \leq 0.05$ (Wilcoxon matched-pairs signed rank test).

4.3. Discussion

4.3.1. Pitfall in the whole-cell voltage clamp experiments

Overall, figures 4.1. – 4.5. demonstrate the ability for tianeptine to increase network activity and neurotransmission *in vitro*. This effect was more pronounced in LFP experiments (figures 4.1. – 4.5.) than in whole-cell patch clamp recordings (figure 4.6.). This is likely due to the smaller number of repeats done for patch clamp experiments due to time constraints. As there is a clear trend emerging for peak amplitude following tianeptine application (figure 4.1. A), future work may look to explore the effects of tianeptine further with larger data sets, therefore improving the reliability of the results. Other studies investigating the acute effects of tianeptine on EPSCs of hippocampal pyramidal cells have found a two-fold increase in peak amplitude and an increase in decay time (Kole et al., 2002, Pillai et al., 2012). Meaning, it is likely figure 4.6. was unable to highlight this increase in EPSC effectively.

4.3.2. Mechanisms by which tianeptine potentiates oscillations

However, when studying the effects of tianeptine on local field network activity, a highly significant and robust increase is observed across both CA1 and CA3 in both spontaneous and KA-induced conditions across all timepoints studied. Current understanding of the mechanisms of tianeptine fit with increased network activity, with phosphorylation of certain sites on the GluA1 AMPAR subunit and increased phosphorylation of intracellular kinases (e.g., CaMKII) leading to AMPAR potentiation and increased function in the hippocampus (McEwen et al., 2010). Thus, increased insertion/anchoring and conductance of post-synaptic AMPARs in the hippocampus will increase gamma oscillations both with and without the presence of KA.

Phosphorylation of just one of the two target serine residues on the GluA1 subunit of AMPARs has been found to regulate AMPAR-mediated synaptic activity. Specific activation of PKC by phorbol esters results in phosphorylation of Ser831, and specific activation of PKA by either forskolin or 3-isobutyl-1-methylxanthine (IBMX) results in phosphorylation of the Ser845. This resulted in increased synaptic activity via functional modulation of AMPARs (Blackstone et al., 1994, Roche et al., 1996). As mentioned above, phosphorylation of Ser831 is associated with increased AMPAR channel conductance (Derkach et al., 1999, Jenkins and Traynelis, 2012), while phosphorylation of Ser845 is associated with increased AMPAR trafficking and stabilisation in the post-synaptic membrane, and decreased AMPAR internalisation (Lee et al., 2000, Liu et al., 2009, Man et al., 2007).

Tianeptine can modulation both serine residues on the GluA1 AMPAR subunit, therefore increasing overall AMPAR neurotransmission in the hippocampus, and resulting increased local field activity (Szegedi et al., 2011, Zhang et al., 2013). This modulation of intracellular kinase activity by tianeptine is confirmed by Kole *et al.*, who found this increased EPSC activity by tianeptine is neutralised in the presence of the broad-spectrum kinase inhibitor

staurosporine. Staurosporine primarily effects PKC activity but has been noted to also modulate PKA and CaMKII activity (Kole et al., 2002, Tamaoki et al., 1986).

Centrally, if tianeptine can potentiate local field network activity *in vitro* via AMPAR neurotransmission, then AMPAR antagonists should attenuate neurotransmission. The use of different AMPAR antagonists have been found to reduce hippocampal neurotransmission, including the selective, non-competitive AMPAR antagonists CP 465022 (Menniti et al., 2003), the competitive AMPAR/KAR antagonists CNQX and DNQX (Andreasen et al., 1989), the selective, non-competitive AMPAR antagonists GYKI 52466 (Tarnawa et al., 1992), and the non-selective GluA1 and GluA3 AMPAR subunit antagonist Philanthotoxin 74 (Lu et al., 2009). Thus, showing the effect potentiation and attenuation of AMPARs have on increasing and decreasing local field and synaptic activity respectively.

It is also worth noting that studies have demonstrated that tianeptine is a full agonist of the mu opioid receptor (MOR). Widely expressed in the hippocampus, MOR is a Gi/o-coupled receptor, with presynaptic activation altering neuron excitability via suppression of presynaptic release of GABA. Activation of MOR requires a smaller concentration than that of glutamatergic receptors, meaning Gassaway *et al.* hypothesises that tianeptine's modulation of the glutamatergic system may occur indirectly, via opioid receptor signalling. For example, activation of MOR on CA1 inhibitory interneurons results in decreased activity, therefore disinhibiting CA1 glutamatergic neurons, resulting in enhanced excitability. As such, it cannot be ignored the role MORs may be playing in potentiating both spontaneous and KA-mediated gamma oscillations in the hippocampus (Gassaway et al., 2014, Samuels et al., 2017, Svoboda et al., 1999). An option for ruling out the role MOR activation may play in gamma oscillation potentiation using tianeptine would be to coapply a MOR antagonist (e.g., naloxone).

Overall, acute application of tianeptine results in rapid and dynamic increases in local field and synaptic activity in the hippocampus. Understanding the physiological effects of tianeptine has therapeutic application in disorders which may be associated with reductions in AMPAR-mediated neurotransmission.

Chapter 5 The effect of tianeptine during epileptogenesis *in vitro*

5.1. Introduction

In chapter 3, it has been shown there is a reduction in network excitability in the hippocampus *ex vivo* in both spontaneous and KA-induced conditions during epileptogenesis, particularly during the latent period (weeks 5 – 6 post-induction). Previous work studying epileptogenesis using the RISE model hypothesises this reduction in network excitability is due to a specific loss of AMPAR-mediated neurotransmission. Interestingly, there continues to be a loss of AMPARs even once animals enter the SRS stage of epileptogenesis. Suggesting, this hypoexcitability during the latent period is possibly associated with the progression of epileptogenesis (Needs et al., 2019). Chapter 4 then investigated the hippocampal physiological response to bath applied 10μM tianeptine *in vitro* and confirmed the idea that tianeptine modulates network activity via postsynaptic AMPAR neurotransmission (McEwen et al., 2010).

Epilepsy is described as an imbalance of excitation and inhibition (E/I balance). Notably, epilepsy has been associated with an increase in excitation and/or decrease in inhibition, leading to the emergence of hyperexcitability and hypersynchronous seizures. As such, the majority of the anti-epileptic drugs available are aimed at restoring E/I balance, therefore reducing seizure intensity and frequency (e.g., carbamazepine and topiramate) (Shao et al., 2019). Our understanding of epileptogenesis from the RISE model looks to challenge this idea. It is hypothesised that a loss of AMPAR neurotransmission in the hippocampus, i.e., loss of excitation, will lead to the development of epileptic seizures. This introduces the question: is it possible to modify AMPAR neurotransmission, and therefore slow/prevent the progression to clinical seizures? As described in chapter 4, a drug with anti-epileptogenic potential could be tianeptine. Given the ability for tianeptine to increase AMPAR channel conductance while increasing postsynaptic AMPAR insertion and stabilisation (McEwen et al., 2010), tianeptine could be used as a way of normalising this E/I imbalance by increasing neuronal excitability.

As such, chapter 5 will look to combine these two ideas by exploring the effect of tianeptine on local field and synaptic activity in the hippocampus of both RISE animals and AMC during epileptogenesis *in vitro*. Like chapters 3 and 4, timepoints exploring the latent period (weeks 2 – 6 post-induction) and the SRS (>3 months post-induction) stages of epileptogenesis were explored. The effect of tianeptine was again explored in both spontaneous and KA-induced conditions.

5.2. Results

5.2.1. The effect of tianeptine on spontaneous network activity for AMC and RISE

Horizontal hippocampal-entorhinal slices were prepared of AMC and RISE-induced rats during timepoints for the latent period (weeks 2, 3, 4, 5, and 6 post-induction) and SRS (>3 months post-induction) using the standard LFP method (chapter 2.5.). Healthy brain slices are known

to readily generate spontaneous gamma oscillations in both CA1 and CA3 region of the hippocampus. Like chapters 3 and 4, two analysis parameters were examined to assess the differences in network excitability – peak raw power and area under the curve (AUC). A band-pass of 15 – 49 Hz was used to isolate gamma frequencies.

Following stabilisation of spontaneous gamma band activity for at least 30 minutes, 10μM tianeptine was added for a further 30 minutes minimum. Figure 5.1. shows the normalised % change (increase) following acute bath application of 10μM tianeptine in AMC and RISE animals across all timepoints studied. Data is normalised to baseline conditions (pre-tianeptine). In CA1 (figure 5.1. Ai, Bi) there are trending decreases in network excitability in RISE animals as the latent period progresses following application of tianeptine when employing both raw power and AUC analyses. For raw power analysis (figure 5.1. Ai), AMC saw a 2.7- to 4-fold increase in network activity in spontaneous gamma oscillations in CA1 following bath application of tianeptine across all timepoints studied. This differs from RISE animals, with a trending decrease in response to tianeptine as the latent period progresses, and normalisation back to control as animals reach the SRS stage of epileptogenesis. Significantly, week 6 post-induction has the largest difference in response to tianeptine, with AMC showing a 404.3 ± 89.4% (n = 10 increase in spontaneous gamma oscillations in CA1 following acute application of tianeptine, compared to 180.6 ± 82.1% (n = 7, $p \leq 0.05$) in RISE animals. For AUC analysis (figure 5.1. Bi), a similar story emerges with RISE animals showing the weakest response to acute tianeptine application at week 6 post-induction. AMC shows a 319.4 ± 54.3% (n = 11) increase in spontaneous gamma oscillations in CA1 following acute application of tianeptine, compared to 176.8 ± 53.0% (n = 7, $p \leq 0.05$) in RISE animals. These data suggest that, although spontaneous gamma oscillations can respond to tianeptine and increase network excitability in RISE animals during the latent period, this response is defective and follows the trend of decreased network excitability during epileptogenesis.

Moreover, in CA3 (figure 5.1. Aii, Bii), a similar story emerges. For raw power analysis (figure 5.1. Aii), a trending decrease in response to tianeptine application into the latent period is observed in RISE animals. Compared to CA1, this becomes significant slightly earlier, by week 5 post-induction. For AMC, there is a 396.4 ± 89.3% (n = 7) increase in spontaneous gamma oscillations in CA3 following tianeptine application. For RISE, this is reduced to a 151.8 ± 55.0% (n = 10, $p \leq 0.01$) increase in RISE animals. This continues into 6 weeks post-induction, with AMC showing a 285.3 ± 66.1% (n = 8) increase in spontaneous gamma oscillations following tianeptine application, compared to 97.2 ± 16.6% (n = 6, $p \leq 0.01$) change in RISE animals. Interestingly, CA3 6 weeks post-induction was the first time tianeptine had an opposing effect and decreased spontaneous gamma activity by 2.8%. For AUC analysis (figure 5.1. Bii), a trending decrease in tianeptine responsiveness into the latent period is also observed. This also becomes first significant at 5 weeks post-induction, with AMC showing a 399.6 ± 70.5% (n = 7) increase in spontaneous gamma activity compared to 178.6 ± 24.1% (n = 10, $p \leq 0.01$) in RISE animals. This continues into week 6 post-induction, with AMC showing

a 252.1 ± 40.6% (n = 8) increase in spontaneous gamma activity compared to 111.9 ± 14.5% (n = 6, $p \leq 0.01$) in RISE animals. Meaning, network excitability and responsiveness to tianeptine is blunted in CA3 in RISE animals during the latent period compared to AMC. In raw power analysis, but not AUC analysis, there is a small decrease in spontaneous network activity in CA3, meaning tianeptine decreases network excitability at 6 weeks post-induction.

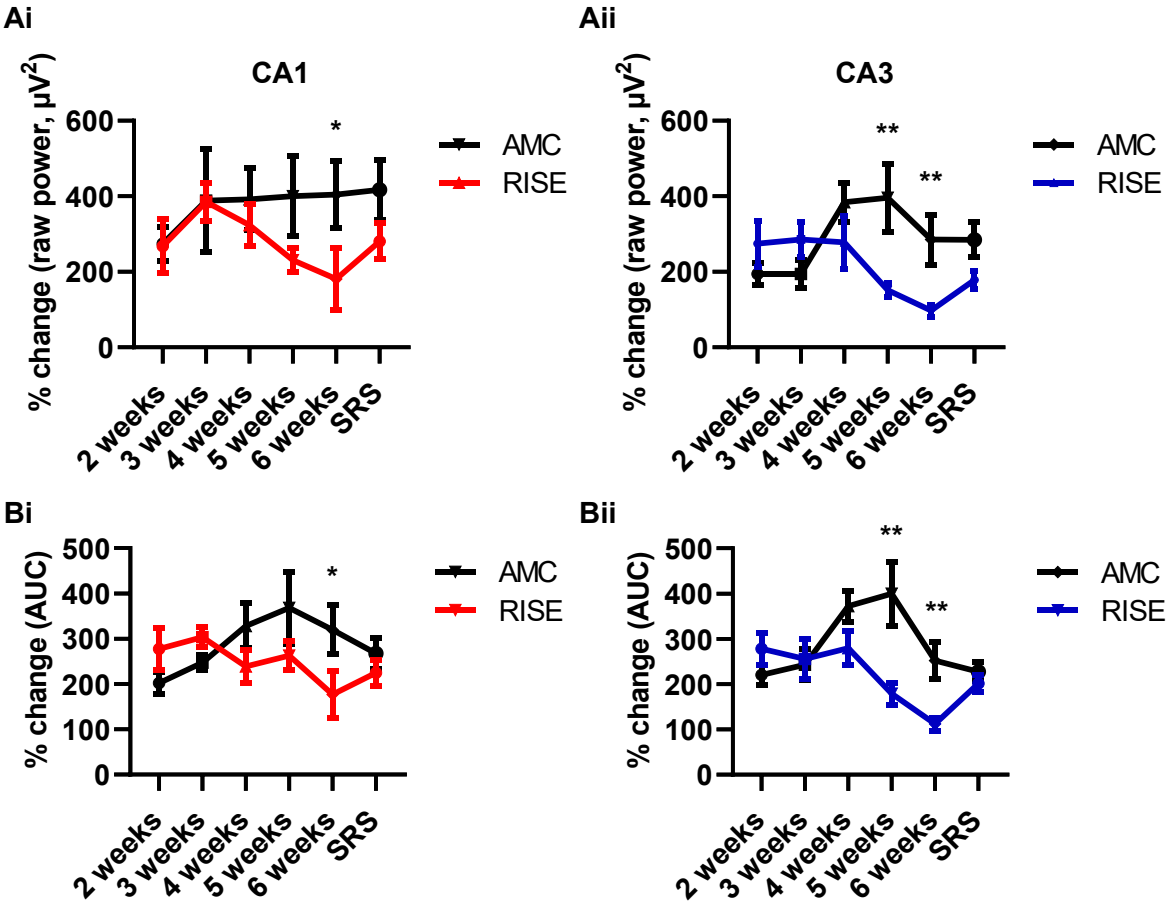

Figure 5.1. Comparison of tianeptine response on spontaneous network excitability in the hippocampus throughout epileptogenesis for AMC and RISE.

Connected column mean graphs of weeks 2, 3, 4, 5, 6 and SRS (>3 months) post-induction. (A) Graphs Ai and Aii show normalised % change from baseline to tianeptine of raw peak power (μV^2) for CA1 and CA3, respectfully. (B) Graphs Bi and Bii show % change of AUC analysis for CA1 and CA3, respectfully. A manual band-pass of 15 – 49 Hz was used to isolate gamma oscillations. Red (left) represents CA1 and blue (right) represents CA3. Error bars show SEM. * denotes $p \leq 0.05$ and ** denotes $p \leq 0.01$ (Mann-Whitney test).

5.2.2. The effect of tianeptine on spontaneous network activity for AMC and RISE – 6 weeks post-induction

As shown by figure 5.1., both CA1 and CA3 show significant deficits in response to tianeptine in spontaneous conditions in RISE animals by 6 weeks post-induction. The next section of this chapter will be delving more deeply into the spontaneous local field changes which occur in week 6 post-induction in CA1 (figure 5.2.) and CA3 (figure 5.3.) of the hippocampus following application of tianeptine.

Figure 5.2. shows the response to tianeptine in spontaneous conditions in AMC animals (figure 5.2. Ai – Aiv) and RISE animals (figure 5.2. Bi – Biv) in CA1. In AMC, there is a clear increase in gamma power following bath application of 10μM tianeptine. Figure 5.2. Ai shows an example FFT with its corresponding raw trace (figure 5.2. Aii). A highly synchronous gamma peak forms ~30Hz following application of tianeptine. Peak raw gamma power saw an increase from 5.7 ± 2.8 μV^2 (figure 5.2. Aiii, n = 10) for spontaneous gamma oscillations to 21.2 ± 10.5 μV^2 (n = 10, $p \leq 0.01$) following the addition of tianeptine. Peak gamma frequency also saw a significant change, with the spontaneous gamma rhythm oscillating at 30.7 ± 1.2 Hz (figure 5.2. Aiv, n = 10) and decreasing to 27.0 ± 0.7 Hz (n = 10, $p \leq 0.01$) following application of tianeptine.

However, in RISE animals 6 weeks post-induction, smaller, less coherent gamma oscillations emerge following bath application of tianeptine in CA1. Figure 5.2. Bi shows an example FFT with its corresponding raw trace (figure 5.2. Bii). There is no defined gamma peak followed application of tianeptine, showing defective network synchrony (despite showing small but coherent gamma oscillations during spontaneous conditions). There is also the emergence of this slower frequency element oscillating at ~5Hz. Peak raw gamma power saw no change following bath application of tianeptine (spontaneous gamma saw 0.9 ± 0.4 μV^2, n = 7; 10μM tianeptine saw 1.0 ± 0.3 μV^2, p = ns, figure 5.2. Biii). Similarly, peak gamma frequency also saw no change following bath application of tianeptine (spontaneous gamma saw 22.9 ± 1.2 Hz, n = 8; 10μM tianeptine saw 22.1 ± 2.5 Hz, n = 8, p = ns, figure 5.2. Biv).

Equally, figure 5.3. shows the response to tianeptine in AMC animals (figure 5.3. Ai – Aiv) and RISE animals (figure 5.3. Bi – Biv) in CA3 at 6 weeks post-induction. In AMC, there is a sustained increase in gamma power following bath application of 10μM tianeptine. Figure 5.3. Ai shows an example FFT with its corresponding raw trace (figure 5.3. Aii). Again, a highly synchronised gamma peak forms ~30Hz following application of tianeptine in CA3. Peak raw gamma power saw an increase from 182.6 ± 78.2 μV^2 (figure 5.3. Aiii, n = 7) for spontaneous gamma oscillations to 505.4 ± 263.1 μV^2 (n = 7, $p \leq 0.05$) following the addition of tianeptine. Peak gamma frequency also saw a significant change, with the spontaneous gamma rhythm oscillating at 31.7 ± 1.2 Hz (figure 5.3. Aiv, n = 7) and decreasing to 28.4 ± 1.3 Hz (n = 7, $p \leq 0.05$) following application of tianeptine.

However, in RISE animals 6 weeks post-induction, low amplitude, low coherent gamma oscillations emerge following bath application of tianeptine in CA3 also. Figure 5.3. Bi shows an example FFT with its corresponding raw trace (figure 5.3. Bii). Although still possible to identify the peak, tianeptine produces broadband gamma oscillations in spontaneous conditions in CA3. Peak raw gamma saw no change following bath application of tianeptine (spontaneous gamma saw 2.4 ± 1.7 μV^2, n = 6; 10μM tianeptine saw 1.9 ± 1.3 μV^2, n = 6, p = ns, figure 5.3. Biii). Similarly, peak gamma frequency also saw no change following bath application of tianeptine (spontaneous gamma saw 29.4 ± 4.2 Hz, n = 6; 10μM tianeptine saw 24.0 ± 2.7 Hz, n = 6, p = ns, figure 5.3. Biv).

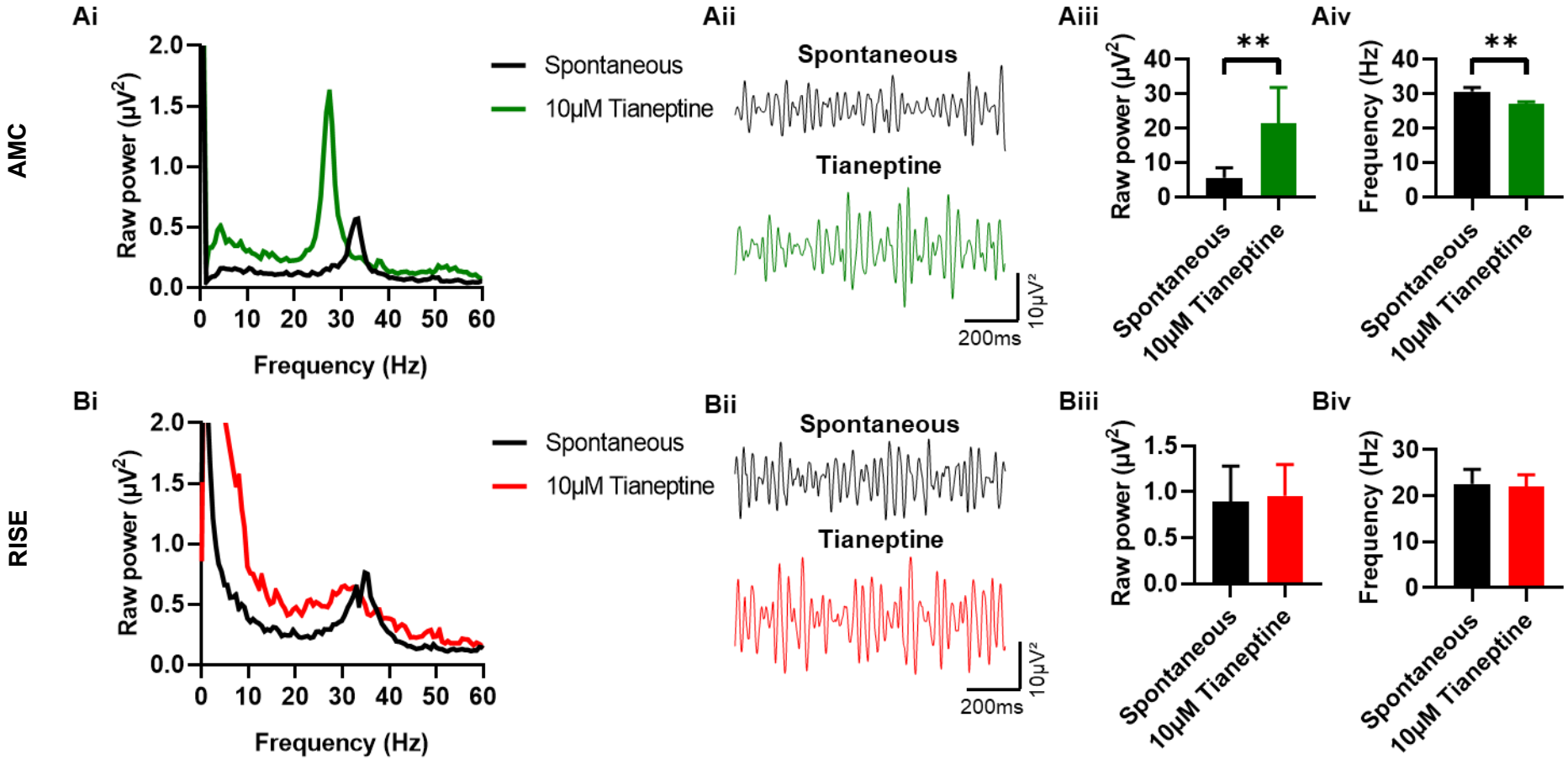

Figure 5.2. Exploring the effect of tianeptine in CA1 - week 6 post-induction of epileptogenesis.

(A) represents AMC and (B) represents RISE. (Ai) AMC example FFT showing spontaneous oscillations (black) and in the presence of 10μM tianeptine (green). (Aii) one second raw trace from the same experiment (IIR filtered to a band-pass of 15 – 49 Hz). (Aiii) bar chart showing raw gamma power for both spontaneous and tianeptine. (Aiv) bar chart showing peak gamma frequency for spontaneous and tianeptine. (Bi) RISE example FFT showing spontaneous oscillations (black) and in the presence of 10μM tianeptine (red). (Bii) one second raw trace from the same experiment (IIR filtered to a band-pass of 15 – 49 Hz). (Biii) bar chart showing raw gamma power for both spontaneous and tianeptine. (Biv) bar chart showing peak gamma frequency for spontaneous and tianeptine. Error bars show SEM. ** denotes $p \leq 0.01$ (Wilcoxon matched-pairs signed rank test).

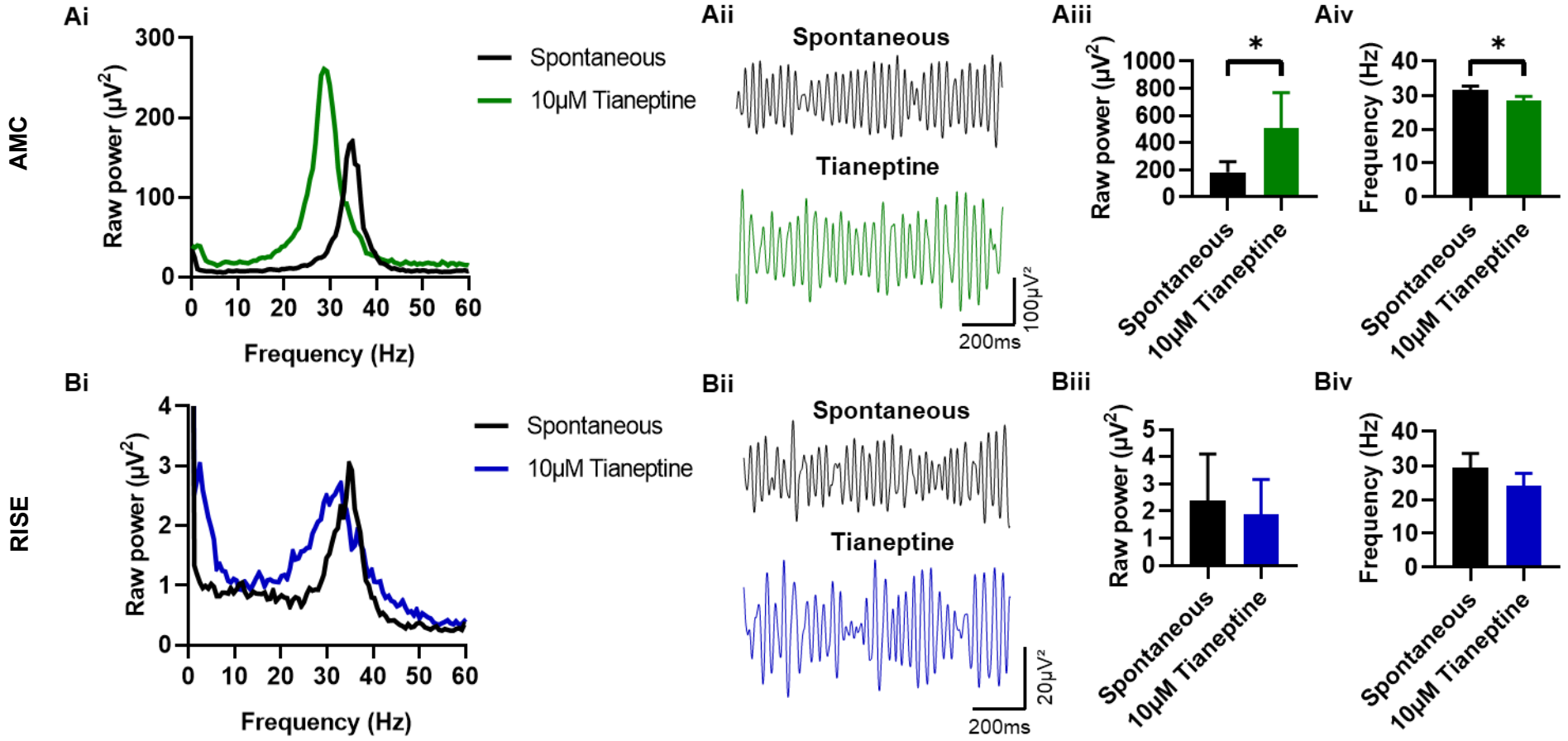

Figure 5.3. Exploring the effect of tianeptine in CA3 - week 6 post-induction of epileptogenesis.

(A) represents AMC and (B) represents RISE. (Ai) AMC example FFT showing spontaneous oscillations (black) and in the presence of 10μM tianeptine (green). (Aii) one second raw trace from the same experiment (IIR filtered to a band-pass of 15 – 49 Hz). (Aiii) bar chart showing raw gamma power for both spontaneous and tianeptine. (Aiv) bar chart showing peak gamma frequency for spontaneous and tianeptine. (Bi) RISE example FFT showing spontaneous oscillations (black) and in the presence of 10μM tianeptine (red). (Bii) one second raw trace from the same experiment (IIR filtered to a band-pass of 15 – 49 Hz). (Biii) bar chart showing raw gamma power for both spontaneous and tianeptine. (Biv) bar chart showing peak gamma frequency for spontaneous and tianeptine. Error bars show SEM. * denotes $p \leq 0.05$ (Wilcoxon matched-pairs signed rank test).

Taken together, these data confirm spontaneous local field gamma oscillations at 6 weeks post-induction are heavily defective in RISE animals. Furthermore, it appears acute bath application of 10μM tianeptine is unable to recover spontaneous oscillations in both CA1 and CA3, with both peak power and the frequency showing deficits. The next section of this thesis will explore the effects of acute tianeptine application onto gamma oscillations already 'oscillating' in the presence of 200nM KA.

5.2.3. The effect of tianeptine on KA-induced network activity for AMC and RISE

Like the spontaneous experiments above, horizontal hippocampal-entorhinal slices were prepared from AMC and RISE-induced rats during timepoints for the latent period (weeks 2, 3, 4, 5, and 6 post-induction) and SRS (>3 months post-induction) using the standard LFP method (chapter 2.5.). Healthy brain slices are known to readily generate spontaneous gamma oscillations in both CA1 and CA3 region of the hippocampus, with bath application of 200nM KA potentiating these gamma oscillations. Two analysis parameters were examined to assess the differences in network excitability – peak raw power and area under the curve (AUC).

Following stabilisation of spontaneous gamma band activity for at least 30 minutes, 200nM KA was added for a further 30 minutes minimum. Following stabilisation of KA-induced gamma band activity, 10μM tianeptine was bath applied for a further 30 minutes. Figure 5.4. shows the normalised % change from baseline to tianeptine following acute bath application of 10μM tianeptine in AMC and RISE animals already oscillating in 200nM KA. In CA1 (figure 5.4. Ai, Bi) there is a trend towards decreased network excitability and responsiveness to tianeptine in RISE animals as the latent period progresses when employing both raw power and AUC analyses. For raw power analysis (figure 5.4. Ai), AMC saw a 2.7 – 5.5-fold increase in network activity in KA-induced gamma oscillations in CA1 following application of tianeptine across all timepoints studied. This differs from RISE animals, with a trending decrease in response to tianeptine as the latent period progresses, and 'normalisation' back to control as animals reach the SRS stage of epileptogenesis. There are significant differences between AMC and RISE at weeks 4 and 6 post-induction. At 4 weeks post-induction, AMC demonstrates a 420.0 ± 66.4% (n = 7) increase compared to a marginal 104.1 ± 30.0% (n = 12, $p \leq 0.001$) increase in KA-induced gamma oscillations following acute bath application of tianeptine. Likewise, at 6 weeks post-induction, AMC demonstrates a 441.8 ± 133.7% (n = 6) increase compared to 150.5 ± 28.0% (n = 8, $p \leq 0.05$) increase in RISE animals in KA-induced gamma oscillations following acute bath application of tianeptine. Interestingly, this response to tianeptine is regained once animals enter the SRS stage of epileptogenesis in CA1 (AMC increases by 556.9 ± 213.5%, n = 6; RISE increases by 432.0 ± 116.5%, n = 9, p = ns).

For AUC analysis of CA1 (figure 5.4. Bi), a similar story emerges with RISE animals showing reductions in network excitability and responsiveness to tianeptine as the latent period progresses, with 'recovery' once animals reach SRS. For AUC analysis, AMC saw a 1.6 – 3.1-fold increase in network activity in KA-induced gamma oscillations in CA1 following application

of tianeptine across all timepoints studied. Significant differences between AMC and RISE are demonstrated at weeks 4, 5, and 6 post-induction. At 4 weeks post-induction, AMC demonstrates a 221.4 ± 43.0% (n = 7) increase following tianeptine application. This differs hugely to RISE, which saw an overall decrease to 80.0 ± 17.6% (n = 12, $p \leq 0.01$) following tianeptine application – this is a 20% decrease in AUC compared to KA-only conditions. At 5 weeks post-induction, AMC demonstrates 190.4 ± 15.1% (n = 8) increase compared to a small 101.1 ± 28.3% (n = 8, $p \leq 0.01$) increase in RISE following tianeptine application. Likewise, at 6 weeks post-induction, AMC demonstrates 317.6 ± 107.6% (n = 6) increase compared to a marginal 124.1 ± 21.3% (n = 9, $p \leq 0.01$) increase in RISE following tianeptine application. As seen with raw power analysis, this response to tianeptine is regained once animals enter the SRS stage of epileptogenesis in CA1 (AMC increases by 264.1 ± 73.0%, n = 6; RISE increases by 232.8 ± 41.7%, n = 9, p = ns).

Overall, this demonstrates network excitability and responsiveness to tianeptine is dampened in the CA1 subregion of the hippocampus in RISE animals. This first emerges by 4 weeks post-inductions and continues into week 6 post-induction. It appears that responsiveness to tianeptine is regained once animals enter the SRS stage of epileptogenesis.

In CA3 (figure 5.4. Aii, Bii) there are trending decreased in network excitability and responsiveness to tianeptine in RISE animals as the latent period progresses when employing both raw power and AUC analyses. Significantly, unlike CA1, there does not appear to be recovery in response to tianeptine once animals enter the SRS stage of epileptogenesis. For raw power analysis (figure 5.4. Aii), AMC saw a 2.5 – 3.6-fold increase in network activity in KA-induced gamma oscillations in CA3 following application of tianeptine across all timepoints studied. This differs from RISE animals, with a trending decrease in response to tianeptine as the latent period progresses, and continuation of this decrease even once animals reach SRS. There are significant differences between AMC and RISE at weeks 4, 5, 6 and SRS post-induction. At 4 weeks post-induction, AMC has a 359.3 ± 76.0% (n = 9) increase in KA-induced gamma oscillations following application of tianeptine, compared to a decrease of 89.8 ± 28.8% (n = 10, $p \leq 0.001$) for RISE. This is a decrease in raw power of 10.2% at week 4 post-induction. By 5 weeks post-induction, AMC continues to respond effectively to tianeptine with a 255.7 ± 26.2% (n = 11), comparatively to RISE which appears to decrease further following application of tianeptine (85.0 ± 21.5%, n = 10, $p \leq 0.001$), showing a 15.0% decrease in peak gamma power. This develops further into 6 weeks post-induction, with AMC showing a 300.0 ± 54.5% (n = 11) increase in KA-induced gamma oscillations following tianeptine application, compared to a declining 78.4 ± 23.0% (n = 8, $p \leq 0.01$) change in RISE. Week 6 post-induction shows the largest reduction in raw gamma power in RISE animals, with a 21.6% reduction compared to peak gamma power in KA-only conditions. Finally, contrastingly to CA1, this lack of response to tianeptine continues into the SRS stage of epileptogenesis in CA3. For AMC, there is a 291.1 ± 73.0% (n = 8) increase in peak gamma power following application of tianeptine. For

RISE animals, there is a marginal 103.3 ± 14.7% (n = 8, $p \leq 0.01$) increase, meaning there is no real change following application of tianeptine onto KA-induced gamma oscillations.

For AUC analysis (figure 5.4. Bii), AMC saw a 1.7 – 2.6-fold increase in network activity in KA-induced gamma oscillations in CA3 following application of tianeptine across all timepoints studied. This differs from RISE animals, with a trending decrease in response to tianeptine as the latent period progresses, and continuation of this decrease even once animals reach SRS. There are significant differences between AMC and RISE at weeks 4, 5, 6 and SRS post-induction. At 4 weeks post-induction, AMC has a 264.6 ± 42.1% (n = 7) increase in KA-induced gamma oscillations following application of tianeptine, compared to a decrease of 72.0 ± 17.3% (n = 11, $p \leq 0.001$) for RISE. This is a decrease in AUC of 28.0% at week 4 post-induction. By week 5 post-induction, AMC continues to respond effectively to tianeptine with a 188.1 ± 19.4% (n = 10), comparatively to RISE which appears to decrease further following application of tianeptine (67.1 ± 14.4%, n = 10, $p \leq 0.001$), showing a staggering 32.9% decrease in gamma AUC. This continues into 6 weeks post-induction, with AMC showing a 235.2 ± 39.2% (n = 9) increase in AUC following tianeptine application, compared to a reduction to 72.2 ± 20.9% (n = 8, $p \leq 0.01$) in RISE animals. This is another reduction of 27.8% in AUC following application of tianeptine. Finally, as also shown in peak raw power analysis, reductions in responsiveness to tianeptine in RISE animals continues into the SRS stage of epileptogenesis. AMC demonstrates a 173.4 ± 36.0% (n = 8) increase following tianeptine application, compared to 94.2 ± 12.9% (n = 8, $p \leq 0.05$) reduction in RISE. Although this is still a decrease of 5.8% compared to KA-only conditions, this is an improvement when compared to reductions seen during the latent period following application of tianeptine.

To conclude, figure 5.4. shows acute application of 10μM tianeptine to *ex vivo* epileptic brain slices already oscillating with KA results in reduced responsiveness to tianeptine from week 4 post-induction in both CA1 and CA3, and even declines in overall peak raw gamma and AUC. Interestingly, there appears to be ‘recovery’ in CA1 once animals enter the SRS stage of epileptogenesis which is not replicated in CA3. This may be significant in our understanding of epileptogenesis and what drives this transition from the seizure-free latent period into the presentation of clinical seizures (SRS).

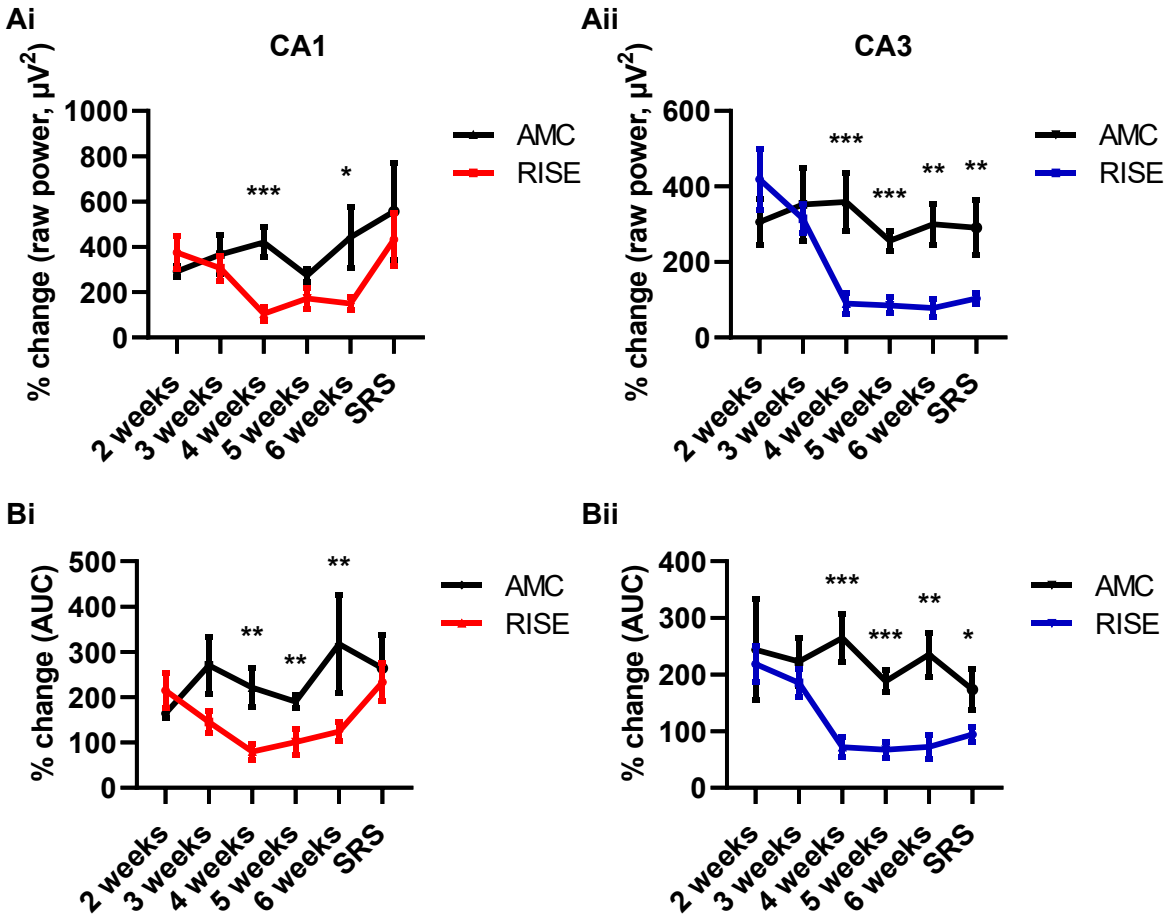

Figure 5.4. Comparison of tianeptine response on KA-induced network excitability in the hippocampus throughout epileptogenesis for AMC and RISE.

Connected column mean graphs of weeks 2, 3, 4, 5, 6 and SRS (>3 months) post-induction. (A) Graphs Ai and Aii show % change of raw peak power (μV^2) for CA1 and CA3, respectfully. (B) Graphs Bi and Bii show % change of AUC analysis for CA1 and CA3, respectfully. A manual band-pass of 15 – 49 Hz was used to isolate gamma oscillations. Red (left) represents CA1 and blue (right) represents CA3. Error bars show SEM. * denotes $p \leq 0.05$, ** denotes $p \leq 0.01$ and *** denotes $p \leq 0.001$ (Mann-Whitney test).

5.2.4. The effect of tianeptine on KA-induced network activity for AMC and RISE – SRS stage of epileptogenesis

As shown by figure 5.4., there appears to be 'recovery' in response to tianeptine in KA conditions in the CA1 subregion of the hippocampus once animals have reached the SRS stage of epileptogenesis. This contrasts with CA3, where there is little to no change following application of tianeptine. The next section of this chapter will be delving more deeply into the KA-mediated local field changes which occur during SRS in CA1 (figure 5.5.) and CA3 (figure 5.6.) of the hippocampus following application of tianeptine.

Figure 5.5. shows the response to tianeptine in KA conditions in AMC animals (figure 5.5. Ai – Aiv) and RISE animals (figure 5.5. Bi – Biv) in CA1. In AMC, there is a clear increase in gamma power following bath application of 10μM tianeptine. Figure 5.5. Ai shows an example FFT with its corresponding raw trace (figure 5.5. Aii). A highly synchronous gamma peak forms ~25Hz following application of tianeptine. Peak raw gamma power saw an increase from 25.4 ± 8.4 μV^2 (figure 5.5. Aiii, n = 9) for KA-induced gamma oscillations to 143.8 ± 57.6 μV^2 (n = 9, $p \leq 0.01$) following the addition of tianeptine. Peak gamma frequency also saw a significant change, with the KA-mediated gamma rhythm oscillating at 27.9 ± 1.1 Hz (figure 5.5. Aiv, n = 9) and decreasing to 23.9 ± 0.9 Hz (n = 9, $p \leq 0.01$) following application of tianeptine.

A similar trend emerges for RISE animals during the SRS stage of epileptogenesis. As seen in figure 5.5. Bi and Bii, CA1 is still able to produce robust gamma responses following bath application of both KA and tianeptine. Peak raw gamma power saw an increase from 244.7 ± 187.1 μV^2 (figure 5.5. Biii, n = 9) to 621.4 ± 302.2 μV^2 (n = 9, $p \leq 0.05$) following application of tianeptine. Peak gamma frequency also saw a significant change, with the KA-mediated gamma rhythm oscillating at 31.1 ± 0.7 Hz (figure 5.5. Biv, n = 9) and decreasing to 25.7 ± 1.6 Hz (n = 9, $p \leq 0.05$) following application of tianeptine.

Overall, this shows that despite a lack of response to tianeptine in KA conditions during the latent period of epileptogenesis (figure 5.4.), CA1 can 'recover' and regain network excitability during the SRS stage of epileptogenesis, with both the power and frequency of the gamma rhythm being comparable to AMC.

In contrast, it appears the tianeptine response in KA-mediated conditions continues to be defective into the SRS stage of epileptogenesis in CA3. Figure 5.6. shows the response to tianeptine in KA conditions in AMC animals (figure 5.6. Ai – Aiv) and RISE animals (figure 5.6. Bi – Biv). In AMC, there is an obvious increase in gamma power following bath application of 10μM tianeptine. Figure 5.6. Ai shows an example FFT with its corresponding raw trace (figure 5.6. Aii). A highly synchronous gamma peak forms ~2-Hz following application of tianeptine. Peak raw power saw an increase from 805.3 ± 336.1 μV^2 (figure 5.6. Aiii, n = 8) for KA-induced gamma oscillations to 2310.0 ± 1106.0 μV^2 (n = 8, $p \leq 0.01$) following the addition of tianeptine. Peak gamma frequency also saw a significant decrease, from 30.0 ± 1.1 Hz (figure 5.6. Aiv, n = 8) in KA-only conditions to 25.3 ± 1.5 Hz (n = 8, $p \leq 0.01$) following the addition of tianeptine.

This differs from the tianeptine response in KA-mediated conditions in the CA3 subregion of the hippocampus in RISE animals. As seen in figure 5.6. Bi and Bii, CA3 is able to produce a substantial and robust increase in gamma power following application of 200nM KA, but there are minimal changes in the peak gamma power once tianeptine is introduced. This is confirmed when analysing peak raw power, which saw no significant change following application of tianeptine (peak raw power for KA was 3947.0 ± 2986.0 μV^2, n = 8; peak raw power for tianeptine was 4763.0 ± 3415.0 μV^2, n = 8, p = ns). Interestingly, despite this lack of change in network excitability following application of tianeptine, the speed of the gamma rhythm is

maintained, with the KA-mediated gamma rhythm oscillating at 31.1 ± 0.7 Hz (figure 5.6. Biv, n = 8) and decreasing to 25.9 ± 1.0 Hz (n = 8, $p \leq 0.01$) following application of tianeptine.

Fundamentally, this tells us both CA1 and CA3 can respond effectively following bath application of 200nM KA during the SRS stage of epileptogenesis. However, following application of 10μM tianeptine, only CA1 can increase network excitability further. Furthermore, the speed of the gamma rhythm is maintained in both CA1 and CA3 even following application of tianeptine. This tells us there are specific deficits in network excitability in CA3 during SRS which may be significant in our understanding of what drives epileptogenesis and the presentation of clinical seizures.

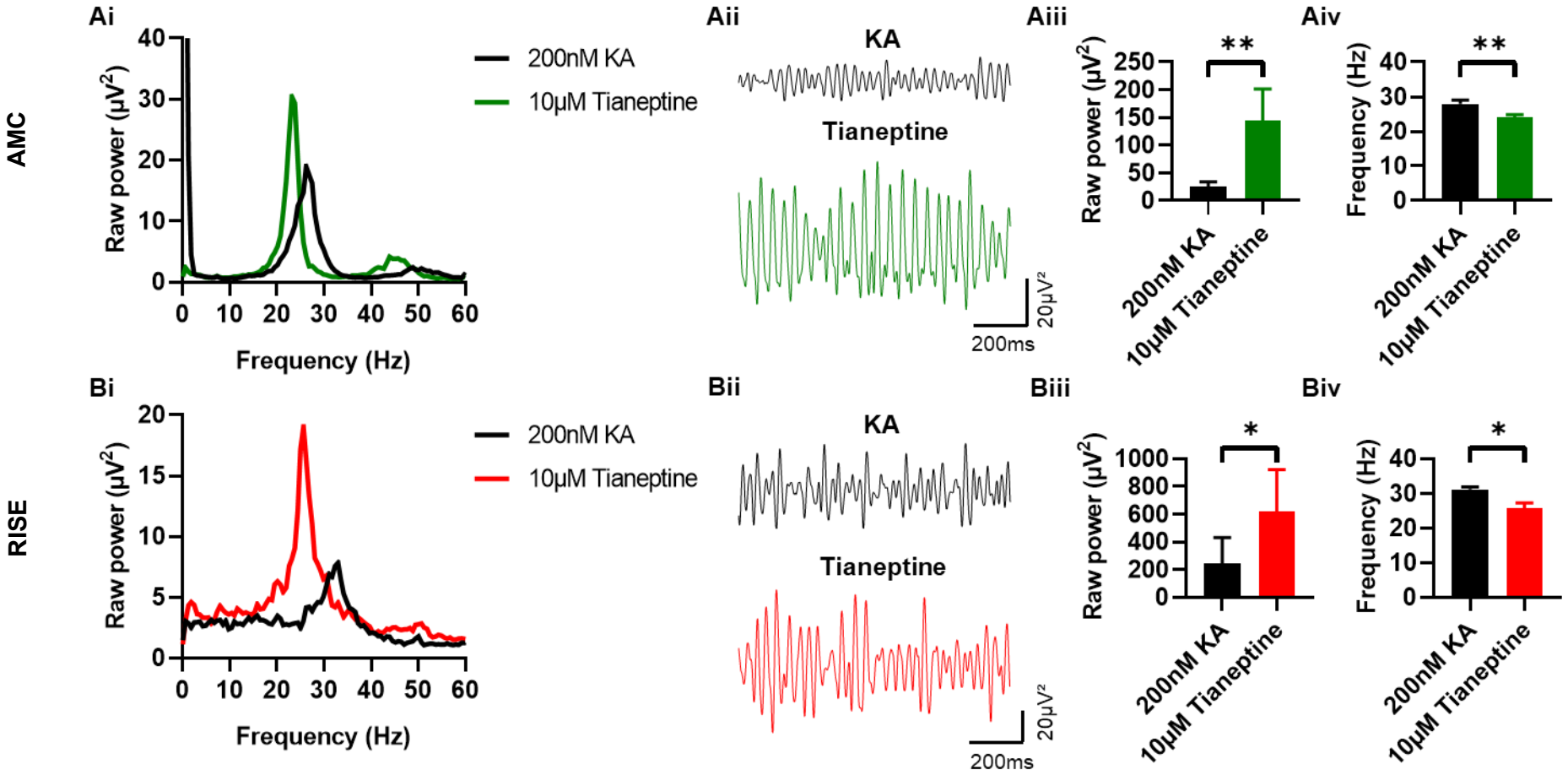

Figure 5.5. Exploring the effect of tianeptine in CA1 – SRS stage of epileptogenesis.

(A) represents AMC and (B) represents RISE. (Ai) AMC example FFT showing KA oscillations (black) and in the presence of 10μM tianeptine (green). (Aii) one second raw trace from the same experiment (IIR filtered to a band-pass of 15 – 49 Hz). (Aiii) bar chart showing raw gamma power for both KA and tianeptine. (Aiv) bar chart showing peak gamma frequency for KA and tianeptine. (Bi) RISE example FFT showing KA oscillations (black) and in the presence of 10μM tianeptine (red). (Bii) one second raw trace from the same experiment (IIR filtered to a band-pass of 15 – 49 Hz). (Biii) bar chart showing raw gamma power for both KA and tianeptine. (Biv) bar chart showing peak gamma frequency for KA and tianeptine. Error bars show SEM. * denotes $p \leq 0.05$ and ** denotes $p \leq 0.01$ (Wilcoxon matched-pairs signed rank test).

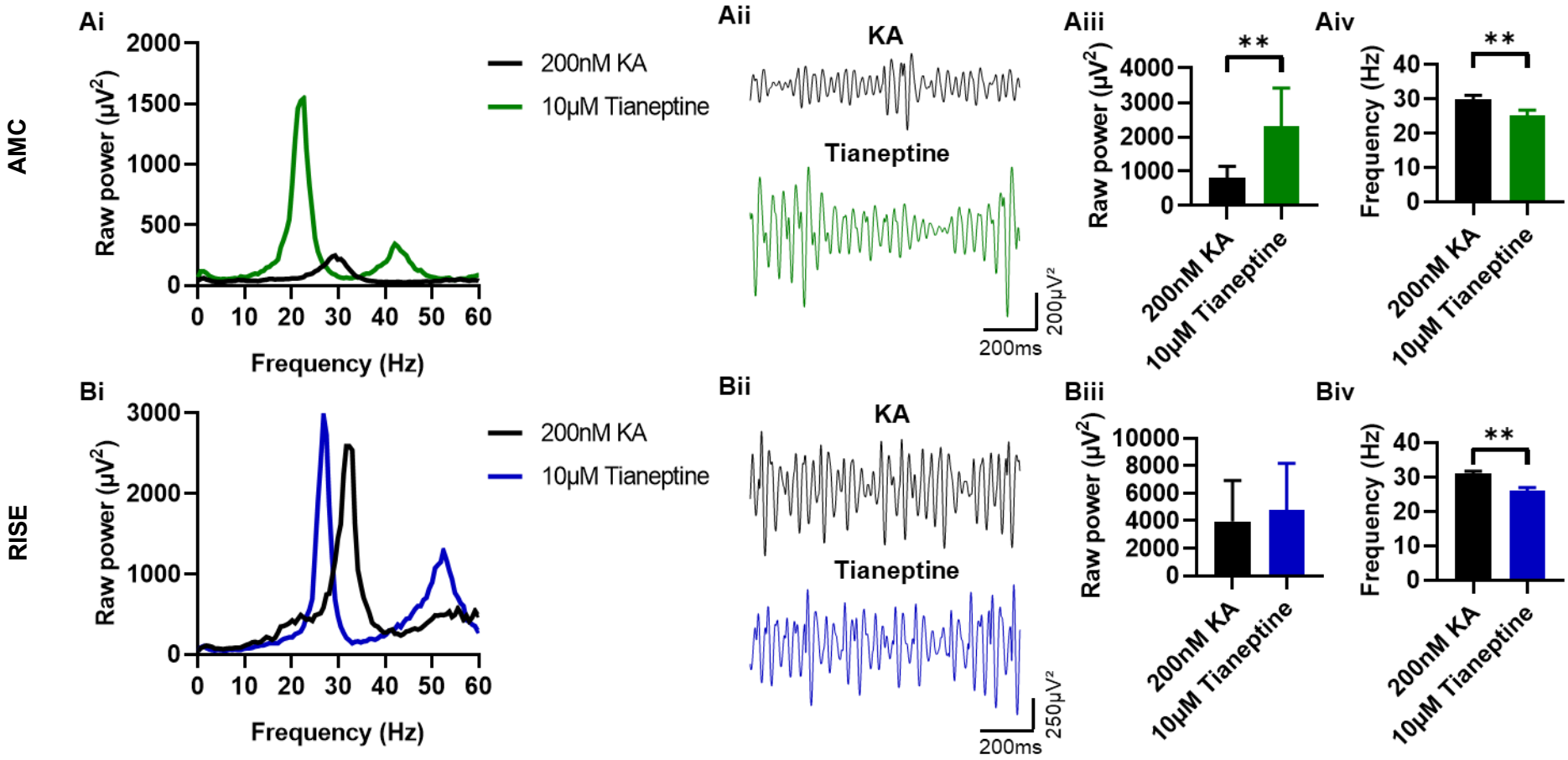

Figure 5.6. Exploring the effect of tianeptine in CA3 – SRS stage of epileptogenesis.

(A) represents AMC and (B) represents RISE. (Ai) AMC example FFT showing KA oscillations (black) and in the presence of 10μM tianeptine (blue). (Aii) one second raw trace from the same experiment (IIR filtered to a band-pass of 15 – 49 Hz). (Aiii) bar chart showing raw gamma power for both KA and tianeptine. (Aiv) bar chart showing peak gamma frequency for KA and tianeptine. (Bi) RISE example FFT showing KA oscillations (black) and in the presence of 10μM tianeptine (blue). (Bii) one second raw trace from the same experiment (IIR filtered to a band-pass of 15 – 49 Hz). (Biii) bar chart showing raw gamma power for both KA and tianeptine. (Biv) bar chart showing peak gamma frequency for KA and tianeptine. Error bars show SEM. ** denotes $p \leq 0.01$ (Wilcoxon matched-pairs signed rank test).

5.2.5. Network excitability and the transition from the latent period to SRS

Understanding the network dynamics which result in the transition from the latent period to the presentation of the first clinical seizure is imperative to preventing this transition to SRS. Figure 5.7. looks to summarise the effects of tianeptine on both spontaneous and KA-induced gamma oscillations in both CA1 and CA3 during the latent period (6 weeks post-induction) and the SRS stage of epileptogenesis.

In CA1, there are significant increases in network excitability following the transition from the latent period to SRS. Bath application of 10μM tianeptine onto spontaneous gamma oscillations results in an increase of raw gamma power from 180.6 ± 82.2% (figure 5.7. Ai, n = 7) during the latent period to 280.7 ± 47.7% (n = 7, $p \leq 0.05$) during SRS. Similarly, RISE animals already oscillating with KA increase from 150.5 ± 28.0% (figure 5.7. Aii, n = 8) during the latent period, compared to 432.0 ± 116.5% (n = 9, $p \leq 0.05$) during SRS following application of tianeptine. Meaning, overall network activity in CA1 is reduced during the latent period (6 weeks post-induction) which appears to recover once animals reach the SRS stage of epileptogenesis.

In CA3, there are only significant increases in network excitability following the transition from the latent period to SRS when tianeptine is applied to spontaneously oscillating brain slices. Bath application of 10μM tianeptine onto spontaneous gamma oscillations results in an increase of raw gamma power from 97.2 ± 16.6% (figure 5.7. Bi, n = 6) during the latent period, to 178.7 ± 23.7% (n = 7, $p \leq 0.05$) during SRS. Meaning, similar to CA1, there is an increase in network responsiveness and activity when tianeptine is applied to spontaneous gamma oscillations. However, this is not replicated when epileptic brain slices were pre-incubated with 200nM KA. There is a non-significant change between the latent period (6 weeks post-induction) and SRS when tianeptine is applied to brain slices already oscillating with KA. During the latent period, there is a decrease in peak power to 78.4 ± 23.0% (figure 5.7. Bii, n = 8) which is a reduction by 21.6% prior to tianeptine application. During the SRS stage of epileptogenesis, there is a small but non-significant increase to 103.3 ± 14.7% (n = 8, p = ns) following application of tianeptine. This shows that there is little improvement in network excitability between the latent period and SRS in CA3, and likely the introduction of KA prior to tianeptine has already pushed network excitability to its maximal rate. This could be fundamental in our understanding of network excitability and seizure initiation during epileptogenesis.

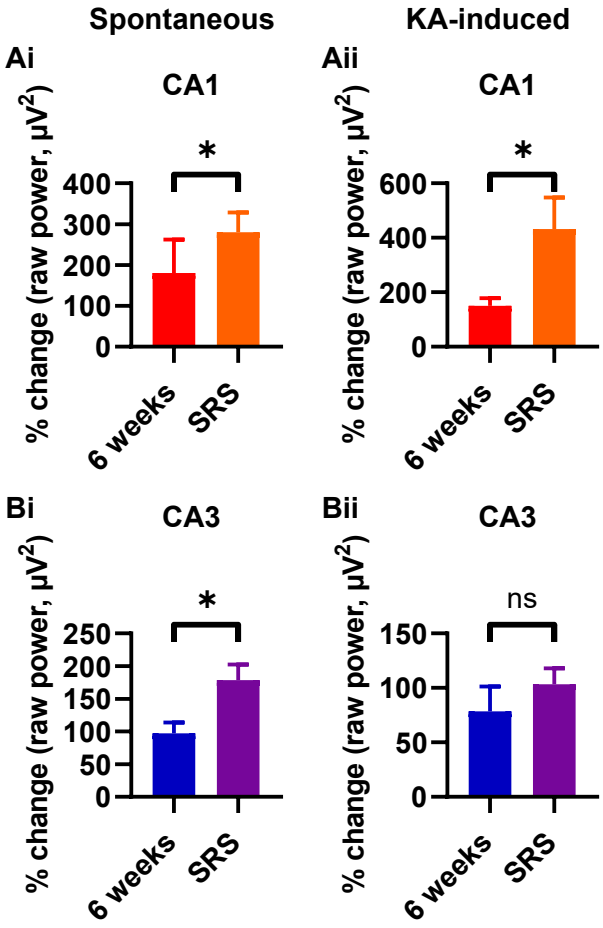

Figure 5.7. Comparison of network excitability during the latent period and SRS following tianeptine application in spontaneous and KA conditions.

Bar graphs showing % change of raw peak power (μV^2) between the latent period (6 weeks post-induction) and the SRS stage of epileptogenesis. (Ai) % change of tianeptine when applied to spontaneous gamma oscillations in CA1, (Aii) % change of tianeptine when applied to KA-induced gamma oscillations in CA1, (Bi) % change of tianeptine when applied to spontaneous gamma oscillations in CA3, and (Bii) % change of tianeptine when applied to KA-induced gamma oscillations in CA3. A manual band-pass of 15 – 49 Hz was used to isolate gamma oscillations. Red/orange represents CA1, and blue/purple represents CA3. Error bars show SEM. * denotes $p \leq 0.05$ (Mann-Whitney test).

5.2.5. The effect of tianeptine on synaptic activity during epileptogenesis

Whole-cell voltage-clamp experiments were conducted to investigate the changes to sEPSCs in AMC and RISE across the progression of epileptogenesis in the hippocampus using the standard patch method (chapters 2.2, 2.3.2). Like LFP experiments, timepoints during the latent period (weeks 2, 3, 4, 5 and 6 post-induction) and SRS (>3 months post-induction) were taken. Parameters studied to assess the effect of acute tianeptine application during epileptogenesis on sEPSCs were amplitude (pA), decay time constant (tau, ms) and interevent interval (IEI, ms). To maintain consistency and due to the fragility of neurons in CA3 following epileptogenesis, which is likely due to chronic inflammation, patch clamp recordings were only possible in the CA1 subregion of the hippocampus.

As can be seen in figure 5.8., there appears to be little difference in the response to tianeptine when comparing AMC and RISE across amplitude. However, for IEI of sEPSC in RISE animals (figure 5.8. C), there does seem to be a trending decrease in the frequency of sEPSCs as the latent period progresses, with 'recovery' again once animals reach the SRS stage of epileptogenesis when comparing to AMC. As described in chapter 4, it is likely the small data sets used for the effects of tianeptine on sEPSC are accounting for this lack of significance seen in the LFP data. As such, future work should look to use larger data sets.

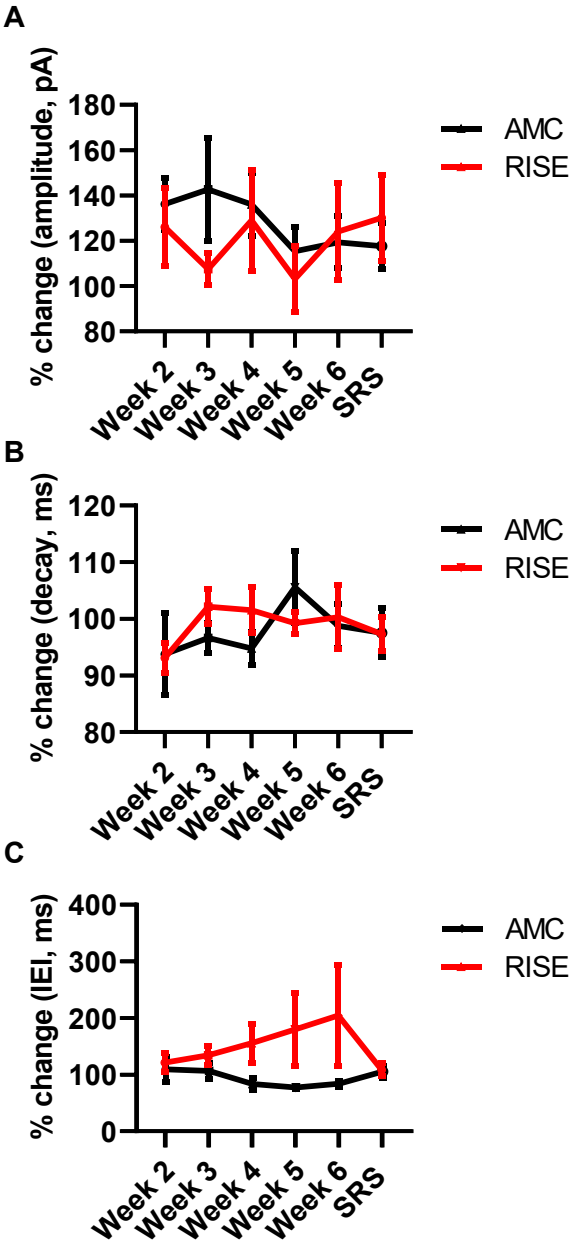

Figure 5.8. Changes in synaptic excitability by tianeptine in AMC and RISE.

Connected column mean graphs showing normalised % change of baseline to bath application of tianeptine sEPSC results for (A) mean median amplitude, (B) mean median decay tau, and (C) mean median IEI. Black lines indicate AMC and red lines indicate RISE following application of 10μM tianeptine.

5.3. Discussion

Studying the effects of tianeptine on network excitability in the hippocampus during epileptogenesis has shown us several significant network changes which may be central to the progression of epileptogenesis. Firstly, there appears to be a reduction in network excitability and response to tianeptine during the latent period in both spontaneous and KA-induced gamma oscillations. This deficit also extended to the frequency of the gamma oscillation. Secondly, although there is an overall boost in network excitability to KA during the SRS stage of epileptogenesis, only CA1 can increase further upon application of tianeptine. This discussion chapter looks to consider these polar changes in network excitability and how they may trigger the transition from the latent period to the presentation of clinical seizures.

5.3.1. Network excitability and the response to tianeptine during the latent period

As demonstrated in figure 5.1. – 5.4., the response to tianeptine becomes defective during the latent period in both spontaneous and KA-induced conditions. This is most consistent by week 6 post-induction, showing acute bath application of 10μM tianeptine was unable to rescue the network excitability in RISE animals. This is exhibited most obviously in figures 5.2. (Biii) and 5.3. (Biii) where there is no change in raw peak power to the already compromised gamma oscillations following bath application of tianeptine in CA1 and CA3, respectively.

Our understanding of the hippocampal receptor protein changes which occur during the latent period have come from studying the RISE model of epileptogenesis. There are significant reductions in the GluA1, GluA2 and GluA3 AMPAR subunits. In approximate terms, there is a ~80% reduction in the protein expression of the GluA1 subunit during the latent period of RISE animals compared to AMC. Also, there is ~50% reduction in the postsynaptic excitatory scaffolding protein PSD-95 (Needs et al., 2019). Hence, during the latent period, hippocampal neurons produce fewer GluA1-mediated AMPARs and lack the appropriate scaffold proteins to anchor the remaining AMPARs into the postsynaptic membrane, therefore resulting in reduced network excitability. As such, given the current understanding of the mode of action of tianeptine, it was thought tianeptine would be able to recover this deficit in network excitability.

Tianeptine is known to increase single channel conductance of AMPARs while also increasing AMPAR trafficking from extra-synaptic regions to the post-synaptic scaffold and decreasing AMPAR internalisation (Derkach et al., 1999, Lee et al., 2000, Man et al., 2007). Tianeptine also activates CaMKII which leads to phosphorylation the AMPAR auxiliary subunit stargazin, resulting in this AMPAR-stargazin interaction forming a complex with PDZ scaffold proteins (such as PSD-95) and increase anchoring in the postsynapse (Szegedi et al., 2011, Zhang et al., 2013). However, as shown in figures 5.1. – 5.4. tianeptine is either unable to increase network excitability in RISE animals during the latent period (no effect) or causes a reduction in overall network excitability compared to baseline activity.

The fact tianeptine is unable to change network excitability during the latent period could be because hippocampal neurons are simply not producing the protein necessary to assemble functional AMPARs (Needs et al., 2019). But, why in some cases would tianeptine cause a reduction in network excitability during the latent period in RISE animals? One possible explanation could be due to receptor desensitisation.

Glutamate-induced AMPAR desensitisation is a reduction in response to a sustained stimulus. In baseline conditions, AMPARs will undergo a two-step confirmational change which reduces AMPAR conductance. Desensitisation also increases synaptic diffusion, with ~50% of AMPARs continually cycling between postsynaptic and extra-synaptic locations. This increased lateral diffusion allows for exchange of desensitised receptors with naïve ones in the synapse, therefore allowing for sustainment of high-frequency synaptic transmission. The speed of this AMPAR diffusion is made possible by reduced interactions with the AMPAR auxiliary subunit stargazin. Stargazin, as mentioned above, is involved in AMPAR stabilisation in the PSD via its interaction with scaffolding proteins (e.g., PSD-95) (Bowie and Lange, 2002, Constals et al., 2015, Robert and Howe, 2003, Traynelis et al., 2010).

In this scenario, it is possible tianeptine is increasing lateral diffusion into the postsynaptic membrane initially. However, these AMPARs are unable to be anchored effectively in the postsynaptic membrane due to lack of scaffolding proteins during the latent period, resulting in desensitisation and lateral movement back to extra-synaptic locations, therefore decreasing network excitability further. Therefore, it is thought that this study of examining network excitability using tianeptine during the latent period is investigating the differences in localisation (postsynaptic vs extrasynaptic) of the remaining AMPARs during epileptogenesis.

Alternatively, it is possible that this acute bath application of tianeptine doesn't allow for effective incubation of tianeptine to have the desired effect on AMPAR trafficking and anchoring. Tramarin *et al*. studied re-recruitment and stabilisation of AMPARs in a model characterised by a mutation in the X-linked cyclin-dependent kinase-like 5 (CDKL5) gene which results in infantile seizures, impaired cognition and motor skills, and autistic features. Tianeptine was incubated for 7 days, and the authors found complete normalisation and restoration of both GluA1 and GluA2 AMPAR subunits into the cell membrane. Tianeptine was also able to restore lost accessory protein PSD-95 (Tramarin et al., 2018). Meaning, future work may look to incubate hippocampal slices *ex vivo* with tianeptine over a longer time period, or even dose RISE animals throughout different points within epileptogenesis.

Finally, another interesting phenomenon noted during the latent period is the non-significant change in peak gamma frequency seen in CA1 and CA3 in RISE animals following tianeptine when compared to AMC (figure 5.2. Biv, figure 5.3. Biv). The PING model of gamma oscillations states inhibitory interneurons generate $GABA_A$-induced IPSPs onto the perisomatic region of pyramidal cells, which results in shunting inhibition. Following decay of this IPSP, pyramidal cells can fire again, resulting in cyclic behaviour. The decay of this IPSP determines

the frequency of this oscillation, which typically runs in the gamma frequency range (Buzsáki and Wang, 2012). Even under spontaneous conditions, the gamma frequency is varied and incoherent which does not recover in the presence of tianeptine. It is hypothesised the incoherent synchrony of gamma oscillations is due to the lack of excitatory feedforward inputs from pyramidal cells onto inhibitory interneurons. Defective excitatory drive to interneurons will result in defective feedback inhibition, therefore incoherent gamma oscillations will develop. Tianeptine was unable to recover the excitatory drive by pyramidal cells, therefore having no effect on the frequency of the oscillation.

5.3.2. Network excitability and the response to tianeptine during the SRS stage of epileptogenesis

As demonstrated in figures 5.5. – 5.7., there appears to be an overall increase in network excitability in RISE animals during the SRS stage of epileptogenesis which increases further following acute bath application of 10μM tianeptine in all conditions except for CA3 that is already oscillating in KA-induced conditions (figures 5.4., 5.6.). In spontaneous conditions for both CA1 and CA3, application of tianeptine results in a comparable increase in network excitability to that of AMC ('recovery' in network activity). The same is also true for CA1 on KA-induced gamma oscillations. Despite GluA1, GluA2 and GluA3 AMPAR subunits in the hippocampus remaining substantially low once animals move into the SRS stage of epileptogenesis (Needs et al., 2019), there is increased network excitability. As described in chapter 3, this may be due to homeostatic plasticity. Pyramidal cells will stabilise their own excitability to maintain firing rates to prevent hyper- or hypo-excitability, therefore increasing their own intrinsic excitability (Turrigiano and Nelson, 2004). This increased response following tianeptine fits with the protein expression profile documented by Needs *et al*., who reported a 3-fold increase in PSD-95 compared to AMC during SRS. Meaning, it is likely that tianeptine was able to increase lateral diffusion and postsynaptic anchoring of the little available AMPARs, therefore increasing overall network activity.

Accordingly, why would CA3 be unable to increase network activity further with tianeptine when already oscillating in KA during the SRS stage of epileptogenesis? We have hypothesised that CA3 has already hit maximal network excitability in the presence of KA (which is why tianeptine is able to increase network activity in spontaneous conditions), meaning all available AMPARs are occupied and participating in the EPSC. There are two major sources of CA3-specific excitation to pyramidal cells – recurrent synapses and mossy fibre inputs (Le Duigou et al., 2014). This means bath application of 200nM KA will result in a larger excitatory local field output – a consistent observation when comparing peak power between CA1 and CA3.

5.3.3. This excitatory-inhibitory imbalance and the consequence for the transition to SRS

Epilepsy is described as an imbalance of excitation and inhibition (E/I (im)balance). Notably, epilepsy has been associated with an increase in excitation and/or decrease in inhibition, leading to the emergence of hyperexcitability and hypersynchronous seizures (Shao et al., 2019). This results chapter agrees with this observation of increased excitation once animals present with electrographic and clinical seizures, but the receptor and network changes which drive this process prior to the first seizure may be paradoxical to this.

Following the initial precipitating insult, those who have entered epileptogenesis will advance into the seizure-free latent period. As shown throughout this chapter, there are consistent reductions in spontaneous and KA-mediated network excitability which do not recover with acute bath application of 10μM tianeptine. This would assume hippocampal networks are tipped in favour of inhibition, which would explain why seizures are not present during the latent period.

At some point, there is an increase in network excitability as pyramidal cells begin to adjust their intrinsic excitability to homeostatically regulate their firing rate (Turrigiano and Nelson, 2004). This will shift the balance in favour of excitation. As shown in figures 5.4. and 5.6., although CA3 can regain some network excitability and coherence following transition into SRS, there is a limit in network excitability compared to CA1. Conversely, CA1 can readily respond to KAR activation and increase further upon application of tianeptine once in SRS (figure 5.4. and 5.5.). This mismatch in maximal network excitability in CA1 and CA3 may cause reductions in functional connectivity between CA1 and CA3, therefore underlying the generation and foci of seizures and explaining the transition to SRS. *In vitro* and *in vivo* studies of spontaneous epileptiform activity in the hippocampus commonly identifies CA1 as the propagation site (Bikson et al., 2018, Feng and Durand, 2003, Jefferys and Haas, 1982, Shuai et al., 2003, Yaari et al., 1983).

Under normal conditions, rhythmic activity can be generated intrinsically in CA3 which propagates to CA1. The predominant synaptic input to CA1 interneurons was excitatory from CA3 pyramidal cells, meaning CA3 pyramidal cells rhythmically recruit CA1 interneurons. The firing of local CA1 pyramidal cells is controlled by their connected interneurons by feedforward inhibition. Phase-coupling of CA1 pyramidal cells shows a dominance of inhibition over excitation, meaning this feedforward inhibition is what drive rhythmogenesis in CA1 (Zemankovics et al., 2013). Hypothetically, loss of this excitatory drive from CA3 pyramidal cells to CA1 interneurons would remove this inhibitory drive to local CA1 pyramidal cells, possibly leading to the emergence of hyperexcitability and hypersynchronous seizures.

Future work should look to explore this reduced protein expression and postsynaptic localisation of AMPARs even during the SRS stage of epileptogenesis and explore if modified

AMPAR protein expression during the latent period normalised the excitatory-inhibitory imbalance. Furthermore, more work exploring the functional connectivity of CA1-CA3 throughout epileptogenesis should be conducted, particularly as animals begin transition into electrographic and behavioural seizures.

Chapter 6 Seizure-like activity *in vitro*

6.1. Introduction

So far, chapters 3 – 5 have studied the local field and synaptic neuronal activity changes which occur throughout the progression of epileptogenesis. Consistently, there are reductions in local field and synaptic excitability during the latent period which recover once animals enter the SRS stage of epileptogenesis, despite now displaying the seizure phenotype. Another option for assessing brain slice excitability is to study acute seizure-like activity *in vitro*. There are various methods used to study SLA *in vitro* which involves either modification of the slice environment to promote a hyperactive, pro-convulsive state (e.g., 0 Mg^{2+} aCSF, high K^{+} aCSF) or bath application of a pro-convulsant (e.g., 4-aminopyridine, kainic acid). Acute seizure models allow us to study seizure development and progression, and the effects of anti-epileptic drugs (e.g. carbamazepine, valproate) (Zhang et al., 1995).

6.1.1. 0 Mg^{2+} model of acute seizures

Magnesium-free medium has been used to induce SLA in hippocampal slices for several decades now (Anderson et al., 1986, Walther et al., 1986). This *in vitro* model of acute seizures has clinical relevance in humans as deficits in Mg^{2+} can increase seizure susceptibility (Arnold et al., 1983, Nuytten et al., 1991) and Mg^{2+} injections are effective in treating seizures associated with eclampsia (Duley et al., 2010). The mechanisms by which a reduction in Mg^{2+} can induce SLA involves facilitation of NMDARs by neuronal depolarisation and decreased surface charge screening near voltage-gated ion channels leading to a hyperpolarising shift (Isaev et al., 2012). This leads to increased excitability and initiation of SLA.

At resting membrane potentials, a voltage-dependent block by Mg^{2+} prevents current flow through NMDARs. Only significant depolarisation via other ionotropic glutamatergic receptors (e.g., AMPARs) allows for relief from this Mg^{2+} block, and entry of Ca^{2+} and Na^{+} can occur through NMDARs (Nikolaev et al., 2012). In the presence of Mg^{2+}, it is difficult to evoke NMDAR EPSCs at membrane potentials close to rest (-60 mV), however, upon depolarisation-induced relief of the Mg^{2+} at depolarised potentials, NMDAR currents are easily evoked. Indeed, protocols in which the neuronal membrane is held at +20 mV to reveal 'silent' NMDAR are widely used. In contrast, in absence of Mg^{2+}, NMDARs can evoke EPSCs at all depolarising voltages. This reflects the voltage-sensitivity of NMDARs in the presence of Mg^{2+} (Mayer et al., 1984). As such, removal of bath Mg^{2+} will lead to increased activation of NMDARs and influx of Na^{+} and Ca^{2+}, therefore resulting in increased postsynaptic activation and the possible development of SLA (Malenka and Nicoll, 1999). Equally, investigation of SLA generated by Mg^{2+}-medium *in vitro* found replacement of depleted Mg^{2+} with Ca^{2+} did result in a slight decrease in the amplitude of SLA but not complete abolition, suggesting other factors (e.g., surface charge screening) are also involved in the mechanism by which Mg^{2+} modulates hyperactivity via NMDARs (Jones and Heinemann, 1988).

Another proposed mechanism for the generation of SLA following removal of Mg^{2+} is decreased surface charge screening. Under physiological conditions, a negative local electrical field is generated by the cell membrane (e.g., by sialic acid, phosphates, charged lipids and negatively charged amino acids). This negative cell surface attracts a layer of positive ions (Stern layer). As positive ions are large, the cell surface charge is not completely neutralised so more positive ions (with a few negative ions) are attracted (Gouy-Chapman layer). Two types of electrostatic interactions can occur – (1) at the cell surface, positive ions will bind to the cell surface when hydration has been removed and become immobile, and (2) more distal, hydrated positive ions can screen the cell surface and repel opposing charges, remaining mobile and unbound. Removal of bath Mg^{2+} leads to alterations in the Stern and Gouy-Chapman layers and reduced screening/shielding of the membrane. This can shift the voltage dependences of voltage-gated ion channels towards hyperpolarised potentials, leading to increased ion channel activation and the generation of SLA (Bara et al., 1989, Isaev et al., 2012).

To study brain slice excitability via seizure susceptibility using the *in vitro* 0 Mg^{2+} model of acute seizure, *ex vivo* extraction of AMC and RISE animals were taken at the same timepoints as above to explore the latent period (weeks 2, 3, 4, 5, and 6 post-induction) and the SRS stage of epileptogenesis (>3 months). Slices were placed onto the rigs and were recorded in normal aCSF for 30 minutes to examine 'baseline' activity. This was then switched to the Mg^{2+}-free aCSF for 3 hours. Several parameters were measured to explore seizure susceptibility over those 3 hours: (1) percentage of slices to seize overall, (2) time to first seizure (seconds), (3) total number of seizures (count), (4) duration of seizures (seconds) and (5) inter-seizure interval (ISI, seconds).

6.2. Results

6.2.1. Typical seizure generation in the hippocampus

Horizontal hippocampal-entorhinal slices were prepared from AMC and RISE-induced rats during timepoints for the latent period (weeks 2, 3, 4, 5, and 6 post-induction) and SRS (>3 months post-induction) using the standard LFP method (chapter 2.5.). As mentioned above, slices were placed onto the rigs and were recorded in normal aCSF for 30 minutes to examine 'baseline' activity. This was then switched to the Mg^{2+}-free aCSF for 3 hours. Several parameters were measured to explore seizure susceptibility over those 3 hours: (1) percentage of slices to seize overall, (2) time to first seizure (seconds), (3) total number of seizures (count), (4) duration of seizures (seconds) and (5) inter-seizure interval (ISI, seconds).

Figure 6.1. shows an example of a single typical looking seizure generated in 0 Mg^{2+} conditions in CA1 of a RISE animal in the SRS stage of epileptogenesis. Repetitive high frequency, high power bursting activity of ≥10 seconds is seen initially ('seizure') which terminates into a period

of post-ictal depression (PID). Most seizures showed a hypersynchronous onset with a few pre-ictal spikes. This follows a period of lower frequency discharging after revival of neuronal activity ('post-ictal spiking', PIS) back to baseline. Although common, PIS was not always present after seizures.

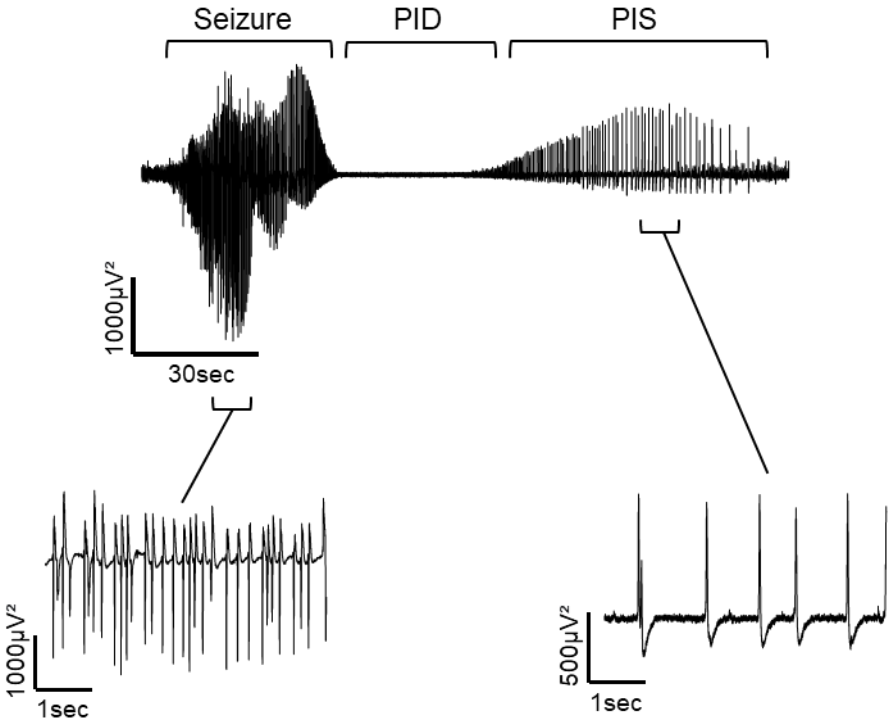

Figure 6.1. An example of a single seizure in CA1 *in vitro*.

An example of a typical single seizure generated in CA1 of a RISE animal in the SRS stage of epileptogenesis. Periods of post-ictal depression (PID) and post-ictal spiking (PIS) also shown. Expansion of the seizure and PIS shown below.

6.2.2. AMC vs RISE – seizure susceptibility using the *in vitro* 0 Mg^{2+} model of epilepsy

The first parameter studied was the total percentage of brain slices to have a minimum of one seizure during the 3 hours in 0 Mg^{2+}. Figure 6.2. A shows the combined percentages across all timepoints studied for the latent period (weeks 2, 3, 4, 5, and 6) and the SRS stage of epileptogenesis. For AMC, there was a combined 36.7 ± 2.5% (n = 6) slices which displayed at least one seizure while in 0 Mg^{2+} compared to 59.4 ± 3.9% for RISE animals (n = 6, $p \leq 0.01$). A week-by-week break down can be seen in figure 6.2. B, with AMC showing a range in percentages of slices showing seizures between 25.0% - 41.7%. Consistently for each week, RISE animals showed increased percentages of slices which developed into seizures following removal of Mg^{2+}. Interestingly, there seems to be a decrease in seizure susceptibility as the latent period progresses, with week 2 showing 65.0% of slices to seize which decreased to 42.3% at 6 weeks post-induction. This increased again to 66.7% as animals entered the SRS

stage of epileptogenesis. This shows that following removal of Mg^{2+}, RISE animals were more likely to develop seizures *in vitro* and even showed a slight resistance to seizure generation as the latent period progresses.

A

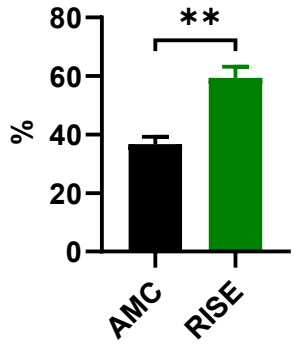

B

Week	AMC	RISE
2	41.7%	65.0%
3	42.0%	60.0%
4	37.5%	66.7%
5	38.0%	55.6%
6	25.0%	42.3%
SRS	36.0%	66.7%

Figure 6.2. Percentages of slices to seize for AMC and RISE.

(A) A bar chart showing the combined percentages of slices to seize following removal of Mg^{2+} *in vitro* for AMC (black) and RISE (green) across all timepoints studied. (B) Week-by-week breakdown of percentages of slices to seize following removal of Mg^{2+} *in vitro* for AMC and RISE. Error bars show SEM. ** denotes $p \leq 0.01$ (Mann-Whitney test).

The next parameter studied was time to first seizure. This was calculated by measuring the time between bath application of the 0 Mg^{2+} aCSF to the generation of the first seizure. Figure 6.3. shows the week-by-week time course for both AMC to RISE. In the early stages of the latent period, the time to first seizure for RISE is shorter than AMC. At 2 weeks, time to first seizure was 4168.0 ± 462.5 s (n = 24) for RISE and 6624.0 ± 837.8 s (n = 9, $p \leq 0.05$) for AMC. Although non-significant, this trend continues into week 3 (AMC: 6469.0 ± 1075.0 s, n = 9; RISE: 5610.0 ± 704.6 s, n = 12, p = ns). By 4 weeks, time to first seizure was 6220.0 ± 389.5 s (n = 29) for RISE and 8487.0 ± 183.7 s (n = 5, $p \leq 0.05$) for AMC. By week 5, it appears AMC and RISE have almost identical time to first seizure (AMC: 7478.0 ± 458.3 s, n = 6; RISE: 7802.0 ± 501.3, n = 20, p = ns) meaning seizure susceptibility in RISE animals in the latent period is like that of AMC. As RISE animals enter the SRS stage of epileptogenesis, we see a large difference in the time to first seizure. For RISE animals, time to first seizure is 3930.0 ± 546.1 s (n = 15) compared to 8284.0 ± 491.1 s (n = 10, $p \leq 0.001$) for AMC. This means RISE animals can generate SLA in 0 Mg^{2+} conditions much faster than AMC.

Following the trend of RISE, it is clear there is an increase in time to first seizure as the latent period progresses which decreases again as animals enter SRS. This likely also reflects the reduction of SLA seen in the latent period.

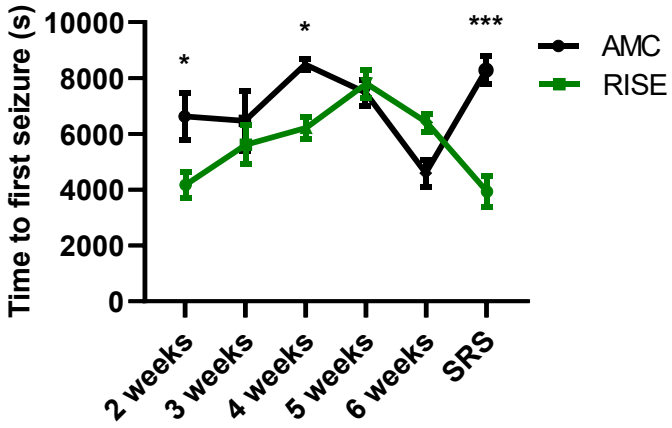

Figure 6.3. Time to first seizure for AMC and RISE.

Connected column mean graph showing time to first seizure (s) for AMC (black) and RISE (green) in 0 Mg^{2+} conditions. Error bars show SEM. * denotes $p \leq 0.05$ and *** denotes $p \leq 0.001$ (Mann-Whitney test).

The next parameters studied were the total number (count) and duration of seizures following removal of Mg^{2+} for 3 hours. Figure 6.4. shows both seizure count (figure 6.4. A) and duration of seizures (figure 6.4. Bi, Bii). For total seizure count, a clear trend forms for RISE animals with a decreasing total number of seizures in 0 Mg^{2+} at the latent period progresses which appears to increase as animals enter the SRS stage of epileptogenesis. A significant difference in total number of seizures is only present during SRS, with AMC averaging 1.6 ± 0.3 seizures (n = 10) during the 3 hours in 0 Mg^{2+} compared to 6.5 ± 1.1 seizures (n = 15, $p \leq 0.01$) for RISE animals. This shows the increased seizure susceptibility demonstrated by RISE animals in 0 Mg^{2+} conditions while in the SRS stage of epileptogenesis.

For seizure duration, the length of seizures displayed in 0 Mg^{2+} is very consistent in AMC throughout all timepoints studied. This differs from RISE, with seizure duration being longest during the early stages of the latent period which decreases to a similar duration to AMC by week 4. From week 5, RISE animals display a stable duration of seizure length. As shown in figure 6.4. Bi, at 2 weeks, seizure duration in 0 Mg^{2+} conditions averages 58.6 ± 7.8 s (n = 24) for RISE animals and 14.8 ± 1.4 s (n = 10, $p \leq 0.001$) for AMC. At 3 weeks, seizure duration for RISE animals is 41.0 ± 9.0 s (n = 12) compared to 15.6 ± 2.7 s (n = 9, $p \leq 0.05$) for AMC. Interestingly, by 4 weeks post-induction, there appears to be little difference in seizure duration

between AMC and RISE (AMC: 17.1 ± 2.9 s, n = 5; RISE: 19.0 ± 1.9 s, n = 29, p = ns). However, by 5 weeks post-induction, seizure duration in 0 Mg^{2+} conditions averages 30.3 ± 3.5 s (n = 19) for RISE animals and 16.6 ± 1.7 s (n = 6, $p \leq 0.05$) for AMC. At 6 weeks post-induction, seizure duration for RISE animals is 32.2 ± 7.7 s (n = 19) compared to 13.2 ± 1.0 s (n = 28, $p \leq 0.05$) for AMC. Finally, during SRS, seizure duration for RISE animals is 31.4 ± 3.5 s (n = 15) compared to 12.7 ± 2.0 s (n = 10, $p \leq 0.001$) for AMC. A comprehensive week-by-week breakdown of seizure duration is also shown in figure 6.4. Bii.

Overall, this shows that following removal of Mg^{2+}, both total seizure count and seizure duration follow a trend of decreases as the latent period progresses before large increases in both count and duration once RISE animals enter the SRS stage of epileptogenesis.

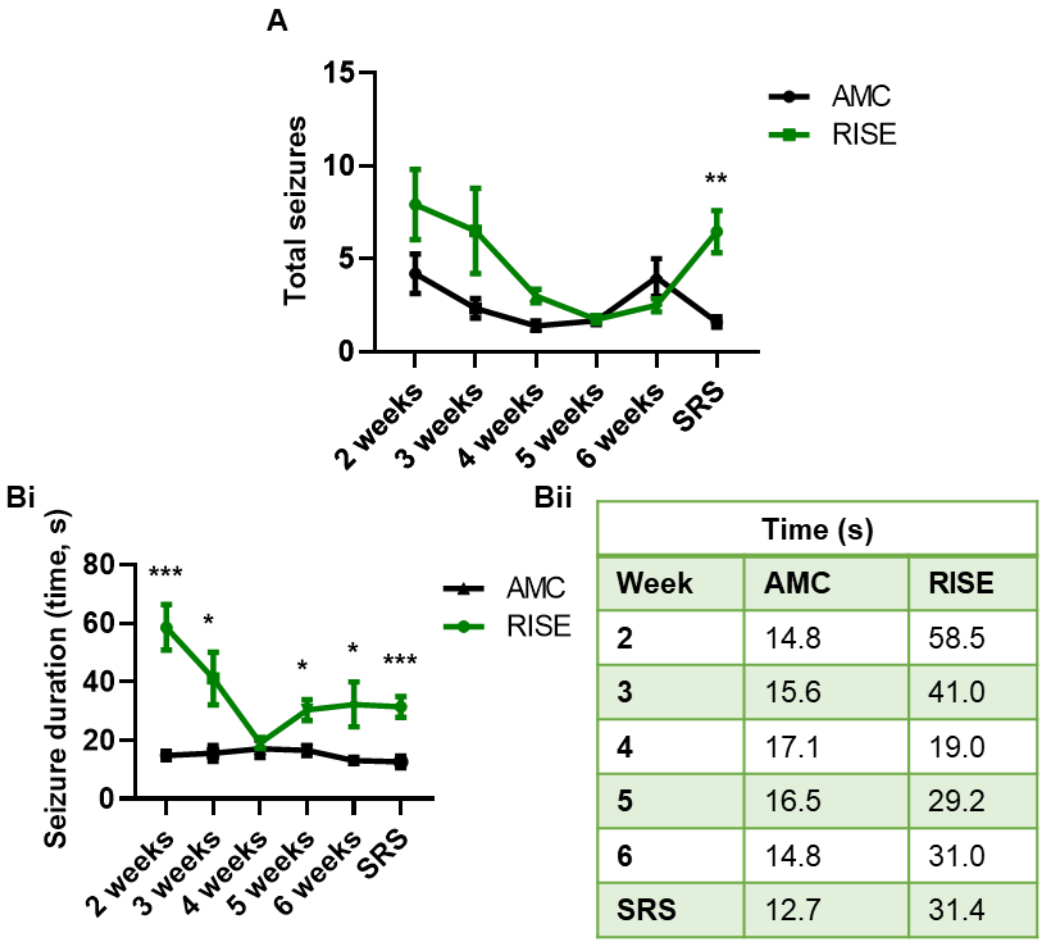

Time (s)		
Week	**AMC**	**RISE**
2	14.8	58.5
3	15.6	41.0
4	17.1	19.0
5	16.5	29.2
6	14.8	31.0
SRS	12.7	31.4

Figure 6.4. Total seizure count and seizure duration for AMC and RISE.

(A) Connected column mean graph showing total number of seizures (count) during the 3 hours following removal of Mg^{2+} throughout the latent period and SRS. (Bi) Connected column mean graph showing seizure duration during the 3 hours following removal of Mg^{2+} throughout the latent period and SRS. (Bii) Table with the week-by-week breakdown of seizure duration for AMC and RISE. Black lines indicate AMC and green lines indicate RISE. Error bars show SEM. * denotes $p \leq 0.05$, ** denotes $p \leq 0.01$ and *** denotes $p \leq 0.001$ (Mann-Whitney test).

The final parameter studied was inter-seizure interval (ISI). This was defined as the time between each seizure event, meaning ISI was only possible if at least two seizures were present over the 3 hours in 0 Mg^{2+}. Due to the lack of seizures at weeks 4 and 5 for AMC animals, ISI was not possible. Figure 6.5. A shows the ISI for RISE animals only. The shortest ISI was 2 weeks post-SE, with RISE animals averaging 304.6 ± 30.5 s (n = 88). The longest ISI was 5 weeks post-SE, with RISE animals averaging 2641.0 ± 467.4 s (n = 8). By SRS, ISI had decreased slightly to 1001.0 ± 77.1 s (n = 35). Figure 6.5. B shows the combined ISI across all timepoints studied for AMC and RISE (minus weeks 4 and 5 AMC). Significantly, when in 0 Mg^{2+}, AMC displayed a longer ISI (1110.0 ± 63.7 s, n = 66) than RISE animals (854.0 ± 54.8 s, n = 209, $p \leq 0.001$), indicating that RISE animals displayed increased susceptibility to generating seizures which reduced time in between.

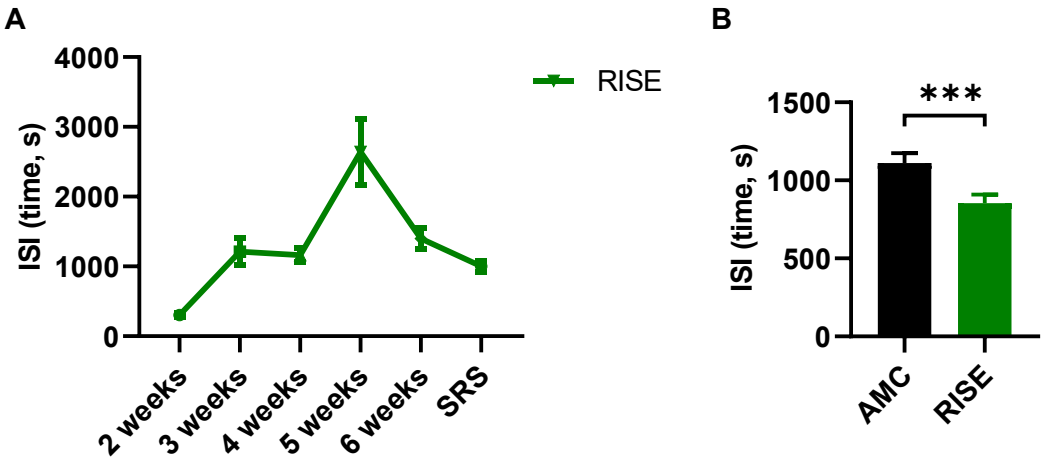

Figure 6.5. Inter-seizure interval for AMC and RISE.

(A) Connected column mean graph showing ISI following removal of Mg^{2+} throughout the latent period and SRS for RISE animals only. (B) A bar chart showing combined ISI values for AMC (black) and RISE (green) following removal of Mg^{2+}. Error bars show SEM. *** denotes $p \leq 0.001$ (Mann-Whitney test).

6.2.3. Seizure initiation zone

An interesting and consistent phenomenon observed was the region of seizure initiation within the hippocampus. This was easily identifiable as seizures would often begin in one region before appearing in the other hippocampal subregion with a short delay of several milliseconds. Typically, hippocampal seizures would begin in the CA1 subregion before appearing in CA3. This is demonstrated in figure 6.6. which shows the percentages of brain slices with CA1 as the seizure initiator region. Studying all timepoints across the latent period and SRS combined, CA1 was the seizure initiator region in 79.8 ± 6.1% of brain slices in AMC and 66.0 ± 5.8% in RISE animals (p = ns). A week-by-week breakdown is shown in figure 6.6.

B. This shows that following removal of Mg^{2+}, seizures would typically begin in CA1 before arising in CA3 in both AMC and RISE animals.

A

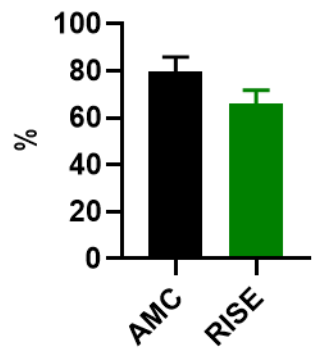

B

Week	AMC	RISE
2	92%	83%
3	80%	50%
4	67%	69%
5	100%	80%
6	80%	64%
SRS	60%	50%

Figure 6.6. Seizure initiation percentages in CA1.

(A) A bar chart showing combined percentages of CA1 as the seizure initiator region in the hippocampus for AMC (black) and RISE (green) following removal of Mg^{2+} throughout the latent period and SRS. (B) A table showing the week-by-week breakdown of these percentages. Error bars show SEM.

6.2.4. Comparing seizure susceptibility between the latent period and SRS stage of epileptogenesis

Finally, seizure susceptibility was studied between the latent period (week 6 post-induction) and the SRS stage of epileptogenesis to assess the differences as RISE animals transition from the seizure-free latent period to presenting with clinical seizures. Like above, time to first seizure, total number of seizures (count), seizure duration and ISI were explored over the 3 hours following removal of Mg^{2+}.

Figure 6.7. A shows the time to first seizure between 6 weeks post-induction and SRS. At 6 weeks, RISE animals display a time to first seizure of 6407.0 ± 326.1 s (n = 20) compared to 3930.0 ± 546.1 s (n = 15, $p \leq 0.001$) once animals enter SRS. This shows seizure susceptibility is reduced during the latent period as it takes much longer for brain slices to produce SLA in 0 Mg^{2+} conditions than during SRS.

Figure 6.7. B shows total seizure count between 6 weeks post-induction and SRS. At 6 weeks, RISE animals produce 2.5 ± 0.4 (n = 20) total seizures during 3 hours in 0 Mg^{2+} compared to 6.5 ± 1.1 (n = 15, $p \leq 0.01$) once animals enter SRS. This shows seizure susceptibility is much higher once animals enter the SRS stage of epileptogenesis, meaning there is resistance to producing SLA during the latent period.

Figure 6.7. C shows seizure duration between 6 weeks post-induction and SRS. At 6 weeks, RISE animals generated seizures lasting 31.0 ± 7.4 s (n = 20) which were similar duration to

SRS at 31.4 ± 3.5 s (n = 15, p = ns). This shows seizure duration following removal of Mg^{2+} did not change as animals progresses from the latent period into the SRS stage of epileptogenesis.

Finally, figure 6.7. D shows the ISI between 6 weeks post-induction and SRS. At 6 weeks, RISE animals showed an ISI of 1399.0 ± 148.9 s (n = 16) during 3 hours in 0 Mg^{2+} compared to 1001.0 ± 77.1 s (n = 35, $p \leq 0.01$) once animals enter SRS. This shows that following removal of Mg^{2+}, the latency between each seizure event is larger during the latent period than during SRS, meaning seizure susceptibility is increased during the SRS stage of epileptogenesis.

Overall, this fits with the idea that the latent period has reduced susceptibility to generating seizures and SLA. As animals progress into SRS, seizure susceptibility is massively increased in terms of total count and frequency of seizures. However, it appears there is no change in seizure duration which stays consistent regardless of timepoint within epileptogenesis.

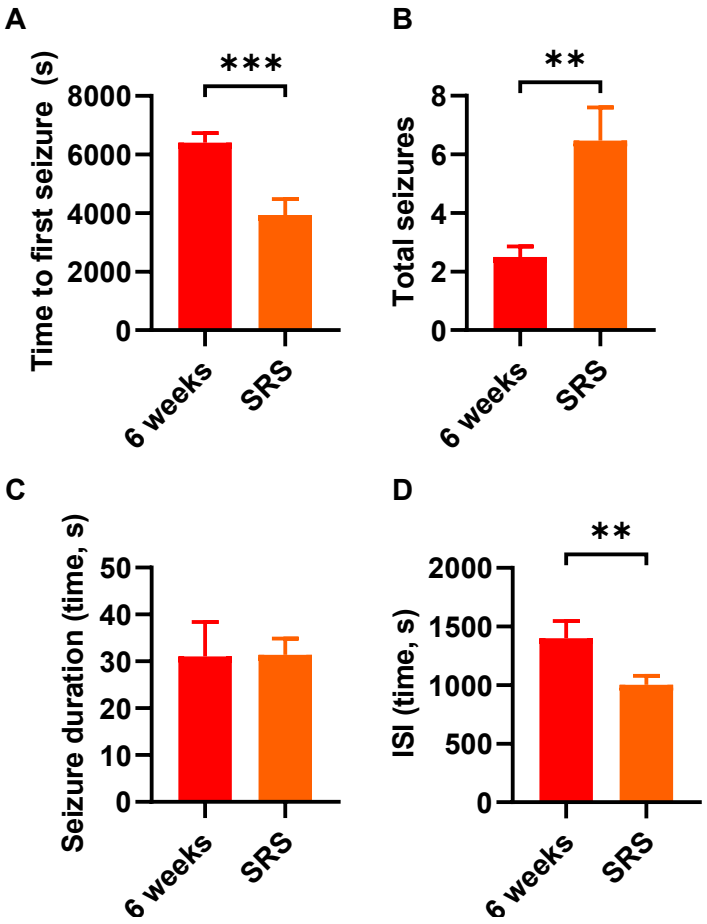

Figure 6.7. Comparing seizure susceptibility between 6 weeks post-induction and SRS in slices from RISE animals.

Bar graphs comparing seizure susceptibility following 3 hours in 0 Mg^{2+} conditions for week 6 post-induction (red) and the SRS stage of epileptogenesis (orange). (A) time to first seizure (s), (B) total seizure count, (C) seizure duration (s), and (D) inter-seizure interval (ISI, s). Error bars show SEM. ** denotes $p \leq 0.01$ and *** denotes $p \leq 0.001$ (Mann-Whitney test).

To conclude, studying seizure susceptibility using the 0 Mg^{2+} model of epilepsy has shown that seizure susceptibility in RISE animals is hugely increased in comparison to AMC. It appears

there is reduced seizure susceptibility in RISE animals during the latent period which increases again as animals enter the SRS stage of epileptogenesis. Finally, it is possible that the CA1 subregion is the seizure initiator within the hippocampus.

6.3. Discussion

Chapter 6 demonstrates increased experimental seizure susceptibility using the *in vitro* 0 Mg^{2+} model of epilepsy across several measures when animals have already entered epileptogenesis using the RISE model of epilepsy compared to controls. There is also an interesting pattern of decreased seizure susceptibility during the latent period which represents the altered network, synaptic and cellular changes which result in this seizure-free phase.

One limitation of this chapter is the lack of effective AED testing. One advantage of using the *in vitro* 0 Mg^{2+} model of epilepsy is to study the effect of AED following seizure induction. Given the above work in chapters 4 and 5 studying tianeptine and its effect on oscillations throughout epileptogenesis (anti- epileptogenic drug), work was began studying tianeptine as an AED. However, due to time constraints, not enough data was gathered for presentation in this thesis. As such, there is hope that work will continue to give a better idea of the potential therapeutic role tianeptine could play in the treatment of epileptic seizures.

6.3.1. Increased seizure susceptibility following RISE induction

Previous studies examining the susceptibility to pro-convulsants following induction of epileptogenesis have found different results regarding seizure susceptibility. Blanco *et al.* induced epileptogenesis using the lithium-pilocarpine method. One month later, Wistar rats were given an AED (e.g., phenytoin, phenobarbital or valproic acid) and then subjected to a pro-convulsive state (either using pentylenetetrazol, PTZ, or maximal electroshock, MES). The authors found pre-treatment with an AED was effective in preventing seizure induction in the group subjected to MES, however this was not the case for PTZ. Only control animals had seizure control when given PTZ, and seizure severity was increased in the epileptic (lithium-pilocarpine) group. Meaning, initiation of epileptogenesis puts the brain in a state of vulnerability to seizure induction (Blanco et al., 2009). PTZ treatment in genetically epilepsy-prone rats (GEPRs) also found shorter latency and greater seizure severity to tonic seizure induction compared to control animals (Browning et al., 1990).

Conversely, Nehlig *et al.* found epileptogenesis initiated by lithium-pilocarpine at P10 does not affect long-term susceptibility to seizures. PTZ, picrotoxin and kainic acid were used to promote a convulsive state once animals were in adulthood, however the authors found induction of epileptogenesis using the lithium-pilocarpine method does not lead to spontaneous seizures and did not increase the sensitivity to convulsants at adulthood. However, this is likely due to age of induction as P10 rats were used. Meaning, induction of epileptogenesis in the immature

brain will affect the trajectory of epileptogenesis and resulting reduced susceptibility to seizures (Nehlig et al., 2002).

Interestingly, Zhang *et al.* also conducted similar experiments by inducing epileptogenesis using the lithium-pilocarpine method on P10 rats and found prolonged SE does not lead to the development of SRS during adulthood. However, the authors did report increased susceptibility to KA-induced seizures following induction. The differing results between these two studies is likely due to methodological differences (e.g., brain region studied, or administration route of kainic acid) (Zhang et al., 2004).

Interestingly for this thesis, Zhang *et al.* hypothesises that a specific loss of the AMPAR subunit GluA2 in hippocampal dentate granule cells of adult animals who experienced prolonged SE at P10 may cause an increase in calcium influx and higher channel conductance leading to greater susceptibility to KA-induced seizures in adulthood (Zhang et al., 2004). Sanchez *et al.* also found increased seizure susceptibility into adulthood and decreased GluA2 subunit expression in CA1 following global hypoxia-induced epileptogenesis (Sanchez et al., 2001). Similarly, reduced seizure thresholds to chemical convulsants and electrical stimulation was also present in a study exploring febrile seizures in rats (Dube et al., 2000).

Overall, these studies explain how initiation of epileptogenesis, regardless of aetiology, will likely lead to increased susceptibility to seizure induction which fits with the above work in this chapter. However, this is dependent upon on the pro-convulsive methods adopted, with some being more likely than others to induce a seizure state.

6.3.2. Seizure initiation zones

An interesting phenomenon observed was the hippocampal subregion in which seizures would arise from. Commonly, particularly during the early stages of epileptogenesis, this appeared to be CA1. Other studied have also found similar results when using the 0 Mg^{2+} model of epilepsy. Isaev *et al.* found removal of Mg^{2+} resulted in SLA in the hippocampal CA1 subregion in 67% of slices (Isaev et al., 2012). Furthermore, Lewis *et al*. found seizures originated in CA1 which would spread and invade CA3, but interictal bursts originated in CA3 which would propagate to CA1 and were found to have a suppressant effect on seizures within CA1 (Lewis et al., 1990)

Rates of seizure induction within CA1 did decrease once RISE animals had reached the SRS stage of epileptogenesis, however these were still ~50% (figure 6.6. B). Modebadze *et al.* studied the RISE model and found the seizure initiation region to be the medial entorhinal cortex following development of SRS. However, the authors note that given the reduced nature of the slice preparation, it is difficult to make robust statements concerning the location of the primary epileptogenic zone, though, it is possible that the zone of seizure initiation may not be stable during epileptogenesis (Modebadze et al., 2016).

Codadu *et al.* also argues epileptiform activity begins in neocortical and entorhinal networks before invading the hippocampus. However, the hippocampus then acts as a pacemaker, entraining other brain regions to their discharge pattern (Codadu et al., 2019). As this work only explored epileptiform activity within the hippocampus, it is difficult to conclude the exact seizure initiation region. As mentioned, it is possible that this changes as epileptogenesis develops. Future work should consider conducting dual recordings of the hippocampus and entorhinal cortex to examine the primary epileptogenic zone(s) and patterns of epileptiform activity within the temporal lobe.

Chapter 7 A potential *in vitro* model of epileptogenesis

7.1. Introduction

Animal models of disease have been vital in aiding researchers to investigation disease process' and investigate potential therapeutics (pre-clinical). However, a disadvantage of animal models, such as the RISE model of epilepsy, is the chronic nature of the model. Meaning it often takes weeks or even months before any data is available. An acute, *in vitro* model was developed for studying the receptor movement which aims to mimic the receptor changes believed to occur as epileptogenesis progresses in the RISE model. This would allow us to study epileptogenesis on an acute scale which may enable more rapid screening of potential therapeutics.

The RISE model of epilepsy hypothesises epileptogenesis is driven by a chronic loss of AMPAR neurotransmission (Needs et al., 2019). On an acute scale, AMPAR internalisation can be triggered by bath application of AMPAR agonist s-AMPA. *In vitro* LFP experiments were conducted on horizontal hippocampal-entorhinal slices prepared from control Wistar rats (100 – 130g) using the standard LFP method (chapter 2.5.). To begin with, gamma oscillations were generated by bath applying 200nM KA ('control') for 30 minutes. Following stabilisation of this KA-induced gamma band activity, 50μM D-AP5 was added block to NMDARs and prevent NMDAR-dependent LTP. After 30 minutes, 10μM corticosterone was added to prime excitatory synapses for synaptic potentiation (Mikasova et al., 2017). 30 minutes later 1μM s-AMPA is added to induce AMPAR internalisation, and the slices were allowed to sit in this AMPAR agonism for at least one hour. This s-AMPA mediated AMPAR internalisation was a rapid process, with a substantial collapse in the gamma band activity within 3 minutes. Following 1 hour of s-AMPA mediated AMPAR internalisation, a fresh cylinder of aCSF with 200nM KA and 50μM D-AP5 was recirculated ('wash') for 30 min, before 10μM tianeptine was bath applied for a final 30 minutes to re-insert those internalised AMPARs. Manipulation of receptor trafficking in this manner was used to mimic an acute version of the RISE model of epilepsy, with tianeptine used as the therapeutic drug of potential.

7.2. Results

Figures 7.1. – 7.4. show the *in vitro* receptor shuttling experiments conducted to mimic an acute version of the RISE model of epilepsy with tianeptine used as the therapeutic drug of potential. Figure 7.1. shows the time course of an example experiment in hippocampal subregions CA1 (figure 7.1. A) and CA3 (figure 7.1. B). Following bath application of D-AP5 and corticosterone, there were small increases in hippocampal power in both CA1 and CA3. Overall power is completely diminished following application of s-AMPA. There was little recovery in the oscillation once the wash is applied. However, following application of tianeptine, there was recovery of the oscillation back to control (pre-s-AMPA) levels).

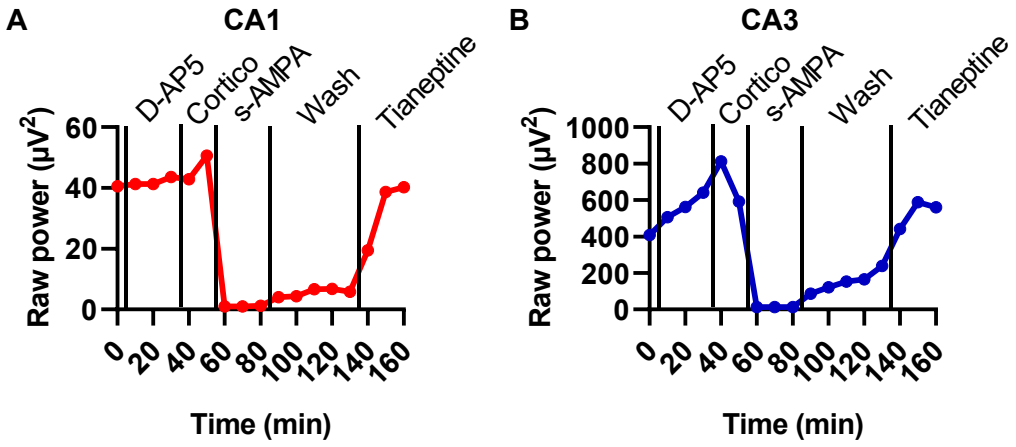

Figure 7.1. Example receptor shuttling (AMPAR internalisation) experiments in CA1 and CA3.

Time course experiments examining AMPAR internalisation and recovery with 10μM tianeptine. Baseline oscillations were generated with 200nM KA, then bath application of the following drugs: 50μM D-AP5 > 10μM corticosterone > 1μM s-AMPA > wash (new cylinder of aCSF with 200nM KA and 50μD-AP5) > 10μM tianeptine. (A) CA1 (red), (B) CA3 (blue).

Further analysis of this can be seen in figure 7.2. Percentage change was calculated and plotted similar to figure 7.1.. Most notably, the timescale aims to demonstrate the rapid loss of power following application of s-AMPA (approximately 3 minutes). Figure 7.2. B shows the percentage increase following tianeptine application after the slices had been washed with a new cylinder of aCSF. There were no significant difference in the increase in power between CA1 and CA3, with CA1 increasing by 966.8 ± 331.5% (n = 7) following bath application of tianeptine, and CA3 increasing by 772.8 ± 218.7% (n = 10). This shows that despite loss of AMPAR neurotransmission, tianeptine was able to substantially increase the raw power of gamma oscillations in the hippocampus.

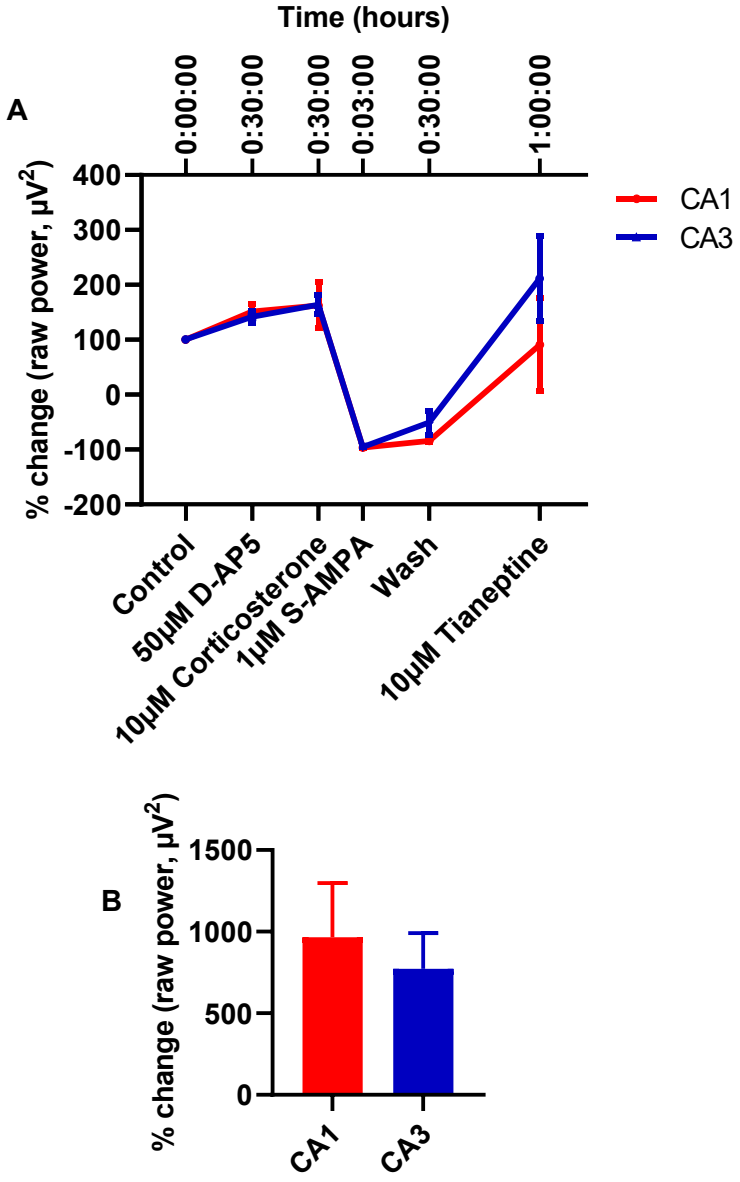

Figure 7.2. Percentage changes throughout the receptor shuttling experiment

(A) Time course following the percentage changes of raw power following bath application of each drug used to track receptor shuttling changes (KA, D-AP5, corticosterone, s-AMPA, and tianeptine). Percentage changes were calculated from control. The time course is representative of full drug effect. (B) Percentage increase between 'wash' and 'tianeptine' for CA1 and CA3. Red indicates CA1 and blue indicates CA3. Error bars show SEM.

Finally, a deeper analysis of the change in raw power and frequency of CA1 and CA3 can be found in figure 7.3. and figure 7.4., respectively. An example FFT for CA1 is shown in figure 7.3. Ai demonstrating the diminished oscillations following application of s-AMPA. Little revival was seen in the wash period, with a much faster oscillation produced. Following application of tianeptine, a much more robust gamma oscillation is produced with a more defined peak ~30 Hz. Raw power analysis is seen in figure 7.3. B, with s-AMPA producing a peak gamma oscillation of 9.2 + 7.3 μV^2 (n = 7). A small increase during the wash period produces a peak gamma oscillation of 12.2 + 3.3 μV^2 (n = 7). However, following bath application of tianeptine, there was a substantial increase in the peak gamma power to 158.0 + 79.4 μV^2 (n = 7). A significant difference between peak power for s-AMPA and tianeptine is shown ($p \leq 0.01$). Finally, analysis of the peak gamma frequency (figure 7.3. C) throughout each drug application reveals an interesting spike in frequency following application of s-AMPA to 49.6 + 1.8 Hz (n = 7).

Similarly, an example FFT for CA3 is shown in figure 7.4. Ai. Again, diminished oscillations are seen following application of s-AMPA with little recovery into the wash period. Application of tianeptine produced a coherent, large gamma oscillation. Raw power analysis shows an increase in power from 61.6 + 27.0 μV^2 in s-AMPA, to 412.5 + 27.0 μV^2 during the wash, and finally to 2320.0 + 857.5 μV^2 (n = 10) following application of tianeptine. A significant difference between peak power for s-AMPA and tianeptine is shown ($p \leq 0.001$). Finally, as seen in CA1, analysis of the peak gamma frequency (figure 7.4. C) throughout each drug application reveals an interesting spike following application of s-AMPA to 46.6 + 2.9 Hz (n = 10). Recovery to gamma frequency of control is seen following application of tianeptine (33.5 + 0.8 Hz for control compared to 33.2 + 0.7 Hz for tianeptine).

Overall, this *in vitro* model of the receptor shuttling may be useful as an acute model for studying epileptogenesis, with the potential to test target drugs in the treatment of TLE.

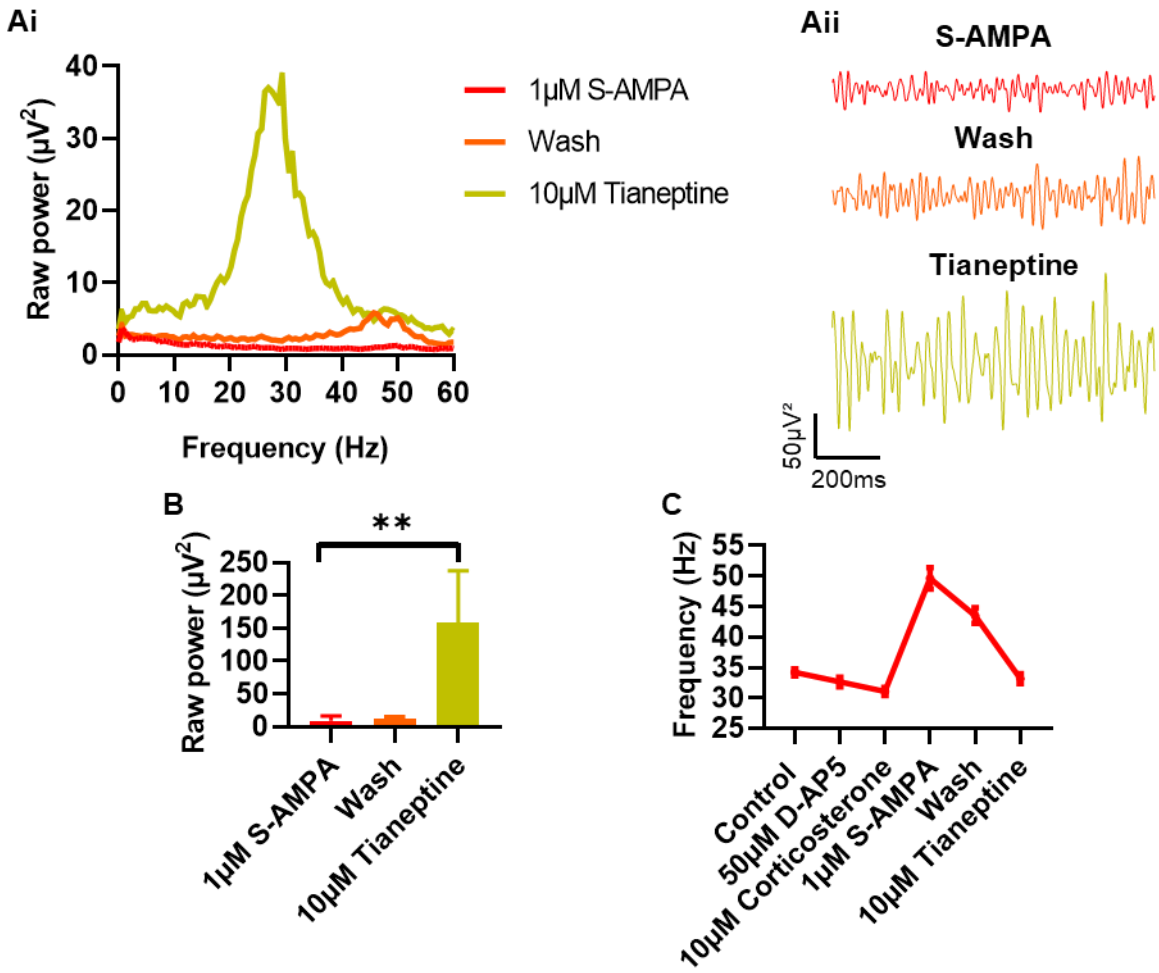

Figure 7.3. Receptor shuttling (AMPAR internalisation) in CA1.

(Ai) Example FFT showing peak gamma oscillations in s-AMPA, wash and tianeptine conditions. (Aii) Corresponding raw traces in each condition. (B) Bar chart of peak raw power in each condition. (C) Before-and-after graph of peak gamma frequency in each condition throughout the full experiment. Red indicates s-AMPA, orange indicates wash and yellow indicates tianeptine. Error bars show SEM. ** denotes $p \leq 0.01$ (Friedman one-way ANOVA test).

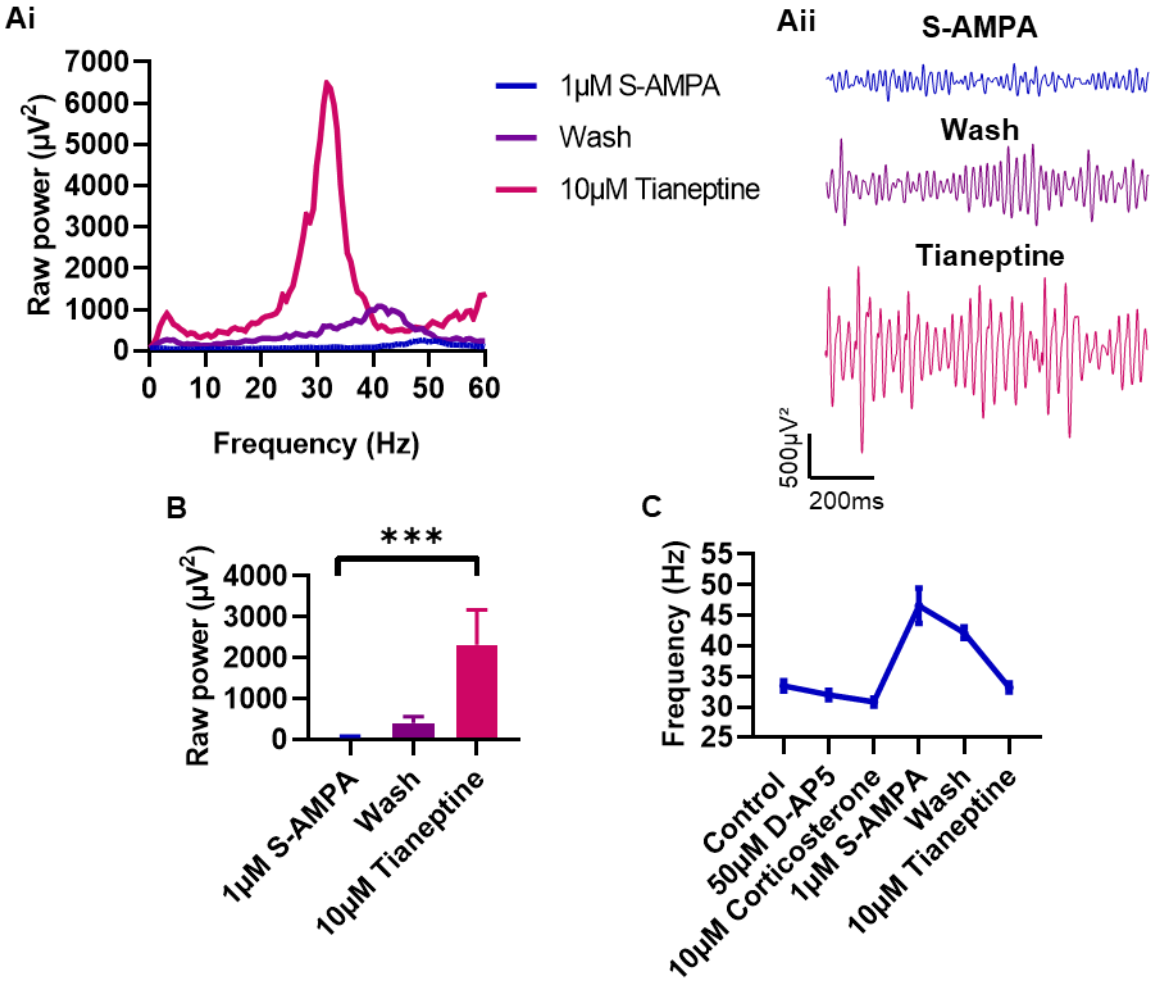

Figure 7.4. Receptor shuttling (AMPAR internalisation) in CA3.

(Ai) Example FFT showing peak gamma oscillations in s-AMPA, wash and tianeptine conditions. (Aii) Corresponding raw traces in each condition. (B) Bar chart of peak raw power in each condition. (C) Before-and-after graph of peak gamma frequency in each condition throughout the full experiment. Blue indicates s-AMPA, purple indicates wash and pink indicates tianeptine. Error bars show SEM. *** denotes $p \leq 0.001$ (Friedman one-way ANOVA test).

7.3. Discussion

AMPA stimulation results in rapid AMPAR internalisation, with AMPARs then entering a recycling endosome system. Internalisation of postsynaptic AMPARs depresses excitatory neurotransmission (Lin et al., 2000). AMPAR internalisation (endocytosis) and insertion (exocytosis) modulates synaptic strength, leading to LTD and LTP, respectively. AMPARs move between the postsynaptic membrane and the cytoplasm via lateral movement to the extrasynaptic membrane. A reduction in synaptic strength (LTD) involves AMPAR sorting to lysosomes. Blocking of NMDARs with D-AP5 allows for NMDAR-independent AMPAR internalisation, which targets AMPARs to late endosomes and lysosomes for degradation, therefore preventing reinsertion into the membrane (Ehlers, 2000, Parkinson and Hanley, 2018). Furthermore, the use of corticosterone allows for increased AMPAR surface mobility and movement, therefore resulting in increased AMPAR trafficking (Groc et al., 2008). As such, the use of D-AP5, s-AMPA and corticosterone aims to mimic the increased trafficking and then chronic loss of AMPARs seen in the RISE model of epilepsy.

AMPAR internalisation following agonism is a rapid process. Lissin *et al.* found AMPAR agonism using 100μM glutamate applied onto rat hippocampal cultures resulted in rapid internalisation and redistribution of AMPARs within 5 minutes (Lissin et al., 1999). Similarly, Ehlers reports application of s-AMPA and D-AP5 results in nearly complete internalisation of surface AMPAR within 10 minutes and sorting to late endosomes which are then degraded by lysosomes (Ehlers, 2000). This shows that activation of AMPARs results in rapid activity-dependent changes in synaptic localisation.

As well as rapid internalisation, the frequency of the remaining oscillation was massively increased following bath application of s-AMPA. Glutamate, an agonist of AMPARs, has also been found to increase the frequency of gamma rhythms (Ainsworth et al., 2016). The frequency of the local population oscillation is proportional to the output from excitatory neurons (Atallah and Scanziani, 2009), meaning increased activation by AMPAR agonists will increase the frequency of the gamma oscillation.

Following internalisation of AMPARs, there is little recovery once the wash was applied, which likely reflects the degradation pathways internalised AMPARs would have entered (Ehlers, 2000). However, upon application of tianeptine, there was recovery in the power and synchrony of the oscillations in the hippocampus back to pre-agonist control levels. This is likely due to the target phosphorylation sites of tianeptine. Tianeptine is known to target two sites (Ser831 and Ser845) on the GluA1 AMPAR subunit. AMPAR trafficking (exocytosis) and re-insertion to the postsynaptic membrane is usually mediated by PKA and CaMKII. Phosphorylation of these sites by either kinases or tianeptine will result in increased trafficking and re-insertion into the postsynaptic membrane, resulting in increased EPSPs (Derkach et al., 1999, Jenkins and Traynelis, 2012, Lee et al., 2000, Liu et al., 2009).

This acute, *in vitro* experiment suggests that despite chronic internalisation of AMPARs (LTD), it is possible to re-insert lost AMPARs with tianeptine. Of course, it is worth noting that AMPAR internalisation using this method only works on an acute scale, and chronic internalisation (like hypothesised in the RISE model of epilepsy) may result in more permanent modifications to AMPAR expression. For example, Bonini *et al.* reports that chronic AMPAR activation with low dose 10μM glutamate to rat primarily cortical cell cultures selectively results in downregulation of the RNA levels of AMPAR subunits GluA2-4 (Bonini et al., 2015). Meaning, although this *in vitro* model may have use in studying epileptogenesis and the patterns of receptor shuttling on an acute scale, it may not accurately represent the chronic losses of AMPARs seen in the RISE model of epilepsy.

Chapter 8 General discussion and future work

8.1. Introduction

Epileptogenesis is defined as the chronic pathogenic process by which a normal brain is transformed to an epileptic brain, capable of generating spontaneous seizures. Several crucial, progressive steps which develop over a period of weeks, months or sometimes years have been identified - following the initial precipitating assault/injury (e.g., trauma, status epilepticus), the brain undergoes a period of 'silence' where molecular, cellular and network changes occur. This is known as the latent period and is thought to be responsible for progression to subsequent spontaneous recurrent seizures (SRS) (Williams et al., 2009, Wong, 2009).

The latent period has become a focal point of epilepsy research due to its potential use as a therapeutic target before patients progress into symptomatic epilepsy. Animals models have been vital in allowing epilepsy researchers to explore the mechanisms of epileptogenesis, particularly during the latent period, and investigate potential therapeutic options for preventing progression. Throughout this thesis, the RISE model of epilepsy was used due its high morbidity, low mortality rates which shows consistent features of epileptogenesis in humans (such as a lack of gross damage to the brain, progressive network alteration within the temporal lobe, electrophysiological features like *in vitro* recordings of human brain tissue, and 40% - 100% of animals in any cohort (mean 69%) progressing into SRS) (Modebadze et al., 2016).

Previous work studying epileptogenesis using the RISE model only explored specific but sparse timepoints within the progression of epilepsy, therefore only giving transient snapshots of epileptogenesis. As such, it was of upmost interest to characterise the synaptic and network changes which occur during the early stages of epileptogenesis. As previous research has shown no receptor or network changes had occurred within one week of induction of epileptogenesis (Modebadze et al., 2016), we looked to explore from 2 weeks post-induction. Week-by-week analysis of the latent period continued to 6 weeks post-induction, and animals which were shown to be eliciting clinical seizures (SRS) were also investigated.

Network excitability, a measure of glutamatergic receptor activation, was explored in both spontaneous conditions and following *in vitro* bath application of 200nM KA in the hippocampus. Next, atypical antidepressant tianeptine was also explored as a potential anti-epileptogenic drug for altering the progression of epileptogenesis. And finally, seizure susceptibility following RISE induction was also investigated.

8.2. Changes in brain excitability throughout epileptogenesis

Chapter 3 modelled the progression of epileptogenesis *in vitro*. Epilepsy is described as an imbalance of excitation and inhibition (E/I balance). Notably, epilepsy has been associated with an increase in excitation and/or decrease in inhibition, leading to the emergence of hyperexcitability and hypersynchronous seizures. As such, the majority of the anti-epileptic

drugs available are aimed at restoring E/I balance, therefore reducing seizure intensity and frequency (e.g., carbamazepine and topiramate) (Shao et al., 2019).

Our understanding of epileptogenesis from the RISE model looks to challenge this idea. Previous studies of the RISE model have looked to explore the hippocampal receptor protein changes which occur throughout epileptogenesis. During the latent period, there are significant reductions in the GluA1, GluA2 and GluA3 AMPAR subunits. In approximate terms, there is a ~80% reduction in the protein expression of the AMPAR subunit GluA1 during the latent period of RISE animals compared to AMC. Also, there is ~50% reduction in the postsynaptic excitatory scaffolding protein PSD-95. There were also significant decreases in NMDAR subunits GluN1 and GluN2A, and the KAR subunit GluK5. Meaning, there are decreases in receptor subunit expression across all glutamatergic ionotropic receptor groups. The levels of these glutamatergic receptor subunits remained low as animals entered the SRS stage of epileptogenesis except for KAR subunits GluK2 and GluK5, NMDAR subunit GluN1 and the postsynaptic excitatory scaffolding protein PSD-95. Notably, this profound loss of AMPARs continued into SRS despite animals now presenting with clinical seizures (Needs et al., 2019).

Chapter 3 showed that throughout the latent period, there were reductions in hippocampal network excitability in both spontaneous and KA-induced conditions. This reached a nadir at around weeks 5 – 6 post-induction when comparing RISE animals to AMC. These observations fit with the loss of vital glutamatergic neurotransmission, particularly via AMPARs, leading to a loss of network excitability (Needs et al., 2019).

However, there appears to be recovery in network excitability as animals move into the SRS stage of epileptogenesis. How is there an increase in network excitability despite a chronic reduction in AMPAR neurotransmission? It is hypothesised this is due to a homeostatic regulation in intrinsic excitability of hippocampal pyramidal cells. Neurons will stabilise their own excitability to maintain a consistent firing rate to prevent hyper- or hypo-excitability. Chronic reductions of AMPAR neurotransmission will likely lead to reduced neuronal activity and Ca^{2+} influx. This leads to reduced activity of CAMKIV and the resulting up-scale of excitability synaptic strength and intrinsic excitability. Activated CaMKIV regulates transcription via phosphorylation of cAMP responsive element binding protein (CREB), which alters trafficking and accumulation of synaptic AMPARs to scale the synaptic strength and intrinsic excitability of neurons to its target firing rate (Joseph and Turrigiano, 2017, Turrigiano, 2008). Therefore, increasing overall network excitability in the hippocampus.

This work was further consolidated after conducting the whole-cell voltage clamp experiments as sEPSC amplitude significantly increased as animals transitioned from the latent period to the SRS stage of epileptogenesis. However, future work should focus on exploring the levels of AMPAR protein expression during the latent period and SRS, and may look to explore homeostatic scaling during these periods by conducting miniature EPSC (mEPSC) experiments. In the presence of tetrodotoxin, neurons are unable to generate action potentials.

However, presynaptic release of neurotransmitter vesicles is probabilistic and will therefore occasionally be released into the synapse, leading to activation of postsynaptic receptors and the generation of a mEPSC. Recording of mEPSCs would allow for analysis of synaptic scaling of AMPARs during epileptogenesis. Chronic down-scaling of AMPARs leads to a paradoxical increase in mEPSC amplitude and prolonged AMPAR half-life, consequently modulating the size of the mEPSC and reducing receptor turnover (O'Brien et al., 1998).

8.3. Can tianeptine modulate the progression of epileptogenesis?

The atypical tricyclic antidepressant tianeptine is used as a treatment for major depressive disorder and anxiety. Tianeptine is thought to primarily work via increased insertion/anchoring and conductance of postsynaptic AMPARs in the hippocampus, therefore increasing gamma oscillations (Lee et al., 2000, Liu et al., 2009, Man et al., 2007). Although thought to have little effect on adrenergic, dopaminergic or serotonergic receptors or transporters (Kato and Weitsch, 1988), studies have also demonstrated tianeptine is a full agonist of the mu opioid receptor which can also enhance network excitability via disinhibition of GABAergic inhibitory neurons (Gassaway et al., 2014, Samuels et al., 2017).

Bath application of tianeptine onto RISE animals throughout epileptogenesis produced interesting results. Firstly, there appears to be a reduction in network excitability and response to tianeptine during the latent period in both spontaneous and KA-induced gamma oscillations. This deficit also extended to the frequency of the gamma oscillation. Secondly, although there is an overall boost in network excitability to KA during the SRS stage of epileptogenesis, only CA1 could increase further upon application of tianeptine.

It is hypothesised that, given our understanding of AMPAR subunit expression during the latent period using the RISE model of epilepsy (Needs et al., 2019), hippocampal neurons produce fewer GluA1-mediated AMPARs and lack the appropriate scaffold proteins to anchor the remaining AMPARs into the postsynaptic membrane, therefore resulting in unchanged network excitability in the presence of tianeptine. If hippocampal neurons are simply not producing the protein necessary to assemble functional AMPARs, tianeptine cannot allow for effective insertion/anchoring of postsynaptic AMPARs. This questions the validity of tianeptine as an anti-epileptogenic drug.

Furthermore, in some cases, tianeptine resulted in an overall reduction in network excitability during the latent period of RISE animals. This could be explained by desensitisation – glutamate-induced AMPAR desensitisation results in increase synaptic diffusion of AMPARs. Approximately 50% of AMPARs continually cycle between postsynaptic and extra-synaptic locations. This increased lateral diffusion allows for exchange of desensitised receptors with naïve ones in the synapse, therefore allowing for sustainment of high-frequency synaptic transmission. The speed of this AMPAR diffusion is made possible by reduced interactions

with the AMPAR auxiliary subunit stargazin. Stargazin is involved in AMPAR stabilisation in the PSD via its interaction with scaffolding proteins (e.g., PSD-95) (Bowie and Lange, 2002, Constals et al., 2015, Robert and Howe, 2003, Traynelis et al., 2010).

In this scenario, it is possible tianeptine is increasing lateral diffusion into the postsynaptic membrane initially. However, these AMPARs are unable to be anchored effectively in the post-synaptic membrane due to lack of scaffolding proteins during the latent period, resulting in desensitisation and lateral movement back to extra-synaptic locations, therefore decreasing network excitability further. Therefore, it is thought that this study of examining network excitability using tianeptine during the latent period was investigating the differences in localisation (postsynaptic vs extrasynaptic) of the remaining AMPARs during epileptogenesis. Future work could look to explore the movement of AMPARs between post- and extrasynaptic locations by conducting receptor mapping experiments. This would allow us to track AMPAR organisation throughout epileptogenesis (Wamsley and Palacios, 1982, Zilles and Amunts, 2009).

Alternatively, it is possible that this acute bath application of tianeptine doesn't allow for effective incubation of tianeptine to have the desired effect on AMPAR trafficking and anchoring. Tramarin *et al*. studied re-recruitment and stabilisation of AMPARs in a model characterised by a mutation in the X-linked cyclin-dependent kinase-like 5 (CDKL5) gene which results in infantile seizures, impaired cognition and motor skills, and autistic features. Tianeptine was incubated for 7 days, and the authors found complete normalisation and restoration of both GluA1 and GluA2 AMPAR subunits into the cell membrane. Tianeptine was also able to restore lost accessory protein PSD-95 (Tramarin et al., 2018). Meaning, future work may look to incubate hippocampal slices *ex vivo* with tianeptine over a longer time period, or even dose RISE animals throughout different points within epileptogenesis.

Finally, to back up the above results of LFP data, future work may look to repeat the whole-cell patch clamp data conducted towards the end of chapter 4. Patch clamp data in chapter 4 aimed to explore the effects of tianeptine on synaptic neurotransmission. This produced inconclusive data which is likely due to the small number of repeats done due to time constraints. This meant that comparing the effects of tianeptine on RISE animals to AMC in chapter 5 also resulted in inconclusive findings. As such, future work may look to explore the effects of tianeptine further with larger data sets, therefore improving the reliability of the results. Given the results of previous research, it is likely there should have been a two-fold increase in peak amplitude and an increase in decay time following acute bath application of tianeptine time (Kole et al., 2002, Pillai et al., 2012). Meaning, it is likely figure 4.6. was unable to highlight this increase in EPSC effectively.

8.4. Increased seizure susceptibility using the RISE model of epilepsy

The 0 Mg^{2+} model of epilepsy offers an *in vitro* option for studying brain slice excitability by exploring experimental seizure susceptibility. This allows for analysis of seizure generation, propagation, and patterns, as well as for testing of potential AEDs. Using several parameters for analysis, the RISE model was found to have increased seizure susceptibility across all parameters employed when compared to AMC (percentage of slices to seize overall, time to first seizure (seconds), total number of seizures (count), duration of seizures (seconds) and inter-seizure interval (ISI, seconds)). This shows that induction of epileptogenesis using the RISE model puts the brain in a vulnerable state which is more prone to experimental seizure generation. However, it was found seizure susceptibility was reduced as RISE animals entered the later stages of the latent period, highlighting this seizure-free phase of epileptogenesis.

Of course, one limitation of this chapter was the lack of effective AED testing. As mentioned, the *in vitro* 0 Mg^{2+} model of epilepsy offers a way of screening potential AEDs on an acute scale. Chapters 4 and 5 explored the potential therapeutic role tianeptine could play as an anti-epileptogenic drug. Work was commenced exploring tianeptine as an AED, however, due to time constraints, not enough data was gathered for presentation in this thesis. As such, there is hope that work will continue to give a better idea of the potential therapeutic role tianeptine could play in the treatment of epileptic seizures.

8.6. Conclusion

Overall, this thesis has demonstrated that epileptogenesis is a chronic, dynamic process which results in changes in brain excitability and seizure susceptibility. Fundamentally, there is an imbalance between excitation and inhibition in the brain, with a loss of excitation appearing to drive epileptogenesis.

Brain slice excitability varies throughout epileptogenesis. As the latent period progresses, there are reductions in brain slice excitability. Once animals enter the SRS stage of epileptogenesis, this appears to recover to that of control despite animals now presenting with clinical and behavioural seizures. Similarly, although seizure susceptibility is increased overall compared to AMC, there is a reduction as RISE animals enter the latent period. 10μM tianeptine was used as a potential anti-epileptogenic drug with the aim to modify the progression of epileptogenesis, however the effectiveness of tianeptine as an anti-epileptogenic drug remains inconclusive. Although seemingly effective at recovering the oscillation at some points throughout epileptogenesis, tianeptine had little effect when applied during the later stages of the latent period. Future work should aim to further explore the mechanisms of reduced brain slice excitability and reduced seizure susceptibility during the latent period and should look to screen potential anti-epileptogenic and anti-epileptic drugs, including tianeptine, as therapeutic options.

References

ABHANG, P., GAWALI, B. W. & MEHROTRA, S. C. Technological Basics of EEG Recording and Operation of Apparatus. 2016.

ACKERMAN, S. 1992. *Discovering the Brain.* Washington (DC): National Academies Press (US)

Copyright © 1992 by the National Academy of Sciences.

AINSWORTH, M., LEE, S., KAISER, M., SIMONOTTO, J., KOPELL, N. J. & WHITTINGTON, M. A. 2016. GABA_B receptor-mediated, layer-specific synaptic plasticity reorganizes gamma-frequency neocortical response to stimulation. *Proceedings of the National Academy of Sciences,* 113**,** E2721-E2729.

AKMAN, C. I., ICHISE, M., OLSAVSKY, A., TIKOFSKY, R. S., VAN HEERTUM, R. L. & GILLIAM, F. 2010. Epilepsy duration impacts on brain glucose metabolism in temporal lobe epilepsy: results of voxel-based mapping. *Epilepsy Behav,* 17**,** 373-80.

ANAND, K. S. & DHIKAV, V. 2012. Hippocampus in health and disease: An overview. *Ann Indian Acad Neurol,* 15**,** 239-46.

ANDERSON, W. W., LEWIS, D. V., SWARTZWELDER, H. S. & WILSON, W. A. 1986. Magnesium-free medium activates seizure-like events in the rat hippocampal slice. *Brain Res,* 398**,** 215-9.

ANDREASEN, M., LAMBERT, J. D. & JENSEN, M. S. 1989. Effects of new non-N-methyl-D-aspartate antagonists on synaptic transmission in the in vitro rat hippocampus. *J Physiol,* 414**,** 317-36.

ANGELERI, F., MAJKOWSKI, J., CACCHIÒ, G., SOBIESZEK, A., D'ACUNTO, S., GESUITA, R., BACHLEDA, A., POLONARA, G., KRÓLICKI, L., SIGNORINO, M. & SALVOLINI, U. 1999. Posttraumatic Epilepsy Risk Factors: One-Year Prospective Study After Head Injury. *Epilepsia,* 40**,** 1222-1230.

ARNOLD, J. D., OLDFIELD, R. K., POLLARD, A. C. & SILINK, M. 1983. Primary hypomagnesaemia: case report. *Aust Paediatr J,* 19**,** 45-6.

ASANUMA, M., NISHIBAYASHI-ASANUMA, S., MIYAZAKI, I., KOHNO, M. & OGAWA, N. 2001. Neuroprotective effects of non-steroidal anti-inflammatory drugs by direct scavenging of nitric oxide radicals. *Journal of Neurochemistry,* 76**,** 1895-1904.

ATALLAH, B. V. & SCANZIANI, M. 2009. Instantaneous Modulation of Gamma Oscillation Frequency by Balancing Excitation with Inhibition. *Neuron,* 62**,** 566-577.

BARA, M., GUIET-BARA, A. & DURLACH, J. 1989. A qualitative theory of the screening-binding effects of magnesium salts on epithelial cell membranes: a new hypothesis. *Magnes Res,* 2**,** 243-8.

BATS, C., GROC, L. & CHOQUET, D. 2007. The Interaction between Stargazin and PSD-95 Regulates AMPA Receptor Surface Trafficking. *Neuron,* 53**,** 719-734.

BAXTER, M. G. 2009. Involvement of medial temporal lobe structures in memory and perception. *Neuron,* 61**,** 667-77.

BERG, A. T., BERKOVIC, S. F., BRODIE, M. J., BUCHHALTER, J., CROSS, J. H., VAN EMDE BOAS, W., ENGEL, J., FRENCH, J., GLAUSER, T. A., MATHERN, G. W., MOSHÉ, S. L., NORDLI, D., PLOUIN, P. & SCHEFFER, I. E. 2010. Revised terminology and concepts for organization of seizures and epilepsies: report of the ILAE Commission on Classification and Terminology, 2005-2009. *Epilepsia,* 51**,** 676-85.

BIKSON, M., RUIZ-NUÑO, A., MIRANDA, D., KRONBERG, G., JIRUSKA, P., FOX, J. E. & JEFFERYS, J. G. R. 2018. Synaptic transmission modulates while non-synaptic processes govern the transition from pre-ictal to seizure activity in vitro. *bioRxiv***,** 280321.

BINGMAN, V. P., SALAS, C. & RODRIGUEZ, F. 2009. Evolution of the Hippocampus. *In:* BINDER, M. D., HIROKAWA, N. & WINDHORST, U. (eds.) *Encyclopedia of Neuroscience.* Berlin, Heidelberg: Springer Berlin Heidelberg.

BIR, S. C., AMBEKAR, S., KUKREJA, S. & NANDA, A. 2015. Julius Caesar Arantius (Giulio Cesare Aranzi, 1530-1589) and the hippocampus of the human brain: history behind the discovery. *J Neurosurg,* 122**,** 971-5.

BLACKSTONE, C., MURPHY, T., MOSS, S., BARABAN, J. & HUGANIR, R. 1994. Cyclic AMP and synaptic activity-dependent phosphorylation of AMPA- preferring glutamate receptors. *The Journal of Neuroscience,* 14**,** 7585-7593.
BLAIR, R. D. 2012. Temporal lobe epilepsy semiology. *Epilepsy Res Treat,* 2012**,** 751510.
BLANCO, M. M., DOS SANTOS JR, J. G., PEREZ-MENDES, P., KOHEK, S. R. B., CAVARSAN, C. F., HUMMEL, M., ALBUQUERQUE, C. & MELLO, L. E. 2009. Assessment of seizure susceptibility in pilocarpine epileptic and nonepileptic Wistar rats and of seizure reinduction with pentylenetetrazole and electroshock models. *Epilepsia,* 50**,** 824-831.
BLUME, W. T., BRYAN YOUNG, G. & LEMIEUX, J. F. 1984. EEG morphology of partial epileptic seizures. *Electroencephalography and Clinical Neurophysiology,* 57**,** 295-302.
BONINI, D., FILIPPINI, A., LA VIA, L., FIORENTINI, C., FUMAGALLI, F., COLOMBI, M. & BARBON, A. 2015. Chronic glutamate treatment selectively modulates AMPA RNA editing and ADAR expression and activity in primary cortical neurons. *RNA Biology,* 12**,** 43-53.
BONSI, P., CUOMO, D., PERSIS, C. D., CENTONZE, D., BERNARDI, G., CALABRESI, P. & PISANI, A. 2005. Modulatory action of metabotropic glutamate receptor (mGluR) 5 on mGluR1 function in striatal cholinergic interneurons. *Neuropharmacology,* 49**,** 104-113.
BOSMAN, C. A., LANSINK, C. S. & PENNARTZ, C. M. A. 2014. Functions of gamma-band synchronization in cognition: from single circuits to functional diversity across cortical and subcortical systems. *European Journal of Neuroscience,* 39**,** 1982-1999.
BOWERY, N. G., BETTLER, B., FROESTL, W., GALLAGHER, J. P., MARSHALL, F., RAITERI, M., BONNER, T. I. & ENNA, S. J. 2002. International Union of Pharmacology. XXXIII. Mammalian gamma-aminobutyric acid(B) receptors: structure and function. *Pharmacol Rev,* 54**,** 247-64.
BOWIE, D. & LANGE, G. D. 2002. Functional stoichiometry of glutamate receptor desensitization. *J Neurosci,* 22**,** 3392-403.
BRAGIN, A., JANDO, G., NADASDY, Z., HETKE, J., WISE, K. & BUZSAKI, G. 1995. Gamma (40-100 Hz) oscillation in the hippocampus of the behaving rat. *The Journal of Neuroscience,* 15**,** 47-60.
BROMFIELD, E. B., CAVAZOS, J. E. & JONAS, P. 2006. An Introduction to Epilepsy. *In:* BROMFIELD, E. B., CAVAZOS, J. E. & SIRVEN, J. I. (eds.) *An Introduction to Epilepsy.* West Hartford (CT): American Epilepsy Society

BROWNING, R. A., WANG, C., LANKER, M. L. & JOBE, P. C. 1990. Electroshock- and pentylenetetrazol-induced seizures in genetically epilepsy-prone rats (GEPRs): differences in threshold and pattern. *Epilepsy Research,* 6**,** 1-11.
BUCKMASTER, C. A., EICHENBAUM, H., AMARAL, D. G., SUZUKI, W. A. & RAPP, P. R. 2004. Entorhinal cortex lesions disrupt the relational organization of memory in monkeys. *J Neurosci,* 24**,** 9811-25.
BUCKMASTER, P. S. & DUDEK, F. E. 1997. Network Properties of the Dentate Gyrus in Epileptic Rats With Hilar Neuron Loss and Granule Cell Axon Reorganization. *Journal of Neurophysiology,* 77**,** 2685-2696.
BUZSÁKI, G., ANASTASSIOU, C. A. & KOCH, C. 2012. The origin of extracellular fields and currents — EEG, ECoG, LFP and spikes. *Nature Reviews Neuroscience,* 13**,** 407-420.
BUZSÁKI, G. & DRAGUHN, A. 2004. Neuronal oscillations in cortical networks. *Science,* 304**,** 1926-9.
BUZSÁKI, G. & WANG, X. J. 2012. Mechanisms of gamma oscillations. *Annu Rev Neurosci,* 35**,** 203-25.
CAIXETA, F. V., CORNÉLIO, A. M., SCHEFFER-TEIXEIRA, R., RIBEIRO, S. & TORT, A. B. L. 2013. Ketamine alters oscillatory coupling in the hippocampus. *Scientific Reports,* 3**,** 2348.
CANTO, C. B., WOUTERLOOD, F. G. & WITTER, M. P. 2008. What does the anatomical organization of the entorhinal cortex tell us? *Neural Plast,* 2008**,** 381243.

CARLÉN, M., MELETIS, K., SIEGLE, J. H., CARDIN, J. A., FUTAI, K., VIERLING-CLAASSEN, D., RÜHLMANN, C., JONES, S. R., DEISSEROTH, K., SHENG, M., MOORE, C. I. & TSAI, L. H. 2012. A critical role for NMDA receptors in parvalbumin interneurons for gamma rhythm induction and behavior. *Mol Psychiatry,* 17**,** 537-48.
CHAUHAN, P., JETHWA, K., RATHAWA, A., CHAUHAN, G. & MEHRA, S. 2021. The Anatomy of the Hippocampus. *In:* PLUTA, R. (ed.) *Cerebral Ischemia.* Brisbane (AU): Exon Publications

CHEN, N., LUO, T. & RAYMOND, L. A. 1999. Subtype-Dependence of NMDA Receptor Channel Open Probability. *The Journal of Neuroscience,* 19**,** 6844 - 6854.
CODADU, N. K., PARRISH, R. R. & TREVELYAN, A. J. 2019. Region-specific differences and areal interactions underlying transitions in epileptiform activity. *J Physiol,* 597**,** 2079-2096.
COLGIN, L. L. & MOSER, E. I. 2010. Gamma oscillations in the hippocampus. *Physiology (Bethesda),* 25**,** 319-29.
COLLINGRIDGE, G. L., OLSEN, R. W., PETERS, J. & SPEDDING, M. 2009. A nomenclature for ligand-gated ion channels. *Neuropharmacology,* 56**,** 2-5.
CONSTALS, A., PENN, ANDREW C., COMPANS, B., TOULMÉ, E., PHILLIPAT, A., MARAIS, S., RETAILLEAU, N., HAFNER, A.-S., COUSSEN, F., HOSY, E. & CHOQUET, D. 2015. Glutamate-Induced AMPA Receptor Desensitization Increases Their Mobility and Modulates Short-Term Plasticity through Unbinding from Stargazin. *Neuron,* 85**,** 787-803.
CSICSVARI, J., JAMIESON, B., WISE, K. D. & BUZSÁKI, G. 2003. Mechanisms of gamma oscillations in the hippocampus of the behaving rat. *Neuron,* 37**,** 311-22.
CUNNINGHAM, M. O., DAVIES, C. H., BUHL, E. H., KOPELL, N. & WHITTINGTON, M. A. 2003. Gamma Oscillations Induced by Kainate Receptor Activation in the Entorhinal Cortex In Vitro. *The Journal of Neuroscience,* 23**,** 9761-9769.
CUNNINGHAM, M. O., HUNT, J., MIDDLETON, S., LEBEAU, F. E., GILLIES, M. J., DAVIES, C. H., MAYCOX, P. R., WHITTINGTON, M. A. & RACCA, C. 2006. Region-specific reduction in entorhinal gamma oscillations and parvalbumin-immunoreactive neurons in animal models of psychiatric illness. *J Neurosci,* 26**,** 2767-76.
CURIA, G., LONGO, D., BIAGINI, G., JONES, R. S. G. & AVOLI, M. 2008. The pilocarpine model of temporal lobe epilepsy. *Journal of Neuroscience Methods,* 172**,** 143-157.
CURTIS, D. R. & WATKINS, J. C. 1960. THE EXCITATION AND DEPRESSION OF SPINAL NEURONES BY STRUCTURALLY RELATED AMINO ACIDS. *Journal of Neurochemistry,* 6.
DALMAU, J., GEIS, C. & GRAUS, F. 2017. Autoantibodies to Synaptic Receptors and Neuronal Cell Surface Proteins in Autoimmune Diseases of the Central Nervous System. *Physiological Reviews,* 97**,** 839-887.
DAY, C., SILVA, J.-P., MUNRO, R., BAKER, T. S., WOLFF, C., BITHELL, A. & STEPHENS, G. J. 2023. Anti-AMPA Receptor Autoantibodies Reduce Excitatory Currents in Rat Hippocampal Neurons. *Pharmaceuticals,* 16**,** 77.
DEL RÍO, J. A., HEIMRICH, B., BORRELL, V., FÖRSTER, E., DRAKEW, A., ALCÁNTARA, S., NAKAJIMA, K., MIYATA, T., OGAWA, M., MIKOSHIBA, K., DERER, P., FROTSCHER, M. & SORIANO, E. 1997. A role for Cajal-Retzius cells and reelin in the development of hippocampal connections. *Nature,* 385**,** 70-4.
DERKACH, V., BARRIA, A. & SODERLING, T. R. 1999. Ca2+/calmodulin-kinase II enhances channel conductance of alpha-amino-3-hydroxy-5-methyl-4-isoxazolepropionate type glutamate receptors. *Proc Natl Acad Sci U S A,* 96**,** 3269-74.
DINGLEDINE, R., BORGES, K., BOWIE, D. & TRAYNELIS, S. F. 1999. The glutamate receptor ion channels. *Pharmacol Rev,* 51**,** 7-61.
DREIER, J. P. & HEINEMANN, U. 1990. Late low magnesium-induced epileptiform activity in rat entorhinal cortex slices becomes insensitive to the anticonvulsant valproic acid. *Neurosci Lett,* 119**,** 68-70.

DUBE, C., CHEN, K., EGHBAL-AHMADI, M., BRUNSON, K., SOLTESZ, I. & BARAM, T. Z. 2000. Prolonged febrile seizures in the immature rat model enhance hippocampal excitability long term. *Annals of Neurology,* 47**,** 336-344.
DULEY, L., HENDERSON-SMART, D. J., WALKER, G. J. & CHOU, D. 2010. Magnesium sulphate versus diazepam for eclampsia. *Cochrane Database Syst Rev,* 2010**,** Cd000127.
DÜRR, K. L., CHEN, L., STEIN, R. A., DE ZORZI, R., FOLEA, I. M., WALZ, T., MCHAOURAB, H. S. & GOUAUX, E. 2014. Structure and dynamics of AMPA receptor GluA2 in resting, pre-open, and desensitized states. *Cell,* 158**,** 778-792.
ECCLES, J. C. & MCGEER, P. L. 1979. Ionotropic and metabotropic neurotransmission. *Trends in Neurosciences,* 2**,** 39-40.
EGBENYA, D. L., HUSSAIN, S., LAI, Y.-C., XIA, J., ANDERSON, A. E. & DAVANGER, S. 2018. Changes in synaptic AMPA receptor concentration and composition in chronic temporal lobe epilepsy. *Molecular and Cellular Neuroscience,* 92**,** 93-103.
EHLERS, M. D. 2000. Reinsertion or degradation of AMPA receptors determined by activity-dependent endocytic sorting. *Neuron,* 28**,** 511-25.
ERIKSSON, P. S., PERFILIEVA, E., BJÖRK-ERIKSSON, T., ALBORN, A. M., NORDBORG, C., PETERSON, D. A. & GAGE, F. H. 1998. Neurogenesis in the adult human hippocampus. *Nat Med,* 4**,** 1313-7.
FAGNI, L., ANGO, F., PERROY, J. & BOCKAERT, J. 2004. Identification and functional roles of metabotropic glutamate receptor-interacting proteins. *Seminars in cell & developmental biology,* 15 3**,** 289-98.
FENG, Z. & DURAND, D. M. 2003. Low-Calcium Epileptiform Activity in the Hippocampus In Vivo. *Journal of Neurophysiology,* 90**,** 2253-2260.
FISAHN, A., CONTRACTOR, A., TRAUB, R. D., BUHL, E. H., HEINEMANN, S. F. & MCBAIN, C. J. 2004. Distinct Roles for the Kainate Receptor Subunits GluR5 and GluR6 in Kainate-Induced Hippocampal Gamma Oscillations. *The Journal of Neuroscience,* 24**,** 9658-9668.
FISAHN, A., PIKE, F. G., BUHL, E. H. & PAULSEN, O. 1998. Cholinergic induction of network oscillations at 40 Hz in the hippocampus in vitro. *Nature,* 394**,** 186-189.
FISHER, R. S., VAN EMDE BOAS, W., BLUME, W., ELGER, C., GENTON, P., LEE, P. & ENGEL, J., JR. 2005. Epileptic seizures and epilepsy: definitions proposed by the International League Against Epilepsy (ILAE) and the International Bureau for Epilepsy (IBE). *Epilepsia,* 46**,** 470-2.
FRENCH, J. A., WILLIAMSON, P. D., THADANI, V. M., DARCEY, T. M., MATTSON, R. H., SPENCER, S. S. & SPENCER, D. D. 1993. Characteristics of medial temporal lobe epilepsy: I. Results of history and physical examination. *Annals of Neurology,* 34**,** 774-780.
GASSAWAY, M. M., RIVES, M. L., KRUEGEL, A. C., JAVITCH, J. A. & SAMES, D. 2014. The atypical antidepressant and neurorestorative agent tianeptine is a μ-opioid receptor agonist. *Transl Psychiatry,* 4**,** e411.
GE, Y., DONG, Z., BAGOT, R. C., HOWLAND, J. G., PHILLIPS, A. G., WONG, T. P. & WANG, Y. T. 2010. Hippocampal long-term depression is required for the consolidation of spatial memory. *Proc Natl Acad Sci U S A,* 107**,** 16697-702.
GEIGER, J. R., MELCHER, T., KOH, D. S., SAKMANN, B., SEEBURG, P. H., JONAS, P. & MONYER, H. 1995. Relative abundance of subunit mRNAs determines gating and Ca2+ permeability of AMPA receptors in principal neurons and interneurons in rat CNS. *Neuron,* 15**,** 193-204.
GOWERS, W. R. 1901. *Epilepsy and other chronic convulsive diseases: their causes, symptoms, and treatment*, Old Hickory Bookshop.
GRAY, C. M. & MCCORMICK, D. A. 1996. Chattering Cells: Superficial Pyramidal Neurons Contributing to the Generation of Synchronous Oscillations in the Visual Cortex. *Science,* 274**,** 109-113.
GREGER, I. H., ZIFF, E. B. & PENN, A. C. 2007. Molecular determinants of AMPA receptor subunit assembly. *Trends in Neurosciences,* 30**,** 407-416.
GRIFFITHS, M. J. D., MESSENT, M., MACALLISTER, R. J. & EVANS, T. W. 1993. Aminoguanidine selectively inhibits inducible nitric oxide synthase. *British Journal of Pharmacology,* 110**,** 963-968.

GROC, L., CHOQUET, D. & CHAOULOFF, F. 2008. The stress hormone corticosterone conditions AMPAR surface trafficking and synaptic potentiation. *Nature Neuroscience,* 11**,** 868-870.
GRUETER, B. A. & WINDER, D. G. 2005. Group II and III metabotropic glutamate receptors suppress excitatory synaptic transmission in the dorsolateral bed nucleus of the stria terminalis. *Neuropsychopharmacology,* 30**,** 1302-11.
GRUNZE, H. C., RAINNIE, D. G., HASSELMO, M. E., BARKAI, E., HEARN, E. F., MCCARLEY, R. W. & GREENE, R. W. 1996. NMDA-dependent modulation of CA1 local circuit inhibition. *J Neurosci,* 16**,** 2034-43.
HAAS, C. A., DUDECK, O., KIRSCH, M., HUSZKA, C., KANN, G., POLLAK, S., ZENTNER, J. & FROTSCHER, M. 2002. Role for reelin in the development of granule cell dispersion in temporal lobe epilepsy. *The Journal of neuroscience : the official journal of the Society for Neuroscience,* 22**,** 5797-5802.
HACK, N. & BALÁZS, R. 1994. Selective stimulation of excitatory amino acid receptor subtypes and the survival of granule cells in culture: effect of quisqualate and AMPA. *Neurochemistry International,* 25**,** 235-241.
HÁJOS, N., PÁLHALMI, J., MANN, E. O., NÉMETH, B., PAULSEN, O. & FREUND, T. F. 2004. Spike timing of distinct types of GABAergic interneuron during hippocampal gamma oscillations in vitro. *J Neurosci,* 24**,** 9127-37.
HASELMANN, H., MANNARA, F., WERNER, C., PLANAGUMÀ, J., MIGUEZ-CABELLO, F., SCHMIDL, L., GRÜNEWALD, B., PETIT-PEDROL, M., KIRMSE, K., CLASSEN, J., DEMIR, F., KLÖCKER, N., SOTO, D., DOOSE, S., DALMAU, J., HALLERMANN, S. & GEIS, C. 2018. Human Autoantibodies against the AMPA Receptor Subunit GluA2 Induce Receptor Reorganization and Memory Dysfunction. *Neuron,* 100**,** 91-105.e9.
HENLEY, J. M. & WILKINSON, K. A. 2013. AMPA receptor trafficking and the mechanisms underlying synaptic plasticity and cognitive aging. *Dialogues Clin Neurosci,* 15**,** 11-27.
HESTRIN, S. 1993. Different glutamate receptor channels mediate fast excitatory synaptic currents in inhibitory and excitatory cortical neurons. *Neuron,* 11**,** 1083-91.
İNCE, R., ADANıR, S. S. & SEVMEZ, F. 2021. The inventor of electroencephalography (EEG): Hans Berger (1873–1941). *Child's Nervous System,* 37**,** 2723-2724.
ISAEV, D., IVANCHICK, G., KHMYZ, V., ISAEVA, E., SAVRASOVA, A., KRISHTAL, O., HOLMES, G. L. & MAXIMYUK, O. 2012. Surface charge impact in low-magnesium model of seizure in rat hippocampus. *J Neurophysiol,* 107**,** 417-23.
JEFFERYS, J. G. R. & HAAS, H. L. 1982. Synchronized bursting of CA1 hippocampal pyramidal cells in the absence of synaptic transmission. *Nature,* 300**,** 448-450.
JENKINS, M. A. & TRAYNELIS, S. F. 2012. PKC phosphorylates GluA1-Ser831 to enhance AMPA receptor conductance. *Channels (Austin),* 6**,** 60-4.
JONAS, P. & BURNASHEV, N. 1995. Molecular mechanisms controlling calcium entry through AMPA-type glutamate receptor channels. *Neuron,* 15**,** 987-990.
JONES, R. S. & HEINEMANN, U. 1988. Synaptic and intrinsic responses of medical entorhinal cortical cells in normal and magnesium-free medium in vitro. *J Neurophysiol,* 59**,** 1476-96.
JONES, S. W. 1990. Whole-Cell and Microelectrode Voltage Clamp. *In:* BOULTON, A. A., BAKER, G. B. & VANDERWOLF, C. H. (eds.) *Neurophysiological Techniques: Basic Methods and Concepts.* Totowa, NJ: Humana Press.
JOSEPH, A. & TURRIGIANO, G. G. 2017. All for One But Not One for All: Excitatory Synaptic Scaling and Intrinsic Excitability Are Coregulated by CaMKIV, Whereas Inhibitory Synaptic Scaling Is Under Independent Control. *J Neurosci,* 37**,** 6778-6785.
KANDRATAVICIUS, L., BALISTA, P. A., LOPES-AGUIAR, C., RUGGIERO, R. N., UMEOKA, E. H., GARCIA-CAIRASCO, N., BUENO-JUNIOR, L. S. & LEITE, J. P. 2014. Animal models of epilepsy: use and limitations. *Neuropsychiatr Dis Treat,* 10**,** 1693-705.
KAPLAN, M. S. & HINDS, J. W. 1977. Neurogenesis in the Adult Rat: Electron Microscopic Analysis of Light Radioautographs. *Science,* 197**,** 1092-1094.
KATO, G. & WEITSCH, A. F. 1988. Neurochemical profile of tianeptine, a new antidepressant drug. *Clin Neuropharmacol,* 11 Suppl 2**,** S43-50.
KATZNER, S., NAUHAUS, I., BENUCCI, A., BONIN, V., RINGACH, D. L. & CARANDINI, M. 2009. Local origin of field potentials in visual cortex. *Neuron,* 61**,** 35-41.
KEHRER, C., DUGLADZE, T., MAZIASHVILI, N., WÓJTOWICZ, A., SCHMITZ, D., HEINEMANN, U. & GLOVELI, T. 2007. Increased inhibitory input to CA1 pyramidal

cells alters hippocampal gamma frequency oscillations in the MK-801 model of acute psychosis. *Neurobiol Dis,* 25**,** 545-52.
KELLEY, M. S. & STEWARD, O. 1997. Injury-induced physiological events that may modulate gene expression in neurons and glia. *Rev Neurosci,* 8**,** 147-77.
KERR, K. M., AGSTER, K. L., FURTAK, S. C. & BURWELL, R. D. 2007. Functional neuroanatomy of the parahippocampal region: The lateral and medial entorhinal areas. *Hippocampus,* 17**,** 697-708.
KIERNAN, J. A. 2012. Anatomy of the Temporal Lobe. *Epilepsy Research and Treatment,* 2012**,** 176157.
KIM, H., CHOI, Y., JOUNG, H. Y., CHOI, Y. S., KIM, H. J., JOO, Y., OH, J. H., HANN, H. J., CHO, Z. H. & LEE, H. W. 2017. Structural and Functional Alterations at Pre-Epileptic Stage Are Closely Associated with Epileptogenesis in Pilocarpine-induced Epilepsy Model. *Exp Neurobiol,* 26**,** 287-294.
KLECKNER, N. W. & DINGLEDINE, R. J. 1988. Requirement for glycine in activation of NMDA-receptors expressed in Xenopus oocytes. *Science,* 241 4867**,** 835-7.
KNIERIM, J. J. 2015. The hippocampus. *Current Biology,* 25**,** R1116-R1121.
KOH, D. S., BURNASHEV, N. & JONAS, P. 1995. Block of native Ca(2+)-permeable AMPA receptors in rat brain by intracellular polyamines generates double rectification. *J Physiol,* 486 (Pt 2)**,** 305-12.
KOHLER, S. J., WILLIAMS, N. I., STANTON, G. B., CAMERON, J. L. & GREENOUGH, W. T. 2011. Maturation time of new granule cells in the dentate gyrus of adult macaque monkeys exceeds six months. *Proceedings of the National Academy of Sciences,* 108**,** 10326-10331.
KOLE, M. H., SWAN, L. & FUCHS, E. 2002. The antidepressant tianeptine persistently modulates glutamate receptor currents of the hippocampal CA3 commissural associational synapse in chronically stressed rats. *Eur J Neurosci,* 16**,** 807-16.
KRISTIANSEN, L. V., HUERTA, I., BENEYTO, M. & MEADOR-WOODRUFF, J. H. 2007. NMDA receptors and schizophrenia. *Curr Opin Pharmacol,* 7**,** 48-55.
KRYSTAL, J. H., KARPER, L. P., SEIBYL, J. P., FREEMAN, G. K., DELANEY, R., BREMNER, J. D., HENINGER, G. R., BOWERS, M. B., JR. & CHARNEY, D. S. 1994. Subanesthetic effects of the noncompetitive NMDA antagonist, ketamine, in humans. Psychotomimetic, perceptual, cognitive, and neuroendocrine responses. *Arch Gen Psychiatry,* 51**,** 199-214.
LE DUIGOU, C., SIMONNET, J., TELEÑCZUK, M. T., FRICKER, D. & MILES, R. 2014. Recurrent synapses and circuits in the CA3 region of the hippocampus: an associative network. *Front Cell Neurosci,* 7**,** 262.
LEE, H. K., BARBAROSIE, M., KAMEYAMA, K., BEAR, M. F. & HUGANIR, R. L. 2000. Regulation of distinct AMPA receptor phosphorylation sites during bidirectional synaptic plasticity. *Nature,* 405**,** 955-9.
LEINEKUGEL, X., KHALILOV, I., MCLEAN, H., CAILLARD, O., GAIARSA, J. L., BEN-ARI, Y. & KHAZIPOV, R. 1999. GABA is the principal fast-acting excitatory transmitter in the neonatal brain. *Advances in neurology,* 79**,** 189-201.
LERTWITTAYANON, W., DEVINSKY, O. & CARLEN, P. 2019. Cardiorespiratory depression from brainstem seizure activity in freely moving rats. *Neurobiology of Disease,* 134**,** 104628.
LEWIS, D. V., JONES, L. S. & MOTT, D. D. 1990. Hippocampal epileptiform activity induced by magnesium-free medium: differences between areas CA1 and CA2–3. *Epilepsy Research,* 6**,** 95-101.
LIN, J. W., JU, W., FOSTER, K., LEE, S. H., AHMADIAN, G., WYSZYNSKI, M., WANG, Y. T. & SHENG, M. 2000. Distinct molecular mechanisms and divergent endocytotic pathways of AMPA receptor internalization. *Nature Neuroscience,* 3**,** 1282-1290.
LISMAN, J. 1989. A mechanism for the Hebb and the anti-Hebb processes underlying learning and memory. *Proc Natl Acad Sci U S A,* 86**,** 9574-8.
LISMAN, J., SCHULMAN, H. & CLINE, H. 2002. The molecular basis of CaMKII function in synaptic and behavioural memory. *Nat Rev Neurosci,* 3**,** 175-90.
LISSIN, D. V., CARROLL, R. C., NICOLL, R. A., MALENKA, R. C. & VON ZASTROW, M. 1999. Rapid, activation-induced redistribution of ionotropic glutamate receptors in cultured hippocampal neurons. *J Neurosci,* 19**,** 1263-72.

LIU, Y., SUN, Q. A., CHEN, Q., LEE, T. H., HUANG, Y., WETSEL, W. C., MICHELOTTI, G. A., SULLENGER, B. A. & ZHANG, X. 2009. Targeting inhibition of GluR1 Ser845 phosphorylation with an RNA aptamer that blocks AMPA receptor trafficking. *J Neurochem,* 108**,** 147-57.
LÖSCHER, W., HIRSCH, L. J. & SCHMIDT, D. 2015. The enigma of the latent period in the development of symptomatic acquired epilepsy — Traditional view versus new concepts. *Epilepsy & Behavior,* 52**,** 78-92.
LOWENSTEIN, D. H., THOMAS, M. J., SMITH, D. H. & MCINTOSH, T. K. 1992. Selective vulnerability of dentate hilar neurons following traumatic brain injury: a potential mechanistic link between head trauma and disorders of the hippocampus. *J Neurosci,* 12**,** 4846-53.
LU, W.-Y., MAN, H.-Y., JU, W., TRIMBLE, W. S., MACDONALD, J. F. & WANG, Y. T. 2001. Activation of Synaptic NMDA Receptors Induces Membrane Insertion of New AMPA Receptors and LTP in Cultured Hippocampal Neurons. *Neuron,* 29**,** 243-254.
LU, W., SHI, Y., JACKSON, A. C., BJORGAN, K., DURING, M. J., SPRENGEL, R., SEEBURG, P. H. & NICOLL, R. A. 2009. Subunit Composition of Synaptic AMPA Receptors Revealed by a Single-Cell Genetic Approach. *Neuron,* 62**,** 254-268.
LÜSCHER, C. & MALENKA, R. C. 2012. NMDA receptor-dependent long-term potentiation and long-term depression (LTP/LTD). *Cold Spring Harb Perspect Biol,* 4.
MACDONALD, J. F., BARTLETT, M. C., MODY, I., PAHAPILL, P., REYNOLDS, J. N., SALTER, M. W., SCHNEIDERMAN, J. H. & PENNEFATHER, P. S. 1991. Actions of ketamine, phencyclidine and MK-801 on NMDA receptor currents in cultured mouse hippocampal neurones. *J Physiol,* 432**,** 483-508.
MAGARIÑOS, A. M., DESLANDES, A. & MCEWEN, B. S. 1999. Effects of antidepressants and benzodiazepine treatments on the dendritic structure of CA3 pyramidal neurons after chronic stress. *Eur J Pharmacol,* 371**,** 113-22.
MAKSYMENKO, K. 2019. *Novel algorithmic approaches for the forward and inverse M/EEG problems.*
MALENKA, R. C. & NICOLL, R. A. 1999. Long-term potentiation--a decade of progress? *Science,* 285**,** 1870-4.
MAN, H. Y., SEKINE-AIZAWA, Y. & HUGANIR, R. L. 2007. Regulation of {alpha}-amino-3-hydroxy-5-methyl-4-isoxazolepropionic acid receptor trafficking through PKA phosphorylation of the Glu receptor 1 subunit. *Proc Natl Acad Sci U S A,* 104**,** 3579-84.
MANN, E. O., SUCKLING, J. M., HAJOS, N., GREENFIELD, S. A. & PAULSEN, O. 2005. Perisomatic Feedback Inhibition Underlies Cholinergically Induced Fast Network Oscillations in the Rat Hippocampus In Vitro. *Neuron,* 45**,** 105-117.
MARX, M., HAAS, C. & HÄUSSLER, U. 2013. Differential vulnerability of interneurons in the epileptic hippocampus. *Frontiers in Cellular Neuroscience,* 7.
MAYER, M. L., WESTBROOK, G. L. & GUTHRIE, P. B. 1984. Voltage-dependent block by Mg2+ of NMDA responses in spinal cord neurones. *Nature,* 309**,** 261-263.
MCEWEN, B. S., CHATTARJI, S., DIAMOND, D. M., JAY, T. M., REAGAN, L. P., SVENNINGSSON, P. & FUCHS, E. 2010. The neurobiological properties of tianeptine (Stablon): from monoamine hypothesis to glutamatergic modulation. *Molecular Psychiatry,* 15**,** 237-249.
MCNALLY, J. M., MCCARLEY, R. W., MCKENNA, J. T., YANAGAWA, Y. & BROWN, R. E. 2011. Complex receptor mediation of acute ketamine application on in vitro gamma oscillations in mouse prefrontal cortex: modeling gamma band oscillation abnormalities in schizophrenia. *Neuroscience,* 199**,** 51-63.
MENNITI, F. S., BUCHAN, A. M., CHENARD, B. L., CRITCHETT, D. J., GANONG, A. H., GUANOWSKY, V., SEYMOUR, P. A. & WELCH, W. M. 2003. CP-465,022, a selective noncompetitive AMPA receptor antagonist, blocks AMPA receptors but is not neuroprotective in vivo. *Stroke,* 34**,** 171-6.
MIKASOVA, L., XIONG, H., KERKHOFS, A., BOUCHET, D., KRUGERS, H. J. & GROC, L. 2017. Stress hormone rapidly tunes synaptic NMDA receptor through membrane dynamics and mineralocorticoid signalling. *Scientific Reports,* 7**,** 8053.
MITZDORF, U. 1985. Current source-density method and application in cat cerebral cortex: investigation of evoked potentials and EEG phenomena. *Physiological Reviews,* 65**,** 37-100.

MIZUTA, K., XU, D., PAN, Y., COMAS, G., SONETT, J. R., ZHANG, Y., PANETTIERI, R. A., JR., YANG, J. & EMALA, C. W., SR. 2008. GABAA receptors are expressed and facilitate relaxation in airway smooth muscle. *Am J Physiol Lung Cell Mol Physiol,* 294**,** L1206-16.
MODEBADZE, T., MORGAN, N. H., PÉRÈS, I. A. A., HADID, R. D., AMADA, N., HILL, C., WILLIAMS, C., STANFORD, I. M., MORRIS, C. M., JONES, R. S. G., WHALLEY, B. J. & WOODHALL, G. L. 2016. A Low Mortality, High Morbidity Reduced Intensity Status Epilepticus (RISE) Model of Epilepsy and Epileptogenesis in the Rat. *PLOS ONE,* 11**,** e0147265.
MORENO-JIMÉNEZ, E. P., TERREROS-RONCAL, J., FLOR-GARCÍA, M., RÁBANO, A. & LLORENS-MARTÍN, M. 2021. Evidences for Adult Hippocampal Neurogenesis in Humans. *The Journal of Neuroscience,* 41**,** 2541-2553.
NADEL, L. & MOSCOVITCH, M. 1997. Memory consolidation, retrograde amnesia and the hippocampal complex. *Curr Opin Neurobiol,* 7**,** 217-27.
NAHAR, L., DELACROIX, B. M. & NAM, H. W. 2021. The Role of Parvalbumin Interneurons in Neurotransmitter Balance and Neurological Disease. *Frontiers in Psychiatry,* 12.
NEEDS, H. I., HENLEY, B. S., CAVALLO, D., GURUNG, S., MODEBADZE, T., WOODHALL, G. & HENLEY, J. M. 2019. Changes in excitatory and inhibitory receptor expression and network activity during induction and establishment of epilepsy in the rat Reduced Intensity Status Epilepticus (RISE) model. *Neuropharmacology,* 158**,** 107728.
NEHLIG, A., DUBÉ, C. & KONING, E. 2002. Status epilepticus induced by lithium-pilocarpine in the immature rat does not change the long-term susceptibility to seizures. *Epilepsy Research,* 51**,** 189-197.
NEVES, G., COOKE, S. F. & BLISS, T. V. P. 2008. Synaptic plasticity, memory and the hippocampus: a neural network approach to causality. *Nature Reviews Neuroscience,* 9**,** 65-75.
NIKOLAEV, M. V., MAGAZANIK, L. G. & TIKHONOV, D. B. 2012. Influence of external magnesium ions on the NMDA receptor channel block by different types of organic cations. *Neuropharmacology,* 62**,** 2078-2085.
NITTA, N., HEINRICH, C., HIRAI, H. & SUZUKI, F. 2008. Granule cell dispersion develops without neurogenesis and does not fully depend on astroglial cell generation in a mouse model of temporal lobe epilepsy. *Epilepsia,* 49**,** 1711-1722.
NUYTTEN, D., VAN HEES, J., MEULEMANS, A. & CARTON, H. 1991. Magnesium deficiency as a cause of acute intractable seizures. *J Neurol,* 238**,** 262-4.
O'BRIEN, R. J., KAMBOJ, S., EHLERS, M. D., ROSEN, K. R., FISCHBACH, G. D. & HUGANIR, R. L. 1998. Activity-Dependent Modulation of Synaptic AMPA Receptor Accumulation. *Neuron,* 21**,** 1067-1078.
OHARA, S., ONODERA, M., SIMONSEN Ø, W., YOSHINO, R., HIOKI, H., IIJIMA, T., TSUTSUI, K. I. & WITTER, M. P. 2018. Intrinsic Projections of Layer Vb Neurons to Layers Va, III, and II in the Lateral and Medial Entorhinal Cortex of the Rat. *Cell Rep,* 24**,** 107-116.
OLSEN, R. W. & SIEGHART, W. 2008. International Union of Pharmacology. LXX. Subtypes of gamma-aminobutyric acid(A) receptors: classification on the basis of subunit composition, pharmacology, and function. Update. *Pharmacol Rev,* 60**,** 243-60.
PANG, C. C.-C., KIECKER, C., O'BRIEN, J. T., NOBLE, W. & CHANG, R. C.-C. 2019. Ammon's Horn 2 (CA2) of the Hippocampus: A Long-Known Region with a New Potential Role in Neurodegeneration. *The Neuroscientist,* 25**,** 167-180.
PAOLETTI, P., BELLONE, C. & ZHOU, Q. 2013. NMDA receptor subunit diversity: impact on receptor properties, synaptic plasticity and disease. *Nat Rev Neurosci,* 14**,** 383-400.
PAOLETTI, P. & NEYTON, J. 2007. NMDA receptor subunits: function and pharmacology. *Curr Opin Pharmacol,* 7**,** 39-47.
PARKINSON, G. T. & HANLEY, J. G. 2018. Mechanisms of AMPA Receptor Endosomal Sorting. *Front Mol Neurosci,* 11**,** 440.
PASCUAL, M. R. 2007. Temporal lobe epilepsy: clinical semiology and neurophysiological studies. *Semin Ultrasound CT MR,* 28**,** 416-23.
PELKEY, K. A., CHITTAJALLU, R., CRAIG, M. T., TRICOIRE, L., WESTER, J. C. & MCBAIN, C. J. 2017. Hippocampal GABAergic Inhibitory Interneurons. *Physiol Rev,* 97**,** 1619-1747.

PENG, W., COTRINA, M. L., HAN, X., YU, H., BEKAR, L., BLUM, L., TAKANO, T., TIAN, G. F., GOLDMAN, S. A. & NEDERGAARD, M. 2009. Systemic administration of an antagonist of the ATP-sensitive receptor P2X7 improves recovery after spinal cord injury. *Proc Natl Acad Sci U S A,* 106**,** 12489-93.
PENG, X., HUGHES, E. G., MOSCATO, E. H., PARSONS, T. D., DALMAU, J. & BALICE-GORDON, R. J. 2015. Cellular plasticity induced by anti–α-amino-3-hydroxy-5-methyl-4-isoxazolepropionic acid (AMPA) receptor encephalitis antibodies. *Annals of Neurology,* 77**,** 381-398.
PILLAI, A. G., ANILKUMAR, S. & CHATTARJI, S. 2012. The Same Antidepressant Elicits Contrasting Patterns of Synaptic Changes in the Amygdala vs Hippocampus. *Neuropsychopharmacology,* 37**,** 2702-2711.
PIN, J. P., KNIAZEFF, J., GOUDET, C., BESSIS, A. S., LIU, J., GALVEZ, T., ACHER, F., RONDARD, P. & PRÉZEAU, L. 2004. The activation mechanism of class-C G-protein coupled receptors. *Biol Cell,* 96**,** 335-42.
PINAULT, D. 2008. N-methyl d-aspartate receptor antagonists ketamine and MK-801 induce wake-related aberrant gamma oscillations in the rat neocortex. *Biol Psychiatry,* 63**,** 730-5.
PITKÄNEN, A. & LUKASIUK, K. 2011. Mechanisms of epileptogenesis and potential treatment targets. *The Lancet Neurology,* 10**,** 173-186.
PRIEL, A., SELAK, S., LERMA, J. & STERN-BACH, Y. 2006. Block of kainate receptor desensitization uncovers a key trafficking checkpoint. *Neuron,* 52**,** 1037-46.
PROCTOR, P. H. 2008. Uric Acid: Neuroprotective or Neurotoxic? *Stroke,* 39**,** e88-e88.
QUILICHINI, P. P., DIABIRA, D., CHIRON, C., BEN-ARI, Y. & GOZLAN, H. 2002. Persistent epileptiform activity induced by low Mg2+ in intact immature brain structures. *Eur J Neurosci,* 16**,** 850-60.
RACINE, R. J. 1972. Modification of seizure activity by electrical stimulation. II. Motor seizure. *Electroencephalogr Clin Neurophysiol,* 32**,** 281-94.
RAY, S. & MAUNSELL, J. H. 2015. Do gamma oscillations play a role in cerebral cortex? *Trends Cogn Sci,* 19**,** 78-85.
RICE, A. C., FLOYD, C. L., LYETH, B. G., HAMM, R. J. & DELORENZO, R. J. 1998. Status epilepticus causes long-term NMDA receptor-dependent behavioral changes and cognitive deficits. *Epilepsia,* 39**,** 1148-57.
ROBERT, A. & HOWE, J. R. 2003. How AMPA receptor desensitization depends on receptor occupancy. *J Neurosci,* 23**,** 847-58.
ROCHE, K. W., O'BRIEN, R. J., MAMMEN, A. L., BERNHARDT, J. & HUGANIR, R. L. 1996. Characterization of Multiple Phosphorylation Sites on the AMPA Receptor GluR1 Subunit. *Neuron,* 16**,** 1179-1188.
ROOHI-AZIZI, M., AZIMI, L., HEYSIEATTALAB, S. & AAMIDFAR, M. 2017. Changes of the brain's bioelectrical activity in cognition, consciousness, and some mental disorders. *Medical Journal of the Islamic Republic of Iran,* 31**,** 53 - 53.
ROTHMAN, S. M. 1985. The neurotoxicity of excitatory amino acids is produced by passive chloride influx. *The Journal of neuroscience : the official journal of the Society for Neuroscience,* 5**,** 1483-1489.
ROUX, L. & BUZSÁKI, G. 2015. Tasks for inhibitory interneurons in intact brain circuits. *Neuropharmacology,* 88**,** 10-23.
SAMUELS, B. A., NAUTIYAL, K. M., KRUEGEL, A. C., LEVINSTEIN, M. R., MAGALONG, V. M., GASSAWAY, M. M., GRINNELL, S. G., HAN, J., ANSONOFF, M. A., PINTAR, J. E., JAVITCH, J. A., SAMES, D. & HEN, R. 2017. The Behavioral Effects of the Antidepressant Tianeptine Require the Mu-Opioid Receptor. *Neuropsychopharmacology,* 42**,** 2052-2063.
SANCHEZ, R. M., KOH, S., RIO, C., WANG, C., LAMPERTI, E. D., SHARMA, D., CORFAS, G. & JENSEN, F. E. 2001. Decreased glutamate receptor 2 expression and enhanced epileptogenesis in immature rat hippocampus after perinatal hypoxia-induced seizures. *J Neurosci,* 21**,** 8154-63.
SANZ-CLEMENTE, A., NICOLL, R. A. & ROCHE, K. W. 2013. Diversity in NMDA Receptor Composition:Many Regulators, Many Consequences. *The Neuroscientist,* 19**,** 62-75.
SCHULTE, J. T., WIERENGA, C. J. & BRUINING, H. 2018. Chloride transporters and GABA polarity in developmental, neurological and psychiatric conditions. *Neurosci Biobehav Rev,* 90**,** 260-271.

SEMPLE, B. D., BLOMGREN, K., GIMLIN, K., FERRIERO, D. M. & NOBLE-HAEUSSLEIN, L. J. 2013. Brain development in rodents and humans: Identifying benchmarks of maturation and vulnerability to injury across species. *Prog Neurobiol,* 106-107**,** 1-16.
SHAO, L.-R., HABELA, C. W. & STAFSTROM, C. E. 2019. Pediatric Epilepsy Mechanisms: Expanding the Paradigm of Excitation/Inhibition Imbalance. *Children,* 6**,** 23.
SHETTY, A. K. & TURNER, D. A. 2001. Glutamic acid decarboxylase-67-positive hippocampal interneurons undergo a permanent reduction in number following kainic acid-induced degeneration of ca3 pyramidal neurons. *Exp Neurol,* 169**,** 276-97.
SHORVON, S. D. 2011. The etiologic classification of epilepsy. *Epilepsia,* 52**,** 1052-1057.
SHUAI, J., BIKSON, M., HAHN, P. J., LIAN, J. & DURAND, D. M. 2003. Ionic Mechanisms Underlying Spontaneous CA1 Neuronal Firing in Ca2+-Free Solution. *Biophysical Journal,* 84**,** 2099-2111.
SIEGHART, W. & SAVIĆ, M. M. 2018. International Union of Basic and Clinical Pharmacology. CVI: GABA(A) Receptor Subtype- and Function-selective Ligands: Key Issues in Translation to Humans. *Pharmacol Rev,* 70**,** 836-878.
SIGEL, E. & BUHR, A. 1997. The benzodiazepine binding site of GABAA receptors. *Trends Pharmacol Sci,* 18**,** 425-9.
SIGEL, E. & STEINMANN, M. E. 2012. Structure, function, and modulation of GABA(A) receptors. *J Biol Chem,* 287**,** 40224-31.
SIRVEN, J. I. 2015. Epilepsy: A Spectrum Disorder. *Cold Spring Harb Perspect Med,* 5**,** a022848.
SLOVITER, R. S. 1992. Possible functional consequences of synaptic reorganization in the dentate gyrus of kainate-treated rats. *Neuroscience Letters,* 137**,** 91-96.
SMALL, S. A., SCHOBEL, S. A., BUXTON, R. B., WITTER, M. P. & BARNES, C. A. 2011. A pathophysiological framework of hippocampal dysfunction in ageing and disease. *Nature Reviews Neuroscience,* 12**,** 585-601.
SOKOLOVA, S., SCHMITZ, D., ZHANG, C. L., LÖSCHER, W. & HEINEMANN, U. 1998. Comparison of effects of valproate and trans-2-en-valproate on different forms of epileptiform activity in rat hippocampal and temporal cortex slices. *Epilepsia,* 39**,** 251-8.
SOMMER, B., KÖHLER, M., SPRENGEL, R. & SEEBURG, P. H. 1991. RNA editing in brain controls a determinant of ion flow in glutamate-gated channels. *Cell,* 67**,** 11-9.
SQUIRE, L. R. 2009. The legacy of patient H.M. for neuroscience. *Neuron,* 61**,** 6-9.
STAFSTROM, C. E. & CARMANT, L. 2015. Seizures and epilepsy: an overview for neuroscientists. *Cold Spring Harb Perspect Med,* 5.
STALEY, K. J. & DUDEK, F. E. 2006. Interictal Spikes and Epileptogenesis. *Epilepsy Currents,* 6**,** 199-202.
STEWARD, O. & SCOVILLE, S. A. 1976. Cells of origin of entorhinal cortical afferents to the hippocampus and fascia dentata of the rat. *J Comp Neurol,* 169**,** 347-70.
SVENNINGSSON, P., BATEUP, H., QI, H., TAKAMIYA, K., HUGANIR, R. L., SPEDDING, M., ROTH, B. L., MCEWEN, B. S. & GREENGARD, P. 2007. Involvement of AMPA receptor phosphorylation in antidepressant actions with special reference to tianeptine. *Eur J Neurosci,* 26**,** 3509-17.
SVOBODA, K. R., ADAMS, C. E. & LUPICA, C. R. 1999. Opioid receptor subtype expression defines morphologically distinct classes of hippocampal interneurons. *J Neurosci,* 19**,** 85-95.
SZEGEDI, V., JUHÁSZ, G., ZHANG, X., BARKÓCZI, B., QI, H., MADEIRA, A., KAPUS, G., SVENNINGSSON, P., SPEDDING, M. & PENKE, B. 2011. Tianeptine potentiates AMPA receptors by activating CaMKII and PKA via the p38, p42/44 MAPK and JNK pathways. *Neurochem Int,* 59**,** 1109-22.
TAMAOKI, T., NOMOTO, H., TAKAHASHI, I., KATO, Y., MORIMOTO, M. & TOMITA, F. 1986. Staurosporine, a potent inhibitor of phospholipid/Ca++dependent protein kinase. *Biochem Biophys Res Commun,* 135**,** 397-402.
TARNAWA, I., MOLNÁR, P., GAÁL, L. & ANDRÁSI, F. 1992. Inhibition of hippocampal field potentials by GYKI 52466 in vitro and in vivo. *Acta Physiol Hung,* 79**,** 163-9.
TERRANOVA, J. I., OGAWA, S. K. & KITAMURA, T. 2019. Adult hippocampal neurogenesis for systems consolidation of memory. *Behav Brain Res,* 372**,** 112035.
THEODORE, W. H., KELLEY, K., TOCZEK, M. T. & GAILLARD, W. D. 2004. Epilepsy duration, febrile seizures, and cerebral glucose metabolism. *Epilepsia,* 45**,** 276-9.

TOMITA, S., ADESNIK, H., SEKIGUCHI, M., ZHANG, W., WADA, K., HOWE, J. R., NICOLL, R. A. & BREDT, D. S. 2005. Stargazin modulates AMPA receptor gating and trafficking by distinct domains. *Nature,* 435**,** 1052-8.
TRAMARIN, M., RUSCONI, L., PIZZAMIGLIO, L., BARBIERO, I., PERONI, D., SCARAMUZZA, L., GUILLIAMS, T., CAVALLA, D., ANTONUCCI, F. & KILSTRUP-NIELSEN, C. 2018. The antidepressant tianeptine reverts synaptic AMPA receptor defects caused by deficiency of CDKL5. *Human Molecular Genetics,* 27**,** 2052-2063.
TRAUB, R. D., WHITTINGTON, M. A., STANFORD, I. M. & JEFFERYS, J. G. 1996. A mechanism for generation of long-range synchronous fast oscillations in the cortex. *Nature,* 383**,** 621-4.
TRAYNELIS, S. F., WOLLMUTH, L. P., MCBAIN, C. J., MENNITI, F. S., VANCE, K. M., OGDEN, K. K., HANSEN, K. B., YUAN, H., MYERS, S. J. & DINGLEDINE, R. 2010. Glutamate receptor ion channels: structure, regulation, and function. *Pharmacol Rev,* 62**,** 405-96.
TREIMAN, D. M., WALTON, N. Y. & KENDRICK, C. 1990. A progressive sequence of electroencephalographic changes during generalized convulsive status epilepticus. *Epilepsy Research,* 5**,** 49-60.
TUDOR, M., TUDOR, L. & TUDOR, K. I. 2005. [Hans Berger (1873-1941)--the history of electroencephalography]. *Acta Med Croatica,* 59**,** 307-13.
TURRIGIANO, G. G. 2008. The self-tuning neuron: synaptic scaling of excitatory synapses. *Cell,* 135**,** 422-35.
TURRIGIANO, G. G. & NELSON, S. B. 2004. Homeostatic plasticity in the developing nervous system. *Nature Reviews Neuroscience,* 5**,** 97-107.
TURSKI, W. A., CAVALHEIRO, E. A., SCHWARZ, M., CZUCZWAR, S. J., KLEINROK, Z. & TURSKI, L. 1983. Limbic seizures produced by pilocarpine in rats: Behavioural, electroencephalographic and neuropathological study. *Behavioural Brain Research,* 9**,** 315-335.
UHLHAAS, P. J. & SINGER, W. 2006. Neural synchrony in brain disorders: relevance for cognitive dysfunctions and pathophysiology. *Neuron,* 52**,** 155-68.
VEZZANI, A. 2009. Pilocarpine-induced seizures revisited: what does the model mimic? *Epilepsy Curr,* 9**,** 146-8.
VICINI, S., WANG, J. F., LI, J. H., ZHU, W. J., WANG, Y. H., LUO, J. H., WOLFE, B. B. & GRAYSON, D. R. 1998. Functional and Pharmacological Differences Between RecombinantN-Methyl-d-Aspartate Receptors. *Journal of Neurophysiology,* 79**,** 555-566.
WALTHER, H., LAMBERT, J. D., JONES, R. S., HEINEMANN, U. & HAMON, B. 1986. Epileptiform activity in combined slices of the hippocampus, subiculum and entorhinal cortex during perfusion with low magnesium medium. *Neurosci Lett,* 69**,** 156-61.
WAMSLEY, J. K. & PALACIOS, J. M. 1982. Receptor Mapping by Histochemistry. *In:* LAJTHA, A. (ed.) *Experimental Neurochemistry.* Boston, MA: Springer US.
WANG, L., ZHAO, D., WANG, M., WANG, Y., VREUGDENHIL, M., LIN, J. & LU, C. 2020. Modulation of Hippocampal Gamma Oscillations by Dopamine in Heterozygous Reeler Mice in vitro. *Frontiers in Cellular Neuroscience,* 13.
WANG, X. J. 1993. Ionic basis for intrinsic 40 Hz neuronal oscillations. *Neuroreport,* 5**,** 221-4.
WENTHOLD, R. J., PETRALIA, R. S., BLAHOS, J., II & NIEDZIELSKI, A. S. 1996. Evidence for multiple AMPA receptor complexes in hippocampal CA1/CA2 neurons. *J Neurosci,* 16**,** 1982-9.
WHITLOCK, J. R., HEYNEN, A. J., SHULER, M. G. & BEAR, M. F. 2006. Learning induces long-term potentiation in the hippocampus. *Science,* 313**,** 1093-7.
WILLIAMS, P. A., WHITE, A. M., CLARK, S., FERRARO, D. J., SWIERCZ, W., STALEY, K. J. & DUDEK, F. E. 2009. Development of Spontaneous Recurrent Seizures after Kainate-Induced Status Epilepticus. *The Journal of Neuroscience,* 29**,** 2103-2112.
WITTER, M. P., DOAN, T. P., JACOBSEN, B., NILSSEN, E. S. & OHARA, S. 2017. Architecture of the Entorhinal Cortex A Review of Entorhinal Anatomy in Rodents with Some Comparative Notes. *Frontiers in Systems Neuroscience,* 11.
WITTER, M. P., NABER, P. A., VAN HAEFTEN, T., MACHIELSEN, W. C., ROMBOUTS, S. A., BARKHOF, F., SCHELTENS, P. & LOPES DA SILVA, F. H. 2000. Cortico-hippocampal communication by way of parallel parahippocampal-subicular pathways. *Hippocampus,* 10**,** 398-410.

WONG, C. G., BOTTIGLIERI, T. & SNEAD, O. C., 3RD 2003. GABA, gamma-hydroxybutyric acid, and neurological disease. *Ann Neurol,* 54 Suppl 6**,** S3-12.
WONG, M. 2009. The Window of Epileptogenesis: Looking beyond the Latent Period. *Epilepsy Currents,* 9**,** 144-145.
WOUTERLOOD, F. G., VAN HAEFTEN, T., EIJKHOUDT, M., BAKS-TE-BULTE, L., GOEDE, P. H. & WITTER, M. P. 2004. Input from the presubiculum to dendrites of layer-V neurons of the medial entorhinal cortex of the rat. *Brain Res,* 1013**,** 1-12.
WRIGHT, A. L. & VISSEL, B. 2012. The essential role of AMPA receptor GluR2 subunit RNA editing in the normal and diseased brain. *Frontiers in Molecular Neuroscience,* 5.
WUARIN, J. P. & DUDEK, F. E. 1996. Electrographic Seizures and New Recurrent Excitatory Circuits in the Dentate Gyrus of Hippocampal Slices from Kainate-Treated Epileptic Rats. *The Journal of Neuroscience,* 16**,** 4438 - 4448.
WUARIN, J. P. & DUDEK, F. E. 2001. Excitatory synaptic input to granule cells increases with time after kainate treatment. *Journal of neurophysiology,* 85 3**,** 1067-77.
YAARI, Y., KONNERTH, A. & HEINEMANN, U. 1983. Spontaneous epileptiform activity of ca1 hippocampal neurons in low extracellular calcium solutions. *Experimental Brain Research,* 51**,** 153-156.
YAMAZAKI, M., OHNO-SHOSAKU, T., FUKAYA, M., KANO, M., WATANABE, M. & SAKIMURA, K. 2004. A novel action of stargazin as an enhancer of AMPA receptor activity. *Neurosci Res,* 50**,** 369-74.
YANO, S., TOKUMITSU, H. & SODERLING, T. R. 1998. Calcium promotes cell survival through CaM-K kinase activation of the protein-kinase-B pathway. *Nature,* 396**,** 584-587.
YUAN, T.-F., LI, J., DING, F. & ARIAS-CARRION, O. 2014. Evidence of adult neurogenesis in non-human primates and human. *Cell and Tissue Research,* 358**,** 17-23.
ZEMANKOVICS, R., VERES, J. M., OREN, I. & HÁJOS, N. 2013. Feedforward Inhibition Underlies the Propagation of Cholinergically Induced Gamma Oscillations from Hippocampal CA3 to CA1. *The Journal of Neuroscience,* 33**,** 12337-12351.
ZHANG, C. L., DREIER, J. P. & HEINEMANN, U. 1995. Paroxysmal epileptiform discharges in temporal lobe slices after prolonged exposure to low magnesium are resistant to clinically used anticonvulsants. *Epilepsy Res,* 20**,** 105-11.
ZHANG, G., RAOL, Y. S., HSU, F. C. & BROOKS-KAYAL, A. R. 2004. Long-term alterations in glutamate receptor and transporter expression following early-life seizures are associated with increased seizure susceptibility. *J Neurochem,* 88**,** 91-101.
ZHANG, H., ETHERINGTON, L. A., HAFNER, A. S., BELELLI, D., COUSSEN, F., DELAGRANGE, P., CHAOULOFF, F., SPEDDING, M., LAMBERT, J. J., CHOQUET, D. & GROC, L. 2013. Regulation of AMPA receptor surface trafficking and synaptic plasticity by a cognitive enhancer and antidepressant molecule. *Mol Psychiatry,* 18**,** 471-84.
ZHANG, W., ROBERT, A., VOGENSEN, S. B. & HOWE, J. R. 2006. The relationship between agonist potency and AMPA receptor kinetics. *Biophys J,* 91**,** 1336-46.
ZILLES, K. & AMUNTS, K. 2009. Receptor mapping: architecture of the human cerebral cortex. *Curr Opin Neurol,* 22**,** 331-9.